Peer Review File

Manuscript Title: Visualizing Interfacial Collective Reaction Behaviour of Li-S Batteries

Reviewer Comments & Author Rebuttals

Reviewer Reports on the Initial Version:

Referees' comments:

Referee #1 (Remarks to the Author):

This manuscript entitled “Visualizing Interfacial Collective Reaction Behaviour of Lithium-Sulfur Batteries” by Xu, Amine, and Liao et al. has filled out the huge knowledge gap in commercializing lithium-sulfur battery, a very promising battery that shows 2-3 times higher energy density and much lower cost than current lithium-ion batteries. The authors used real-time liquid-cell electrochemical TEM to investigate the interfacial reaction process of lithium-sulfur batteries, and have well addressed the long debate on the origin and evolution of polysulfides shuttle as well as the sluggish reaction kinetics, and further the effect of electrode surface structure in tailoring these processes. The discovery of gathering-induced collective charge transfer of polysulfides is really new over the classical single-molecular catalysis process in batteries, which has been well supported by the in-situ TEM results and computational modeling efforts. The results would provide new material design principle to truly advance Li-S batteries. In light of the significance of this work to both battery community and electron microscopy field, I would recommend the publication of this work in Nature after addressing the following issues:

Major comments:
1) The observation of Li2S nanocrystalline and microrods during discharge with and without active centers are very interesting. However, despite difference in particle size and morphology, it seems like both of nanocrystalline and microrods can be reversibly converted back to polysulfides during charge (Fig. 2 and Fig. 4). Please explain in detail.

2) By comparing the reactions of polysulfides at different interfaces, two reaction mechanisms, stepwise transformation and instaneous transformation, were discovered. I think the difference in reaction pathway essentially comes from the variation of interfacial reaction kinetics. However, the authors are suggested to provide more coin-cell kinetic analysis to prove the ongoing process. For example, comparison of peak current variation during LiPSs reaction at different interfaces, and comparable measurement of activation energy during the conversion from Li2S6 to Li2S.

3) The morphologies of Li2S discharge products in real battery cell with and without active center should be provided, for example, ex situ SEM/TEM characterization of Li2S deposition on Mo NCs/N-G surface.

4) The electron beam induced effect is crucial in this experiment since Li-S involves both chemical and electrochemical processes. According to the results, it is believed electrochemical process dominated LiPSs reactions. Authors mentioned that the experiments were carried out under low

electron beam dose conditions (below 1.5 e– A–2 s–1). But discussions of the known electron beam induced effects are lacking. Will the observation lead to the decomposition of electrolyte? What is the electron beam intensity threshold for in situ TEM? Can the formation/dissolution of Li2S be driven by electron beam?

5) In MD simulations, as for the dense ion-complex, do the Li2S6 units put together in initial structure of MD or they aggregate during MD simulation? If the attraction is due to Mo nanocluster active sites, how would S62– and Li+ distribute or aggregate without Mo NCs/N-G or Ti surface? What would be if lowering the concentration of Li2S6 electrolyte?

Minor comments:
1) In Movie S1 and 2, besides the deposition of Li2S micro-rods, the dissolution/disappearance of small nanoparticles can also be observed. What is reason for this process? Would they affect the deposition of lager micro-rods?

2) Page 8, line 10: “It revealed that during initial gathering of polysulfides dense phase, the strong interaction between active centers and LiPSs stabilized the droplet-like dense phase (overlapped in red).” According to the collective reaction behavior described by the authors, the gathering and conversion of LiPSs in droplets should be happened simultaneously. This needs to be clarified in the relevant description and Fig. 4c.

3) Caption of Fig. 4d: “DFT calculated the quantify of charge quantity of Mo active centers (Q=+7.37 e)” The “quantify of charge quantity” should be clarified.

4) Caption of Fig. 4e: “Z-axis distance between Mo active centers and dense ion-complex phase was decreased from 42 to 82 ns.” How do the authors define Z-axis distance? Is it the distance from the droplet to surface?

5) The determining of the simulation cell in MD simulation should be provided. Why the simulation cell was not full filled with electrolytes, should it be set up according to experiments conditions?

6) In extended data Fig. 8c, the authors mentioned: “diffusion coefficients of Mo NCs/N-G (D1) and Ti (D2)” in figure caption. According to the experimental results, I think the calculated diffusion coefficient should be corresponded to LiPSs molecules at different interfaces? How do authors calculate the diffusion coefficients?

7) In extended data Fig. 8e, the authors calculated the charge density of Li2S6 in droplet-like dense phase at different times. They mentioned: “The fluctuations in the curves should be attributed the charge re-distribution and continuous approach towards interface of Mo NCs/N-G.” Why would Li2S6 reveal charge density variation? For which ions does it calculate the charge density? In fact, this data is not intuitive, can the authors add a schematic illustration to explain it?

8) The color code should be given in Fig. 2d.

Referee #2 (Remarks to the Author):

This work, entitled “Visualizing Interfacial Collective Reaction Behaviour of Lithium-Sulfur Batteries,” presented high-resolution and real-time observation of the structural evolution of lithium polysulfides (LiPSs) during lithiation, which was excessively hard to visualize using a conventional TEM at the atomic level due to its susceptibility to severe electron beam damage. Based on their highly resolved TEM images, the authors proposed that gathering of soluble LiPSs around active centers (in this case, Mo-N-C) induced the instantaneous deposition of nonequilibrium nanocrystalline/amorphous Li2S, thereby suppressing undesirable degradation of Li-S batteries, such as the shuttle effect of soluble LiPSs. The reviewer considers the high-resolution TEM results of LiPSs to be significant achievements, but the authors did not adequately explain instrumental advancements in this work as compared to the conventional imaging method. Even though cryo-EM techniques are employed, imaging sulfur with atomic resolution remains technically challenging as mentioned this reference paper [Ener. Environ. Sci., 15, 1423-1460 (2022)]. I agree with the viewpoints expressed in this reference paper, such as “More such studies are expected and should prove very insightful in the context of understanding mechanisms at play in LSBs. In situ cryo-EM is not yet a reality, nonetheless ex situ cryo-EM is proving very powerful when sample preparation is performed carefully. Further visualization of the chemical and structure information at the nanoscale should be performed. Should in situ TEM of LSBs with liquid electrolytes never be a reality, cryo-EM may well fill the gap in knowledge.” In this work, the authors employed a custom-made EC-TEM holder, which seems to be a typical biasing holder. Without a proper treatment, high-resolution imaging of sulfur, especially in-situ, is exceedingly difficult to visualize. Although very interesting, this manuscript has some severe shortcomings that would preclude it from publication in Nature in its present form. These shortcomings are noted below:

1. According to a very famous review paper [Niels de Jonge and Frances M. Ross, “Electron microscopy of specimens in liquid,” Nature Nanotechnology, 6, 695-704, (2011)], this review paper was concerned that (1) the liquid layers were still not particularly thin, and the spatial resolution achieved was often not much better than what was available, with much less effort, through light microscopy and (2) electrodeposited nanoparticles (or rods) tended to be nucleated at the top or bottom of SiNx windows, implying that heterogeneous nucleation occurred despite researchers’ willingness to observe ideal phenomena. In particular, the surface functionality of SiNx windows, such as hydrophobic or hydrophilic conditions, can influence the nucleation behaviour of LiPSs, as mentioned by the reference paper [Guangyuan Zheng, Yi Cui et al., “Amphiphilic Surface Modification of Hollow Carbon Nanofibers for Improved Cycle Life of Lithium Sulfur Batteries,” Nano Letters, 13, 1265-1270, (2013)]. In this regard, the authors should be aware that in situ observation using a liquid cell may not provide an accurate depiction of behaviour, so they should investigate various characterizations using in situ and ex situ analyses.

2. In abstract, the authors mentioned the limitations of in situ characterization tools for tracing the reaction of unstable LiPSs with high temporal and spatial resolution. Rehman et al. (Ener. Environ. Sci., 15, 1423-1460 (2022), cited in Ref. 8) also noted that sulfur is too sensitive to the high-energy electron beams, making imaging sulfur with TEM extremely difficult. Furthermore, even cryo-EM has not revealed the atomic details and structural change of LiPSs intermediates. The authors asserted that their in-situ electrochemical TEM (EC-TEM) using an electric field instead of conventional

electron beam-driven charging/discharging is superior and operates differently. However, we do not believe this mitigates the intrinsic susceptibility of sulfur (and LiPSs intermediates) to beam damage during imaging. In addition, it is well-known that Si3N4-based liquid TEM cells impede high-resolution imaging due to their relatively thick and high atomic number element windows with poor electron transmission. The authors should provide a reasonable explanation for the acquisition of such high-resolution TEM images of LiPSs and Li2S, even in liquid TEM cells.

3. On page 4, the authors presented two different types of nucleation-growth pathways: a single-step deposition of rod-like Li2S and a two-step deposition via Li2S2. In the main text, however, the authors overlooked a single-step deposition and described a two-step deposition via Ostwald ripening in detail, which has not yet been reported. Then, can the authors statistically explain whether a two-step deposition is the dominant mechanism without active centers over a single-step one? In the same context, why is 'the depletion area' (contrast variation dur to the consumption of soluble LiPSs) invisible during a single-step deposition in extended data Fig. 2?
In addition, the authors mentioned that "if the localized concentration of LiPSs species was sufficient, Li2S could also be directly deposited through a single-step," showing simultaneous occurrences of a single-step and two-step deposition reaction in identical liquid TEM cells, which can be attributed to heterogeneous concentration in electrolytes. Then do the authors believe that single-step reactions preferentially occur in highly concentrated electrolytes?
- On page 4, typo (marked as particle #1 and #2 in Fig. 1b): Fig. 1b → Fig. 2b.
- On page 4, typo: Fig. 2a ↔ Fig. 2b
- Authors should provide corresponding positions in TEM images to SAED patterns of granular Li2S2 and rod-like Li2S in Fig. 2c and 2e.

4. In extended data Fig. 5, the authors analyzed the oxidation states of Mo using XANES and XPS. They claimed the existence of Mo4+ and Mo6+ using XPS peak deconvolution, but they did not provide any related references. In addition, it is well-known that XANES is a much more precise tool than XPS to detect the oxidation state of transition metals. Therefore, the estimation of oxidation states of Mo should be based on XANES analysis.

5. As mentioned above, the authors should provide corresponding sample imaging positions at a low magnification for HR-TEM images in Fig. 3i.

6. Obtaining images with atomic resolution for Fig. 3i is extremely challenging. The experimentally acquired images appear to have undergone noise cancellation. Please include raw data for Fig. 3i in the supplementary information or extended Figures. In addition, the authors should elaborate on the experimental conditions in this section. The reviewer is concerned that disagreements will arise if this manuscript is later published. Therefore, the authors should illuminate how to acquire high-resolution images under unfavorable conditions of strong electron beams, thick electrolytes relative to LiPSs, and relatively high atomic numbers relative to LiPSs.

7. On page 7, I believe that the term 'non-equilibrium' Li2S means polycrystalline (or amorphous) products in Mo-NCs/N-G, in contrast to single-crystal Li2S in a bare electrode. Additionally, the authors mentioned that multiple droplets (shown in Supplementary Movie. S6) should not be assigned to crystallized or nucleated Li2S2/Li2S. I do not support the idea that the multiple droplets

are highly concentrated Li2Sn (2<n<6) from TEM images. The authors should provide a reasonable explanation as to why they recognized that this behaviour is distinct from conventional step-by-step reaction.

8. How is it verified in DFT calculations that the strong interaction between Mo active centers and LiPSs droplets successfully suppresses the step-by-step evolution of soluble LiPSs and causes the instantaneous crystallization of Li2S?

9. In extended data Fig. 3, the authors simulated the crystal structure of tetragonal Li2S2 and hexagonal Li2S2 based on other materials such as Li2O2 and so on. However, they simulated hexagonal materials instead of Li2S2. This evidence is insufficient to establish that the structure of Li2S2 is tetragonal. Thus, the author should explain why they simulated hexagonal materials instead of hexagonal Li2S2.

Referee #3 (Remarks to the Author):

In this work, the authors visualized the transformation of LiPSs over electrode interfaces at atomic scale by using in situ liquid-cell electrochemical transmission electron microscopy. They found the gathering-induced collective charge transfer of LiPSs on nanocluster active center immobilized surface and the induced instaneous deposition of nonequilibrium Li2S nanocrystals from LiPSs dense liquid phase. It is a challenge work and found an interesting results. Therefore, I recommended it to be published after the following issues being addressed.
1. Based on the authors' mentioned mechanism, the gathering of the LiPSs into droplet-like dense phase is important for the one step deposition. How to confirm the formation of the dense phase? Moreover, whether electric field or adsorption is the driving force for the gathering of LiPSs? Does the long chain LiPSs were not oxidized to short chain LiPSs during the gathering process under the electric field? More evidences are needed to address these issues.
2. As we known, the LiPSs, Li2S2 and Li2S are sensitive to the e-beam irradiation. What about the effect of e-beam on the HRTEM image and the electrochemical reaction during the in situ experiments.
3. In Extended Data Fig. 2 (17 s) and Movie S2, discharge products were observed far from the electrode surface. It is a interesting phenomenon. The reasons and the electrochemical mechanisms are suggested to be further discussion.
4. In situ or ex situ Raman spectra or XRD measurements are suggested to be performed to further confirm the gathering-induced collective charge transfer of LiPSs during the discharge/charge process of the batteries.

Author Rebuttals to Initial Comments:

Nature (Manuscript ID: 2022-10-16085)

Visualizing Interfacial Collective Reaction Behaviour of Lithium-Sulfur Batteries

Authors: Shiyuan Zhou,† Jie Shi,† Sangui Liu, Gen Li, Fei Pei, Youhu Chen, Junxian Deng, Qizheng Zheng, Jiayi Li, Chen Zhao, Inhui Hwang, Cheng-Jun Sun, Yuzi Liu, Yu Deng, Ling Huang, Yu Qiao, Gui-Liang Xu,* Jian-Feng Chen, Khalil Amine,* Shi-Gang Sun and Hong-Gang Liao*

We would like to express our sincere gratitude to the editor and all the three referees for the valuable feedback/suggestions on our work. The insightful comments prompted us to engage in deeper reflection and make further improvements to the manuscript.

In this section, we provide a detailed point-by-point response to each comment made by the referees. To distinguish their comments from our responses, we have presented their comments in *italics*. Additionally, any revisions we have made to our manuscript or supporting information are highlighted in red for clarity.

Besides, to facilitate the distinction of figures in different files, we have marked them as follows: **Figs. R1-60** are the figures in response; **Figs. 1-4** are the figures in main text; **Extended Data Figs. 1-10** are the figures in extended data; **Figs. S1-32** are the figures in supporting information.

Thank you once again to the editor and referees for their valuable comments.

Responses to Referees:

A Detailed Point-by-Point Responses to Referees' Comments

Referee #1:

General Comment: *This manuscript entitled "Visualizing Interfacial Collective Reaction Behaviour of Lithium-Sulfur Batteries" by Xu, Amine, and Liao et al. has filled out the huge knowledge gap in commercializing lithium-sulfur battery, a very promising battery that shows 2-3 times higher energy density and much lower cost than current lithium-ion batteries. The authors used real-time liquid-cell electrochemical TEM to investigate the interfacial reaction process of lithium-sulfur batteries, and have well addressed the long debate on the origin and evolution of polysulfides shuttle as well as the sluggish reaction kinetics, and further the effect of electrode surface structure in tailoring these processes. The discovery of gathering-induced collective charge transfer of polysulfides is really new over the classical single-molecular catalysis process in batteries, which has been well supported by the in-situ TEM results and computational modeling efforts. The results would provide new material design principle to truly advance Li-S batteries. In light of the significance of this work to both battery community and electron microscopy field, I would recommend the publication of this work in Nature after addressing the following issues.*

Response to General Comment: We would like to thank you for appreciating our work. We have carefully considered each comment and provided a detailed point-by-point response as follows:

Major Comments:

Major Comment 1: *The observation of Li_2S nanocrystalline and microrods during discharge with and without active centers are very interesting. However, despite difference in particle size and morphology, it seems like both nanocrystalline and microrods can be reversibly converted back to polysulfides during charge (Fig. 2 and Fig. 4). Please explain in detail.*

Response to Major Comment 1: Thank you for your comment. Despite the fact that both Li_2S nanocrystalline and some micro-rods can be transformed back into LiPSs during charging, there are still notable differences in their reaction kinetics and reversibility. Liquid cell EC-TEM results showed that during potentiostatic charging,

the decomposition rate of Li_2S micro-rods on bare Ti electrodes exhibited a clear inflection near 240 s (Fig. 2a, b), which can be attributed to the high energy barrier and inherent insulating properties of the Li_2S micro-rods. Accordingly, the oxidized LiPSs easily diffused into the bulk electrolyte, resulting in the loss of active species and hindering re-deposition at the electrode surface in the subsequent cycles. By contrast, the Mo NCs/N-G nanosheets effectively confined the dissolved LiPSs and enabled a reversible deposition (Fig. 4a, b).

The reaction kinetics of Li_2S dissolution were further analyzed in coin-type cells. Li_2S deposited on Mo NCs/N-G nanosheets exhibited a much lower charge transfer resistance, leading to the faster reaction kinetics during potentiostatic dissolution (Extended Data Fig. 9b, c). Hence, the results from *in situ* EC-TEM and coin-type cells confirmed the high reaction activity and reversibility of Li_2S nanocrystalline on Mo NCs/N-G nanosheets, while Li_2S micro-rods on Ti electrodes showed sluggish kinetics and severe LiPSs shuttle effects.

Major Comment 2: *By comparing the reactions of polysulfides at different interfaces, two reaction mechanisms, stepwise transformation and instaneous transformation, were discovered. I think the difference in reaction pathway essentially comes from the variation of interfacial reaction kinetics. However, the authors are suggested to provide more coin-cell kinetic analysis to prove the ongoing process. For example, comparison of peak current variation during LiPSs reaction at different interfaces, and comparable measurement of activation energy during the conversion from Li_2S_6 to Li_2S.*

Response to Major Comment 2: Thank you for your suggestion about the kinetic analysis. To investigate the impact of active centers on the redox reactions of Li-S batteries, we conducted CV tests in symmetric cells using Ti meshes as working/counter electrodes with/without the decoration of Mo NCs/N-G nanosheets, 100 mM Li_2S_6 as electrolyte, and a scanning rate of 0.1 mV s^{-1}. We further quantitively described the different reaction kinetics by calculating the activation energy (E_a) during the liquid-solid conversion of LiPSs, using a similar configuration of coin-type cell. These electrochemical results were separately discussed as follows:

CV tests of symmetric cells: In symmetric cells, CV curves of Mo NCs/N-G nanosheets exhibited two pairs of reversible redox peaks, labeled as peaks *a*, *b*, *c*, and *d* (Fig. R1a). Typically, peak *a* denotes the reduction of Li_2S_6 to Li_2S, while peak *d* represents the decomposition of S_8 to Li_2S_6. Peaks *b* and *c* correspond to the reversible processes of peaks *a* and *d*, respectively. Mo NCs/N-G nanosheets exhibited a much higher current density, almost ten times that of the bare Ti electrode. This should be attributed to an accelerated conversion of LiPSs on Mo NCs/N-G nanosheets. Moreover, the potential gap between peaks *a* and *b* of Mo NCs/N-G (ΔE_1) nanosheets was found to be 0.67 V, which was much lower than that of the bare Ti electrode at 0.82 V (ΔE_2). This suggested a lower energy barrier and polarization of the reversible reactions between Li_2S_6 and Li_2S[1]. Mo NCs/N-G nanosheets showed only a marginal potential shift of the redox peak with an increase in the scanning rate (Fig. R1b), indicating their superior reaction kinetics and ion diffusion properties.

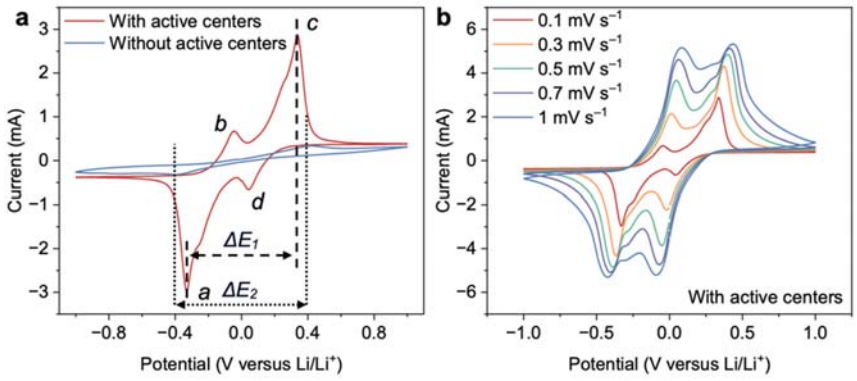

Fig. R1 | CV profiles of symmetric cells. (a) Comparison of CV profiles with/without mediation of active centers at a scan rate of 0.1 mV s^{-1}. (b) CV profiles with mediation of active centers at different scan rates of 0.1, 0.3, 0.5, 0.7, and 1 mV s^{-1}.

Calculation of activation energy: E_a was calculated according to the Arrhenius equation, by measuring the charge transfer resistance (R_{ct}) from Electrochemical impedance spectroscopy (EIS) tests at specific discharge potentials. To stabilize the potential for a particular conversion step, the cell was discharged to the desired potential and held at the same potential (chronoamperometry) until the output current remained constant. EIS tests were then performed at specific discharge voltages of 2.0, 1.9, 1.8, and 1.7 V, which usually represents the liquid-to-solid conversion of LiPSs,[2] at frequencies

ranging from 10 mHz to 100 kHz (Fig. R2). The intercept of the first semicircle with the horizontal axis corresponds to the resistance of electrode and electrolyte (R_e). The first semicircle forms due to the surface deposition of solid Li_2S_2/Li_2S (R_s). The second semicircle is induced by the charge transfer process occurring at the surface of active centers (R_{ct}). The straight line represents the resistance of Li^+ diffusion inside Mo NCs/N-G nanosheet (Z_w). By fitting the measured R_{ct} at different temperatures to the Arrhenius equation, we calculated E_a at each measured potential (Fig. R3a). With mediation of active centers, E_a was significantly lower, the E_a values with/without active centers were 0.27/0.5, 0.23/0.5, 0.17/0.49, and 0.19/0.49 eV, corresponding to discharge potentials of 2.0, 1.9, 1.8, and 1.7 V, respectively (Fig. R3b). The results of symmetric CV tests and the calculation of E_a confirm that the collective reaction pathway at the active center-mediated interface significantly reduces the energy barrier and accelerates the conversion of soluble LiPSs intermediates into insoluble Li_2S_2/Li_2S. This indicates that the active center-mediated interface plays a crucial role in facilitating the conversion process.

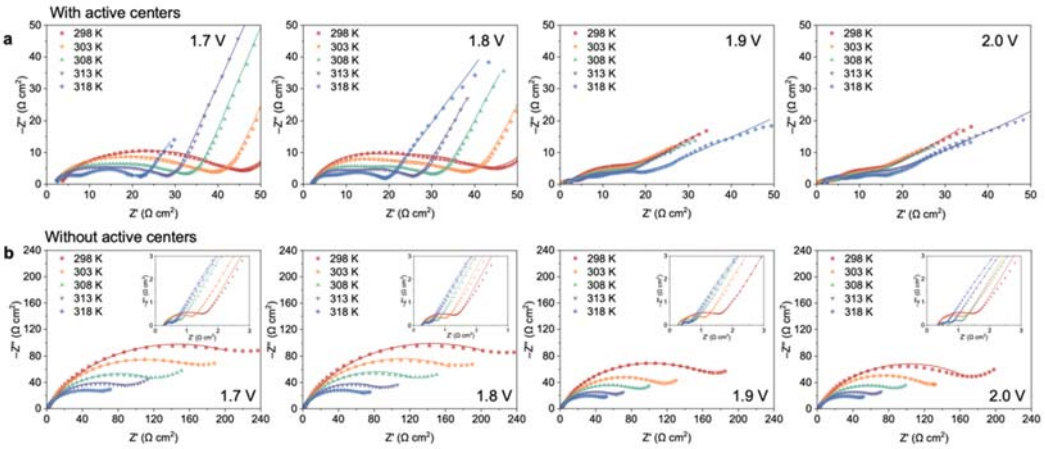

Fig. R2 | Fitting of Nyquist profiles at different temperatures and discharge potentials. (a, b) Nyquist profiles of EIS including the measured (symbols) and fitting (lines) impedance data with/without active centers after galvanostatic discharge at 1.7, 1.8, 1.9, and 2.0 V. The insets are the local magnification profiles.

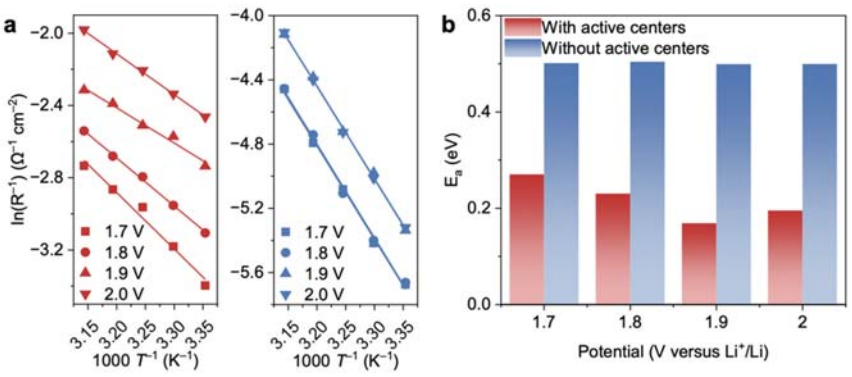

Fig. R3 | Calculation of activation energy based on Arrhenius equation. (a) Arrhenius plots of the linear relationship between logarithmic values of the reciprocal of R_{ct} and the reciprocal of absolute temperatures for 1.7, 1.8, 1.9, and 2.0 V, with (red)/without (blue) active centers. (b) Comparison of the corresponding activation energy (E_a) calculated based on the slope of linear fitting in Fig. R3a.

Revision to Major Comment 2: The corresponding contents have been added in Extended Data Fig. 9d-f and Fig. S31, 32. The discussions have been added in manuscript (page 11, line 3-11).

Major Comment 3: *The morphologies of Li_2S discharge products in real battery cell with and without active center should be provided, for example, ex situ SEM/TEM characterization of Li_2S deposition on Mo NCs/N-G surface.*

Response to Major Comment 3: Thank you for your suggestion regarding conducting *ex situ* experiments to validate our *in situ* results. Our *in situ* EC-TEM experiments revealed that active centers led to the formation of Li_2S nanocrystalline on the surface of Mo NCs/N-G nanosheet, whereas a bare electrode surface resulted in the deposition of Li_2S in a rod-like structure.

Following the deposition of Li_2S in coin-type cells, the XRD patterns of Ti mesh with and without the decoration of Mo NCs/N-G nanosheet were analyzed. In Fig. R4a, both patterns displayed characteristic diffraction peaks at approximately 26.4°, corresponding to the (111) crystal plane of cubic Li_2S (PDF#26-1188). Notably, the Li_2S-Mo NCs/N-G pattern exhibited a stronger diffraction peak, indicating higher

conversion activity from soluble Li_2S_6 to solid Li_2S. The size of the deposited Li_2S crystals was assessed using the Scherrer equation, $D = K\lambda/(\beta\cos\theta)$, where K is the Scherrer constant; λ is the X-ray wavelength; β is the full width at half maximum (FWHM); θ is the Bragg angle. As the crystalline size was inversely related to the β value, the Li_2S-Mo NCs/N-G nanosheet exhibited a smaller crystalline size compared to Li_2S-Ti.

The morphologies of Ti mesh, both with and without the decoration of Mo NCs/N-G nanosheet, were analyzed after Li_2S deposition. *Ex situ* SEM images indicated that the presence of Mo NCs/N-G resulted in a thicker and rougher surface after Li_2S deposition, primarily in a particle-like structure (Fig. R4b, c). By contrast, the bare Ti electrode exhibited a passivated layer covering the electrode surface, with sparse deposition of rod-like/plate-like Li_2S (Fig. R4d). The difference in surface morphology was further confirmed by *ex situ* (S)TEM images and EDS mappings. In the case of Mo NCs/N-G nanosheet, Li_2S was deposited in the form of nanocrystalline, primarily exposing the (111), (200), and (220) crystal planes (Fig. R5a-c). Conversely, Li_2S deposited on the bare Ti electrode surface showed a rod-like structure (Fig. R5d-f). Given that the same electrolyte was used in coin-type cells, the different deposition morphology and structure of Li_2S discharge product was attributed to the decorated Mo NCs/N-G with high activity, which was consistent with the results obtained from *in situ* EC-TEM experiments.

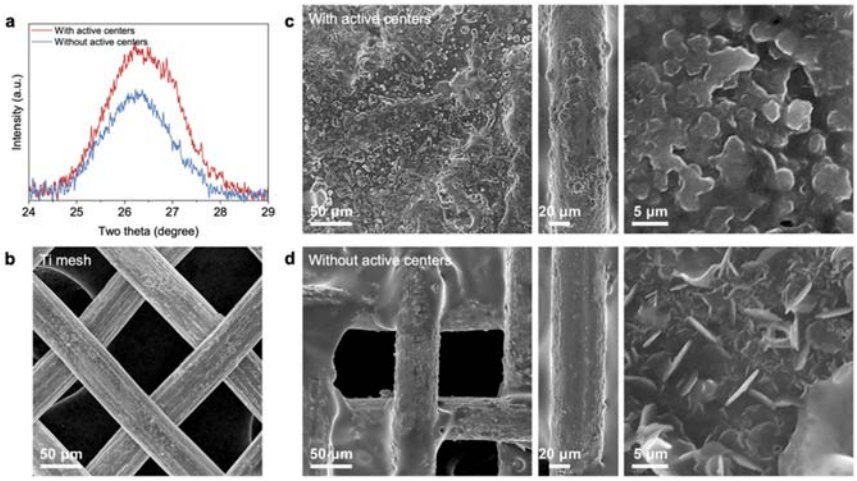

Fig. R4 | *Ex situ* XRD and SEM characterizations. (a) *Ex situ* XRD characterization

of Li_2S deposited electrode with/without mediation of active centers. Li_2S electrodeposition was conducted by galvanostatic discharge at 16 μA cm^{-2} with 100 mM Li_2S_6 electrolyte in coin-type cells from OCP to 1.7 V. To avoid air exposure, the deposited cells were dis-assembled in argon-filled glovebox and re-assembled into Kapton-filmed coin-type cells. (b) SEM image of bare Ti mesh. (c, d) SEM images of Li_2S deposited Ti mesh with/without mediation of active centers.

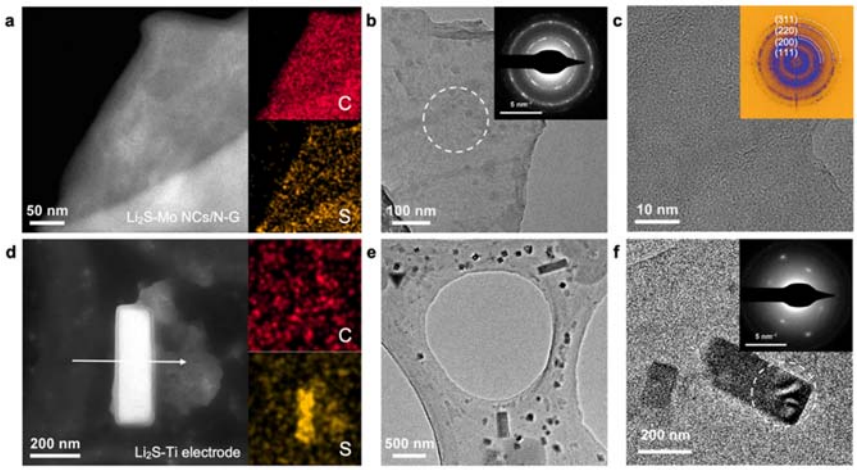

Fig. R5 | *Ex situ* (S)TEM characterization of deposited Li_2S with/without active centers. (a) *Ex situ* STEM and EDS mappings of Mo NCs/N-G nanosheet after Li_2S deposition in coin-type cells. (b, c) (HR)TEM images and the corresponding SAED and FFT patterns of Li_2S nanocrystalline deposited on Mo NCs/N-G nanosheet. Li_2S deposition was conducted by galvanostatic discharge at 16 μA cm^{-2} with 100 mM Li_2S_6 electrolyte in coin-type cells from OCP to 1.7 V. (d) *Ex situ* STEM images and EDS mappings of Li_2S micro-rod deposited on bare Ti electrode. (e, f) TEM images and the corresponding SAED pattern of Li_2S micro-rods. Li_2S deposition was conducted by the same galvanostatic discharge.

Revision to Major Comment 3: The corresponding contents have been added in Fig. S29, 30. The discussions have been added in Supplementary Discussion 6 (consistency of *in situ* and *ex situ* experiments).

Major Comment 4: *The e-beam induced effect is crucial in this experiment since Li-S involves both chemical and electrochemical processes. According to the results, it is believed electrochemical process dominated LiPSs reactions. Authors mentioned that the experiments were carried out under low e-beam dose conditions (below 1.5 $e^- A^{-2} s^{-1}$). But discussions of the known e-beam induced effects are lacking. Will the*

observation lead to the decomposition of electrolyte? What is the e-beam intensity threshold for in situ TEM? Can the formation/dissolution of Li_2S be driven by e-beam?

Response to Major Comment 4: Thank you for your valuable suggestions regarding the e-beam effect in the liquid cell. To address your concerns, we conducted long-term observations using different e-beam dose rates, and studied their influence on the electrolyte, Li_2S nucleation/deposition, and electrochemical process.

We began with conducting observations at a dose rate of 11.5 e $Å^{-2}$ s^{-1}. Time-series TEM images revealed that the high dose rate caused the decomposition of solid discharge products and LiPSs electrolyte after 34.4 s, with the generation of nanobubbles simultaneously (Fig. R6a). By contrast, when we reduced the dose rate to 1.54 and 1.13 e $Å^{-2}$ s^{-1}, the side reactions were effectively prevented over the same observation time, stabilizing both the solid discharge products and LiPSs electrolyte, while the spatial resolution was maintained for real-time observation (Fig. R6b, c). Therefore, it is essential to note that a high e-beam dose rate can lead to the decomposition and accumulated carbon contamination of the electrolyte, resulting in a degradation in image resolution. The threshold of e-beam intensity for high-resolution observation should depend on both the dose rate and observation time. The e-beam damage on the electrolyte or Li_2S crystals can be largely alleviated by conducting *in situ* electrochemical reactions with dose rates below 1.5 e $Å^{-2}$ s^{-1}.

The above investigation has confirmed that a high e-beam dose rate could lead to the decomposition/dissolution of solid Li_2S. To further investigate the influence of the e-beam on the formation of Li_2S, we applied individual e-beam without applying an electric field. Time-series TEM images revealed that the e-beam alone was not able to induce heterogeneous deposition of Li_2S on SiN_x or Ti electrodes over 164 s (Fig. R6d). We also quantified the effect of the e-beam during potentiostatic discharge at –0.5 V under a dose rate of 1.2 e $Å^{-2}$ s^{-1}, which accounted for 2.46% of the measured current density (Fig. R6e, f). The above investigation illustrated that electron accessibility is the prerequisite for electrochemical conversion from soluble Li_2S_6 to solid Li_2S, which can only be driven by an external electric field, not an e-beam.

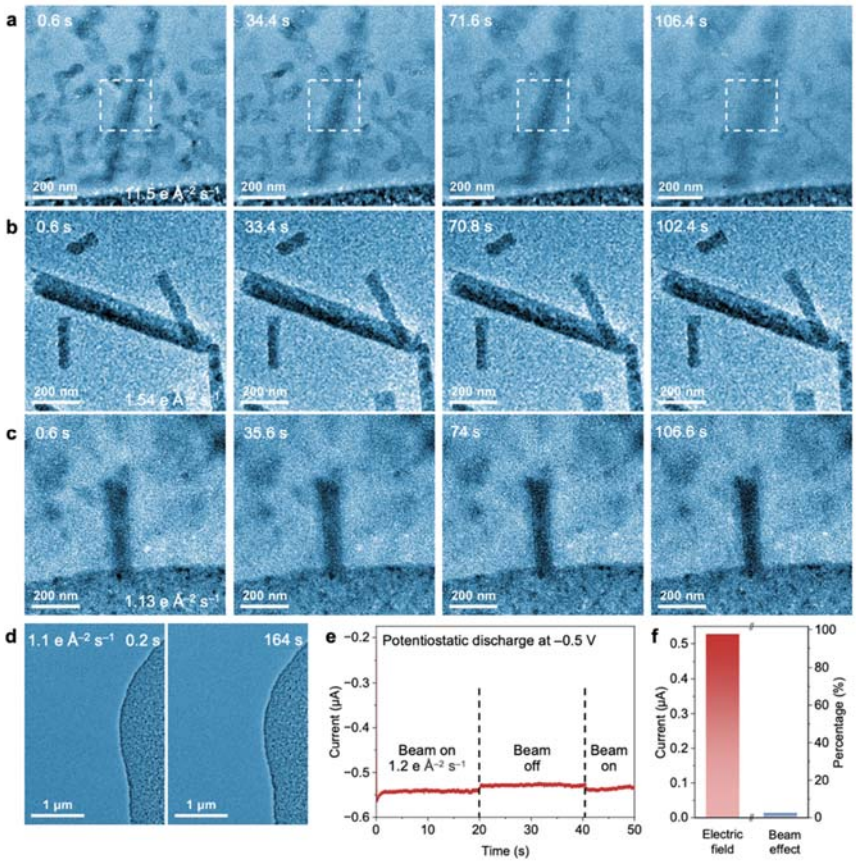

Fig. R6 | E-beam effect in electrochemical liquid cells. (a-c) Time-series TEM images of Li_2S at the dose rates of 11.5, 1.54, and 1.13 e $Å^{-2}$ s^{-1}, respectively. (d) Exclusion of e-beam effect on heterogenous deposition of Li_2S. (e, f) Measured current during potentiostatic discharge at –0.5 V with e-beam on (1.2 e $Å^{-2}$ s^{-1})/off.

<u>Revision to Major Comment 4:</u> The corresponding contents have been added in Fig. S3, 8. The discussions have been added in Supplementary Discussion 2 (e-beam effects).

Major Comment 5: *In MD simulations, as for the dense ion-complex, do the Li_2S_6 units put together in initial structure of MD or they aggregate during MD simulation? If the attraction is due to Mo nanocluster active sites, how would S_6^{2-} and Li^+ distribute or aggregate without Mo NCs/N-G or Ti surface? What would be if lowering the concentration of Li_2S_6 electrolyte?*

<u>Response to Major Comment 5:</u> We appreciate your comments on our MD simulations and would like to address your concerns by splitting and summarizing them

into two main areas: (1) the initial structure of Li_2S_6 and (2) the distribution of S_6^{2-} and Li^+ ions with different concentrations in bulk electrolyte.

In the previous MD simulations, Li_2S_6 molecules and solvent molecules were added to the electrode surface in the form of aggregated liquid layers in the initial MD models, to study the interaction between Li_2S_6 droplets and the electrode surface. In response to the suggestion from the referee, we constructed the randomly dispersed S_6^{2-} and Li^+ ions at varying concentrations (2.51 wt%, 5.28 wt%, 9.68 wt%, and 17.93 wt%) without electrode surface and investigated their movement behavior inside bulk LiPSs electrolyte (Fig. R7). Time-series MD simulations revealed that these ions tended to aggregate spontaneously in solution, forming Li_2S_6 clusters with varying sizes. By calculating the average number of S atoms in these clusters (Fig. R8), we found a direct correlation between cluster size and the concentration of S_6^{2-} and Li^+ ions. Specifically, the cluster size increased as the ion concentration increased.

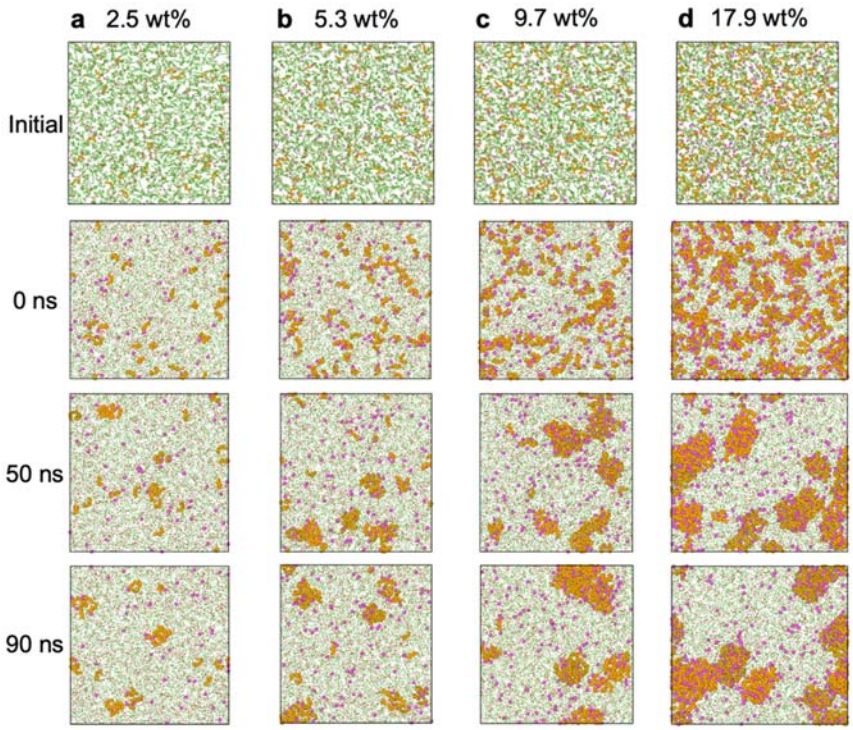

Fig. R7 | Time-series MD simulations of spontaneous aggregation of Li_2S_6 without electrode surfaces. Snapshots of MD simulations with different Li_2S_6 concentrations of (a) 2.5 wt%, (b) 5.3 wt%, (c) 9.7 wt%, and (d) 17.9 wt%, respectively. The first row was the initial structures of MD simulations, where S_6^{2-} and Li^+ ions were randomly

dispersed in the electrolyte. After 0.5 ns of 1 bar NPT simulation, the NVT simulation sampling was carried out. The simulation results revealed that the aggregation degree of Li_2S_6 molecular increased with an increase in concentration.

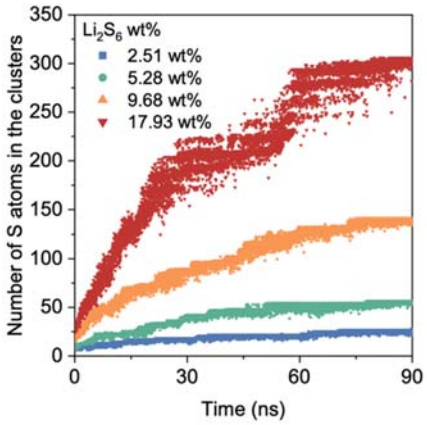

Fig. R8 | Statistical analysis of S atom variation. Statistics of S atoms in Li_2S_6 clusters with different electrolyte concentrations of 2.51 wt%, 5.28 wt%, 9.68 wt%, and 17.93 wt%. The five largest clusters were used to calculate the average number of contained S atoms.

Revision to Major Comment 5: The corresponding contents have been added in Extended Data Fig. 8a, b and Fig. S24, 25. The discussions have been added in Supplementary Discussion 5 (simulations of gathering and charge transfer in dense phase).

Minor Comments:

Minor Comment 1: *In Movie S1 and 2, besides the deposition of Li_2S micro-rods, the dissolution/disappearance of small nanoparticles can also be observed. What is the reason for this process? Would they affect the deposition of lager micro-rods?*

Response to Minor Comment 1: Thank you for your comment. We would like to response in the following two aspects:

Explanation for the formation and dissolution of small nanoparticles: The conversion from soluble Li_2S_6 to solid Li_2S_2/Li_2S occurred through the electrochemical reduction at the electrode interface ($n/6S_6^{2-} + (2-n/3)\ e^- \rightarrow S_n^{2-}$, $n \leq 2$). During this process, some

of the reduced S_2^{2-}/S^{2-} ions diffused away from the electrode and caused the precipitation of granular Li_2S_n in the electrolyte ($S_n^{2-} + Li^+ \rightarrow Li_2S_n\downarrow$, $n\leq2$), as revealed in the TEM image at 17 s (Fig. R9). However, these solid discharge products were thermodynamically unstable and were prone to undergo disproportionation reactions or chemically react with soluble/long-chain LiPSs intermediates,[3] thus leading to their spontaneous decomposition and dissolution. As a result, the formation and dissolution of solid discharge products in the electrolyte was observed during the potentiostatic discharge.

Impact of dissolved particles on the deposition of micro-rods: The decomposition of small nanoparticles occasionally occurred, as revealed in Fig. R9 and Fig. 2b. First, the impact on the deposition of larger micro-rods can be understood according to the statistics of projection area variation in Fig. 2a. It revealed that the decrease of metastable particle #2 (smaller size) was accompanied by the increase of particle #1 (larger size), and the projection area of particle # 1 underwent an accelerated process after 116.2 s. Time-series TEM images (Fig. 2b), especially at 116.2 s, and Supplementary Movie S1 showed the direct observation of mass transfer from particle #2 (smaller size) to particle #1 (larger size), through a process similar to Oswald ripening. This should be attributed to the large surface energy of small particles, which tended to dissolve and re-crystallize on the large particles to lower the system energy and stabilize crystal structures. To further confirm the inter-particle mass transfer, we supplemented a potentiostatic discharge at –0.5 V on the Ti electrode surface (Fig. R10), which revealed a similar mass-redistribution of particles #7/#8 and particles #9/#10.

Therefore, the above investigation indicates that reduced S_n^{2-} ($n\leq2$) ions are diffusible and can result in the precipitation of solid Li_2S_n ($n\leq2$) near the electrode surface. The thermodynamic instability and chemical reactivity of these solid discharge products can lead to their spontaneous dissolution or decomposition, thereby supplying LiPSs species for the growth of larger particles through Ostwald ripening.

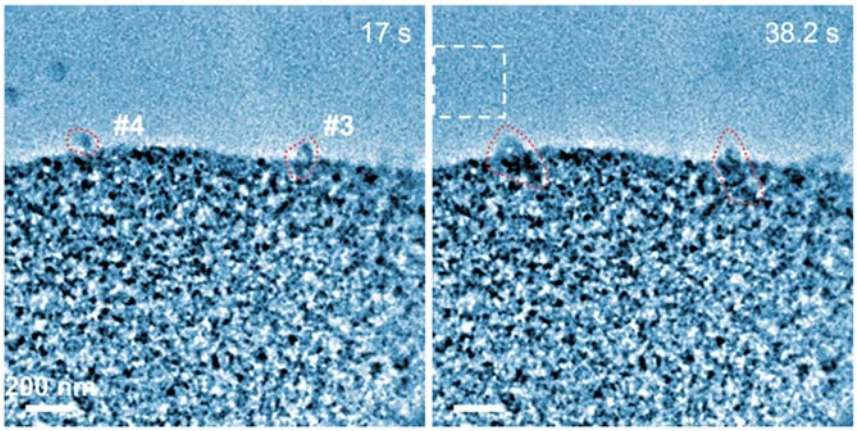

Fig. R9 | Li_2S deposition without mediation of active centers through a single-step pathway. Time-series TEM images from Supplementary Movie S2 of single-step deposition of Li_2S in an electrochemical liquid cell, showing the formation and dissolution of solid discharge products detached from electrode surface. The uncontacted distance of solid discharge products towards electrode surface was marked by the double-sided arrows.

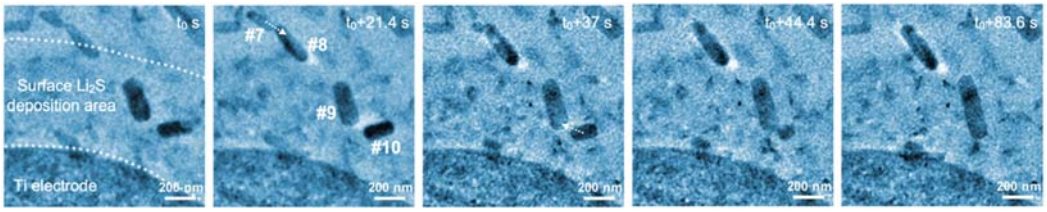

Fig. R10 | Surface Li_2S deposition on Ti electrode via two-step mechanism. Time-series TEM images showing two-step Li_2S deposition in liquid-cell EC-TEM. TEM image (t_0 s) revealed solid Li_2S deposited on the surface of Ti electrode. The mass transfer direction of inter-particle Ostwald ripening is indicated by the dotted single-sided arrows (t_0+21.4 s).

Revision to Minor Comment 1: The corresponding contents and discussions have been added in Fig. S9, 10.

Minor Comment 2: *Page 8, line 10: "It revealed that during initial gathering of polysulfides dense phase, the strong interaction between active centers and LiPSs stabilized the droplet-like dense phase (overlapped in red)." According to the collective reaction behavior described by the authors, the gathering and conversion of LiPSs in droplets should happen simultaneously. This needs to be clarified in the relevant description and Fig. 4c.*

Response to Minor Comment 2: Thank you for asking about the process of gathering and conversion of LiPSs droplets. *In situ* EC-TEM analysis revealed that during potentiostatic discharge on the surface of Mo NCs/N-G nanosheets, non-equilibrium Li_2S was directly converted from the droplet-like LiPSs dense phase without the formation of any intermediates. The conversion from soluble Li_2S_6 to solid Li_2S requires sustained electrochemical reduction ($Li_2S_6 + 10Li^+ + 10e^- = 6Li_2S$). Therefore, it was inferred that S_6^{2-} ions in the dense phase experienced a collective electrochemical reduction during the simultaneous gathering and conversion of LiPSs.

Previous MD simulations have demonstrated the gathering effect of Mo active centers through long-range interactions. *Ab initio* molecular dynamics (AIMD) simulations were further employed to study the charge transfer between Mo active centers and Li_2S_6. We simulated the charge distribution of the system, containing Li_2S_6 molecules in the dense phase before and after applying an electrode potential. The potential was provided by electron-donating Li atoms added below Mo NCs/N-G electrode. From the top view, we defined S_6 ions in the external, middle, and internal layers based on their distance from the Mo active centers (Fig. R11). When the electrode potential was applied, the number of electrons transferred in S_6^{2-} ions remained almost unchanged compared to its original state. However, after a relaxation period of 8 ps, S_6 ions received a significant increase in the number of electrons transferred from the electrodes. Specifically, compared with S_6 ions in the internal layer (3.78 – 3.34 = 0.44e), S_6 ions in the middle layer received even more electrons (2.42 – 1.73 = 0.69e), and S_6 ions in the external layer also gained some electrons (1.52 – 1.37 = 0.15e). AIMD results revealed that electrons were transferred and shared from Mo active centers to S_6 ions in the droplet-like dense phase, from internal to external layers, rather than only the LiPSs molecules near the active centers. In summary, both *in situ* EC-TEM experiments and simulations confirmed that Mo active centers have a long-range gathering effect, inducing the formation of droplet-like dense phase. Electrons can be transferred and shared in these gathered LiPSs molecules.

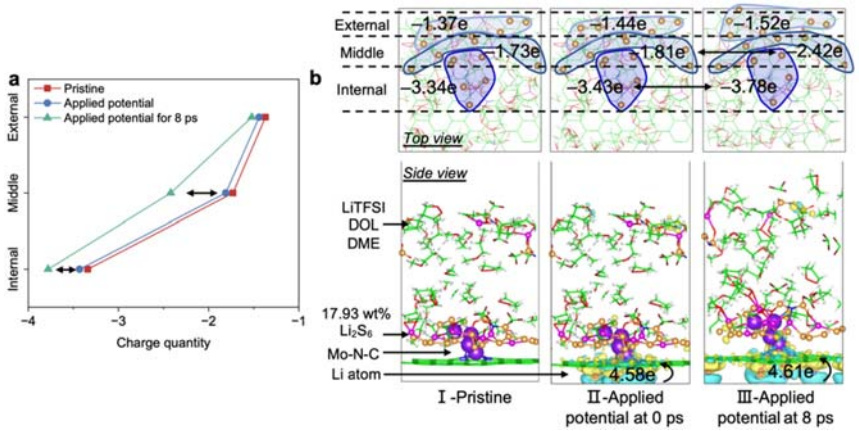

Fig. R11 | AIMD simulation of charge variation in S_6^{2-} ions. (a) Statistics of charge variation of S_6 ions in the internal, middle, and external layers. (b) AIMD simulation of charge variation of S_6 ions around Mo active centers from a top view and a side view. S_6 ions in the dense phase are divided into internal, middle, and external layers according to the distances from Mo active centers when viewed from the top. The charge distribution diagrams, shown from left to right, include (I) pristine structure relaxed for 20 ps before applying the electrode potential, simulations at (II) 0 ps and (III) 8 ps after applying the electrode potential. Considering the dynamic charge distribution, the ions in the dense phase were defined as S_6 ions.

Revision to Minor Comment 2: The corresponding contents have been added in Extended Data Fig. 8g and Fig. S27e. The discussions have been added in manuscript (page 10, line 13-22) and Supplementary Discussion 5 (simulations of gathering and charge transfer in dense phase).

Minor Comment 3: *Caption of Fig. 4d: "DFT calculated the quantify of charge quantity of Mo active centers (Q=+7.37 e)" The "quantify of charge quantity" should be clarified.*

Response to Minor Comment 3: The corresponding description has been revised into "DFT calculated the charge quantity of Mo active centers (Q=+7.37 e)".

Minor Comment 4: *Caption of Fig. 4e: "Z-axis distance between Mo active centers and dense ion-complex phase was decreased from 42 to 82 ns." How do the authors define Z-axis distance? Is it the distance from the droplet to surface?*

Response to Minor Comment 4: The Z-axis distance during the simulation from 42 to 82 ns has been defined from LiPSs droplet to the electrode surfaces (Ti electrode or Mo NCs/N-G).

Minor Comment 5: *The determining of the simulation cell in MD simulation should be provided. Why the simulation cell was not full filled with electrolytes, should it be set up according to experiments conditions?*

Response to Minor Comment 5: Thank you for your interest in the setup of our MD models. To ensure that the bottom of the electrode did not influence the solution layer, we set the unfilled area in the simulation cell, also known as a vacuum layer, with a thickness greater than 100 Å above the liquid layer. To account for the asymmetric structure of the Mo NCs/N-G model in the MD simulation, we used a surface solution layer model that was aperiodic in the Z-axis direction. As our MD simulation focused on the diffusion behavior of S_6^{2-} and Li^+ ions on the electrode interface, the thickness of the liquid layer in the MD model only needed to be thick enough to prevent the interaction between the gas-liquid surface layer and the electrode interface layer. After relaxation, the thickness of the entire solution layer exceeded 100 Å. Therefore, the vacuum layer would not influence the accurate description of the behavior of the solution, including the gas-liquid interface, bulk solution, and electrode interface layer.

Minor Comment 6: *In extended data Fig. 8c, the authors mentioned: "diffusion coefficients of Mo NCs/N-G (D_1) and Ti (D_2)" in figure caption. According to the experimental results, I think the calculated diffusion coefficient should correspond to LiPSs molecules at different interfaces? How do authors calculate the diffusion coefficients?*

Response to Minor Comment 6: We apologize for making misunderstanding in the caption of Extended Data Fig. 8. We would like to clarify that the calculated diffusion coefficients corresponded to those of Li_2S_6 molecules on the surfaces of Mo NCs/N-G

(D_1) and Ti electrode (D_2). They were calculated based on the diffusion of S atoms in Li_2S_6 molecules along Z-axis direction. We have corrected the error in the revised manuscript, and the caption of Extended Data Fig. 8f has been updated as follows: "MSD analysis of Li_2S_6 movement along the Z-axis direction. The diffusion coefficients of S atoms in Li_2S_6 molecules over Mo NCs/N-G (D_1) and Ti (D_2) surfaces were 2.73×10^{-7} cm^2 s^{-1} and 4.88×10^{-9} cm^2 s^{-1}, respectively."

Minor Comment 7: *In extended data Fig. 8e, the authors calculated the charge density of Li_2S_6 in droplet-like dense phase at different times. They mentioned: "The fluctuations in the curves should be attributed the charge re-distribution and continuous approach towards interface of Mo NCs/N-G." Why would Li_2S_6 reveal charge density variation? For which ions does it calculate the charge density? In fact, this data is not intuitive, can the authors add a schematic illustration to explain it?*

Response to Minor Comment 7: Thank you for your comment and suggestion. The charge density in the droplet-like dense phase was calculated by counting the contribution of S_6^{2-} ions in the liquid layer perpendicular to the electrode surface ($\rho_Q = \frac{2\times\sum_z^{z+0.5} n_{S6}}{X_{cell}\times Y_{cell}\times 0.5}$). As the droplet-like dense phase approached the electrode surface under the attraction of Mo NCs/N-G, S_6^{2-} ions in the liquid layer underwent simultaneous re-distribution, leading to the variation in charge density (Fig. R12). To aid in visualization, we have included a schematic illustration demonstrating the approach of the droplet-like dense phase to the Mo NCs/N-G surface and the continuous re-distribution of S_6^{2-} ions within it.

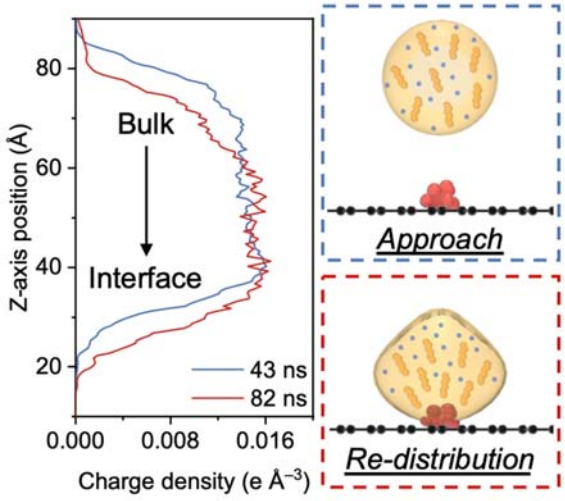

Fig. R12 | Charge density variation of S_6^{2-} ions in the liquid layer. Comparison of charge density variation curves between 43 and 82 ns of Li_2S_6 in droplet-like dense phase, corresponding to Fig. 4f, and the schematic illustration. The fluctuations in the curves and their movement along the Z-axis position should be attributed to the charge re-distribution and the continuous approach of droplet-like dense phase towards the Mo NCs/N-G interface, as illustrated schematically. The orange chains and blue balls in schematic illustration represent S_6^{2-} and Li^+ ions, respectively.

Revision to Minor Comment 7: The corresponding contents have been added in Fig. S27d.

Minor Comment 8: *The color code should be given in Fig. 2d.*

Response to Minor Comment 8: The corresponding description of crystal structure of Li_2S_2 unit cell has been added. The red and blue balls in Fig. 2d represent Li and S atoms, respectively.

Referee #2:

General Comment: *This work, entitled "Visualizing Interfacial Collective Reaction Behaviour of Lithium-Sulfur Batteries," presented high-resolution and real-time observation of the structural evolution of lithium polysulfides (LiPSs) during lithiation, which was excessively hard to visualize using a conventional TEM at the atomic level due to its susceptibility to severe e-beam damage. Based on their highly resolved TEM images, the authors proposed that gathering of soluble LiPSs around active centers (in this case, Mo-N-C) induced the instantaneous deposition of nonequilibrium nanocrystalline/amorphous Li_2S, thereby suppressing undesirable degradation of Li-S batteries, such as the shuttle effect of soluble LiPSs. The reviewer considers the high-resolution TEM results of LiPSs to be significant achievements, but the authors did not adequately explain instrumental advancements in this work as compared to the conventional imaging method. Even though cryo-EM techniques are employed, imaging sulfur with atomic resolution remains technically challenging as mentioned this reference paper [Ener. Environ. Sci., 15, 1423-1460 (2022)]. I agree with the viewpoints expressed in this reference paper, such as "More such studies are expected and should prove very insightful in the context of understanding mechanisms at play in LSBs. In situ cryo-EM is not yet a reality, nonetheless ex situ cryo-EM is proving very powerful when sample preparation is performed carefully. Further visualization of the chemical and structure information at the nanoscale should be performed. Should in situ TEM of LSBs with liquid electrolytes never be a reality, cryo-EM may well fill the gap in knowledge." In this work, the authors employed a custom-made EC-TEM holder, which seems to be a typical biasing holder. Without a proper treatment, high-resolution imaging of sulfur, especially in-situ, is exceedingly difficult to visualize. Although very interesting, this manuscript has some severe shortcomings that would preclude it from publication in Nature in its present form. These shortcomings are noted below.*

Response to General Comment: We sincerely appreciate your high evaluation of our results and the valuable feedback to help us clearly outline our strategies in the instrumental improvements. To better address your concerns, we have organized your comments into the following six key aspects, before discussing the detailed point-by-point responses to each question.

(1) *E-beam effect on Li_2S and in situ EC-TEM observation (Question 2 (Q2)).* The e-beam effect on pure Li_2S should be mainly attributed to the ionization, radiolysis, and heating, due to its poor electrical and thermal conductivity[4,5]. E-beam damage

has been observed in both commercial Li_2S and electrochemically deposited Li_2S via liquid cells or coin-type cells. By contrast, by ultrasonically mixing commercial Li_2S with graphene, the e-beam effect can be largely alleviated, allowing for atomic-resolution and long-time observation of Li_2S@graphene. This also explains how we can observe Li_2S nanocrystalline on Mo NCs/N-G nanosheet. Besides, a high e-beam dose rate can lead to the decomposition and carbon contamination of electrolyte, which can be prevented by reducing the e-beam dose rate to below 1.5 e $Å^{-2}$ s^{-1}.

(2) *The consistency of in situ and ex situ experiments (Q1).* We conducted a comparison of the structures of electrochemically deposited Li_2S through *in situ* EC-TEM observation and *ex situ* characterizations in coin-type cells, while taking into account the e-beam effect and liquid cell configuration on the electrochemical reactions. First, we supplemented the electrochemical deposition of Li_2S in coin-type cells. Subsequent *ex situ* TEM, SEM, and XRD revealed a high degree of structural consistency in liquid cells. Specifically, Li_2S was found to be nanocrystalline on Mo NCs/N-G surface and micro-rods on Ti surface. Second, we quantitively analyzed e-beam effect on electrochemical reactions during *in situ* experiment, under the dose rate of 1.2 e $Å^{-2}$ s^{-1}, which only accounted for 2.46% of the measured current density. It is worth noting that the e-beam cannot drive the deposition of Li_2S without the presence of electric field. Third, we constructed a half-covered SiN_x layer similar to that of liquid cells on a Ti current collector. We found that the insulating SiN_x layer blocked the electrochemical deposition of Li_2S on its surface, as the electrochemical reduction of S_n^{2-} ($2<n\leq6$) to S^{2-} requires charge transfer on conductive interfaces.

(3) *Advancements for high-resolution observation (Q2, Q6).* To achieve the high-resolution observation of LiPSs reactions and atomic structures of Li_2S, we comprehensively considered the liquid cell configuration, thickness of liquid layer, image acquiring conditions, and image processing method. First, the thicknesses of the spacer and SiN_x window primarily determine the spatial resolution in liquid cells. A ~100 nm spacer was used to assemble the bottom and top chips. *Ex situ* HRTEM

images of Li_2S@graphene revealed that with increasing thickness of SiN_x windows (11.2, 48 and 94.8 nm), the background noise gradually increased. By using ~10 nm SiN_x windows similar to *in situ* experiments, we are able to obtain stable atomic-scale HRTEM images of Li_2S. Second, the resolution of HRTEM image in liquid cells also depends on the thickness of the electrolyte layer. After the complete deposition of Li_2S on Mo NCs/N-G nanosheets, we used an "e-beam bubble generation" method to locally squeeze out the liquid layer, which had been previously adopted in our works[6-8]. If the liquid layer was completely excluded, the final imaging resolution should depend only on the thickness of top/bottom SiN_x observation windows, allowing us to obtain atomic-scale HRTEM images of Li_2S nanocrystalline on Mo NCs/N-G surface. Besides, HRTEM images were captured with a 4K resolution and an exposure time of 500 ms. For post-image processing, we applied the radial Weiner filter to HRTEM images to enhance the periodic crystal structure and reduce the background noise of carbon contamination and SiN_x windows.

(4) *Discussion of nucleation-growth pathways without active centers (Q3).* To distinguish between the nucleation-growth pathways of Li_2S on a Ti electrode surface, we conducted potentiostatic discharge reactions at two different potentials: –0.5 V and –0.1 V, and counted the quantities of granular and rod-like structures at various times. At a discharge potential of –0.5 V, both granular and rod-like solid discharge products formed, indicating that the reactions underwent both single-step and two-step pathways simultaneously. However, when we adjusted the discharge potential to –0.1 V, solid discharge products were primarily deposited in granular structures during the initial deposition, which subsequently converted into Li_2S micro-rods. The statistics showed that granular products dominated with the increasing number of deposited products, indicating that the reaction at –0.1 V was controlled by a two-step pathway. Despite the different nucleation-growth pathways at different discharge potentials, using the Lifshitz-Slyozov-Wagner model, we found that the growth rate of Li_2S micro-rods at different potentials (–0.5 V and –0.1 V) was a reaction-limited stage. The above investigation suggested that the

electrochemical deposition under both conditions was controlled by charge transfer, and the two-step pathway dominated the Li_2S deposition on the Ti electrode surface in our *in situ* EC-TEM experiments.

(5) *Characterization of droplet-like dense phase (Q7).* Droplet-like dense phase was identified through its structure, composition, and valence. HRTEM images, along with their FFT and SAED patterns revealed the droplet-like dense phase. Additionally, EDS mappings confirmed a high concentration of sulfur element in the dense phase. EELS detected its characteristic S-$L_{2,3}$ edge peaks at 173.5 eV and 180.7 eV, which were absent in the blank Li_2S_6 electrolyte, and were significantly stronger in the Li_2S nanocrystalline. S(TEM) images showed that multiple droplet-like dense phases formed on the surface of Mo NCs/N-G nanosheets, with nanoparticles exhibiting higher contrast within the dense phase areas. Through the analysis of the Z-contrast from HAADF intensity in STEM model, the contrast was differentiated into different areas of Li_2S nanocrystalline, LiPSs dense phase, Mo NCs/N-G, and the background of SiN_x and electrolyte.

(6) *Other comments (Q4, Q8, Q9).* For other valuable comments and suggestions, we have supplemented updated data and more thorough discussion, including XANES linear combination fitting of Mo oxidation states, radial Wiener filtering for HRTEM images, AIMD simulation of charge transfer in LiPSs dense phase, and crystal structure of Li_2S_2.

Comment 1: *According to a very famous review paper [Niels de Jonge and Frances M. Ross, "Electron microscopy of specimens in liquid," Nature Nanotechnology, 6, 695-704, (2011)], this review paper was concerned that (1) the liquid layers were still not particularly thin, and the spatial resolution achieved was often not much better than what was available, with much less effort, through light microscopy and (2) electrodeposited nanoparticles (or rods) tended to be nucleated at the top or bottom of SiN_x windows, implying that heterogeneous nucleation occurred despite researchers' willingness to observe ideal phenomena. In particular, the surface functionality of SiN_x windows, such as hydrophobic or hydrophilic conditions, can influence the nucleation behaviour of LiPSs, as mentioned by the reference paper [Guangyuan Zheng, Yi Cui et al., "Amphiphilic Surface Modification of Hollow Carbon Nanofibers for Improved*

Cycle Life of Lithium Sulfur Batteries," Nano Letters, 13, 1265-1270, (2013)]. In this regard, the authors should be aware that in situ observation using a liquid cell may not provide an accurate depiction of behaviour, so they should investigate various characterizations using in situ and ex situ analyses.

Response to Comment 1: The reviewer has provided a concise summary of the main concerns of the TEM community and the battery field regarding three key areas: (1) the image resolution in liquid cell, (2) the consistency of *in situ* and *ex situ* results, and (3) the impact of SiN_x layer on heterogeneous nucleation. In the following point-by-point responses, we aim to address your concerns and provide clarity on each of these issues.

Improvement of spatial resolution in liquid cells: Generally, the image resolution limitation in liquid cells have limited image resolution in TEM due to the chromatic aberration coefficient (C_C) caused by inelastic scattering from both the liquid layer and SiN_x window, resulting in a broader range of transmitted electron energy compared to the original spread at the source[9-11]. To improve the spatial resolution, we first reduced the liquid layer thickness by using a spacer of ~100 nm thickness to build electrochemical liquid cells. This thin liquid layer promoted the spatial resolution in liquid cells. It is worth noting that there is a trade-off between spatial resolution and liquid layer thickness. While a thin liquid layer can enhance spatial resolution, it may not accurately reflect the operando environment due to restricted reactant species and slow diffusion processes. To mitigate this effect, our *in situ* EC-TEM experiments focused on the early nucleation and growth of Li_2S rather than the long-term cycle process, thereby ensuring that reactant species were readily available. The growth rate statistics of solid Li_2S_2/Li_2S indicated that the early nucleation was reaction-limited (Fig. 2b), demonstrating that there was an abundant supply of LiPSs reactant at the electrode interfaces. Besides, after the complete deposition of Li_2S on Mo NCs/N-G nanosheets, we used an "e-beam bubble generation" method to further enhance the spatial resolution to atomic scale, which will be discussed in detail in *Response 2* (*Method for HRTEM observation in liquid cells*).

While SiN_x windows are commonly considered transparent for beam energy, thick SiN_x

windows can lead to an increased background contrast and reduced image resolution. Therefore, we investigated the impact of SiN_x window thickness on TEM image resolution by loading Li_2S@graphene on single bottom chips with different thicknesses of SiN_x windows (11.2, 48, and 94.8 nm). HRTEM images and the corresponding FFT patterns showed that in SiN_x windows with thicknesses of 48 and 94.8 nm, the background noise impeded HRTEM image resolution. By contrast, in the 11.2 nm SiN_x window, the atomic structure of Li_2S@graphene was clearly and stably observed in (111), (200), and (220) crystal planes over 103.4 s (Fig. R13). Through the modification of the thickness of the liquid layer and SiN_x window, we can therefore achieve the high-resolution observation in liquid cells.

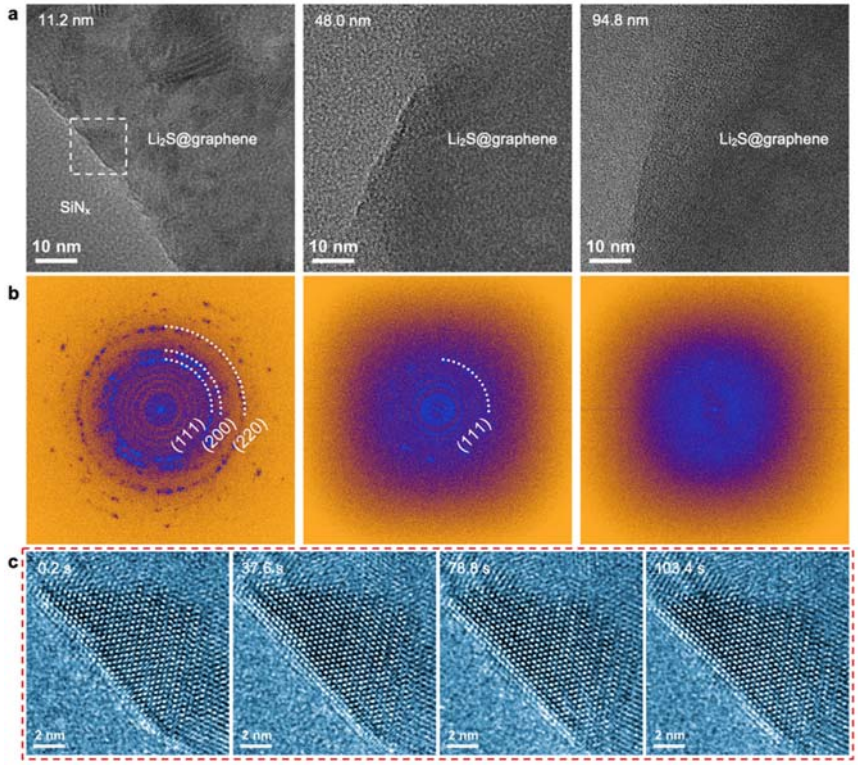

Fig. R13 | HRTEM image resolution of Li_2S@graphene at different SiN_x thickness. (a, b) HRTEM images and corresponding FFT patterns of Li_2S@graphene loaded on single bottom chips were taken with different thicknesses of SiN_x layers (11.2, 48, and 94.8 nm). The thickness of the SiN_x layers was measured using a spectroscopic ellipsometer with a spectral range of 193~1000 nm. As the SiN_x layers increased in thickness, the spatial resolution of the Li_2S nanocrystalline degraded due to the increased background. (c) The stability of the atomic structure of the Li_2S

nanocrystalline was shown through time-series HRTEM images of Li_2S@graphene (from the red-marked frame area) at a dose rate of 18200 e $Å^{-2}$ s^{-1}.

Comparison of Li_2S structures from in situ and ex situ experiments: In our main manuscript, we utilized *in situ* EC-TEM to elucidate the interfacial reaction mechanism of LiPSs in Figs. 2-4, which was based on the apparent differences in the deposition structures of Li_2S on different electrode surfaces shown in Fig. 1, namely nanocrystalline and micro-rods. To verify the consistency and reliability of our *in situ* experimental results, we performed *ex situ* characterizations using XRD, SEM, and (S)TEM after depositing Li_2S in a coin-type cell. As shown in Fig. R14a, both the Ti mesh with and without the Mo NCs/N-G nanosheet revealed typical diffraction peaks of Li_2S at around 26.4°, corresponding to the (111) crystal plane. The Mo NCs/N-G nanosheet showed a stronger diffraction peak, indicating its higher conversion activity from soluble Li_2S_6 to solid Li_2S. The crystalline size of the deposited Li_2S can be compared qualitatively by using the Scherrer equation, $D = K\lambda/(\beta\cos\theta)$, where K is the Scherrer constant; λ is the X-ray wavelength; β is the full width at half maximum (FWHM); θ is the Bragg angle. As the crystalline size was inversely related to the β value, the Li_2S-Mo NCs/N-G nanosheet exhibited a smaller crystalline size compared to Li_2S-Ti.

The morphologies of Ti mesh, both with and without the decoration of Mo NCs/N-G nanosheet, were analyzed after Li_2S deposition. *Ex situ* SEM images indicated that the presence of Mo NCs/N-G resulted in a thicker and rougher surface after Li_2S deposition, primarily in a particle-like structure (Fig. R14b, c). By contrast, the bare Ti electrode exhibited a passivated layer covering the electrode surface, with sparse deposition of rod-like/plate-like Li_2S due to its limited nucleation sites (Fig. R14d). The difference in surface morphology was further confirmed by *ex situ* (S)TEM images, EDS mappings, and SAED patterns. Li_2S was deposited on the surface of Mo NCs/N-G nanosheet as poly-crystalline nanoparticles, primarily exposing the (111), (200), and (220) crystal planes (Fig. R15a-c), while on the bare Ti electrode surface, it was deposited as single-crystal rod-like/plate-like structures (Fig. R15d-f). It is worth noting that while there

may be variations in the size of Li_2S deposited in liquid cells and coin-type cells due to factors such as cell space, deposition time, and reactant amount, the reaction activity and deposition structure on different electrode surface remain highly consistent in both *in situ* and *ex situ* experiments.

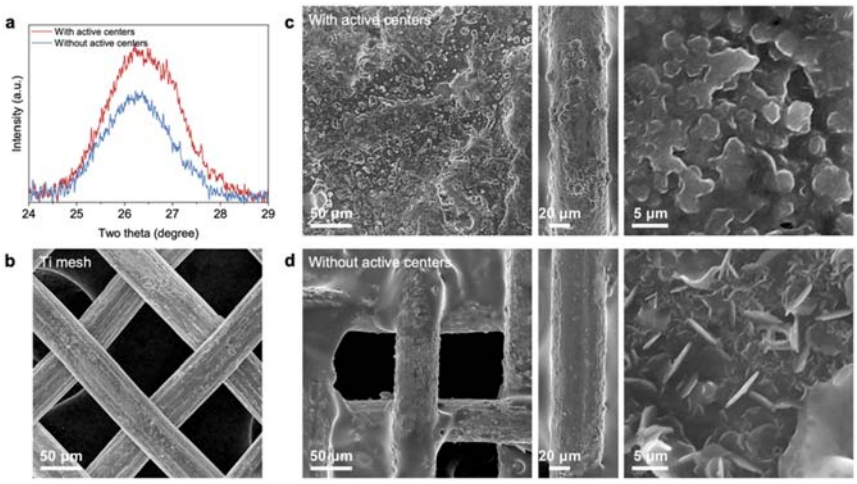

Fig. R14 | *Ex situ* XRD and SEM characterizations. (a) *Ex situ* XRD characterization of Li_2S deposited electrode with/without mediation of active centers. Li_2S electrodeposition was conducted by galvanostatic discharge at 16 μA cm^{-2} with 100 mM Li_2S_6 electrolyte in coin-type cells from OCP to 1.7 V. To avoid air exposure, the deposited cells were dis-assembled in argon-filled glovebox and re-assembled into Kapton-filmed coin-type cells. (b) SEM image of bare Ti mesh. (c, d) SEM images of Li_2S deposited Ti mesh with/without mediation of active centers.

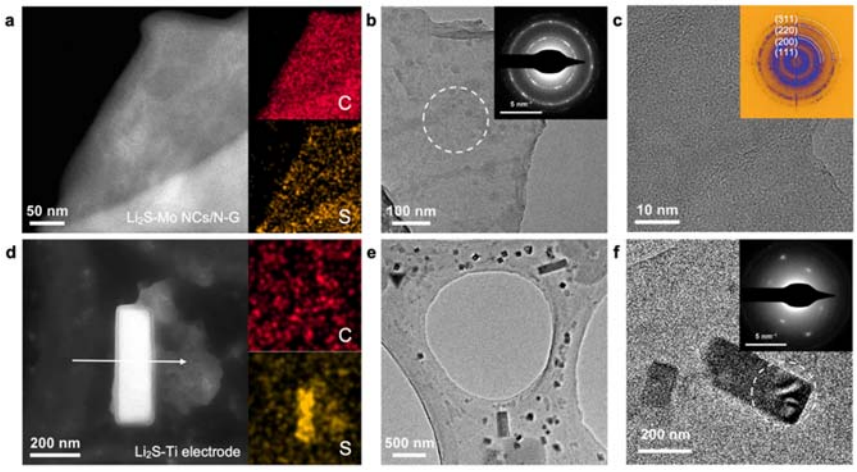

Fig. R15 | *Ex situ* (S)TEM characterization of deposited Li_2S with/without active centers. (a) *Ex situ* STEM and EDS mappings of Mo NCs/N-G nanosheet after Li_2S deposition in coin-type cells. (b, c) (HR)TEM images and the corresponding SAED and

FFT patterns of Li_2S nanocrystalline deposited on Mo NCs/N-G nanosheet. Li_2S deposition was conducted by galvanostatic discharge at 16 μA cm^{-2} with 100 mM Li_2S_6 electrolyte in coin-type cells from OCP to 1.7 V. (d) *Ex situ* STEM images and EDS mappings of Li_2S micro-rod deposited on bare Ti electrode. (e, f) TEM images and the corresponding SAED pattern of Li_2S micro-rods. Li_2S deposition was conducted by the same galvanostatic discharge.

SiN_x effects on the electrochemical deposition: The surface functionality of SiN_x has a significant impact on the surface liquid layers, and can trigger heterogeneous nucleation of crystals at high e-beam dose rates. However, it should be noted and distinguished that the surface properties of SiN_x are largely different from those of carbon nanofibers mentioned by the referee, because the latter is an electrode material with good conductivity, and LiPSs can undergo electrochemical reactions directly on its surface. By contrast, SiN_x is an insulating material that typically lacks conductivity. To investigate the SiN_x effect on electrochemical deposition, we conducted discussions or experiments in three aspects: liquid cell preparation, e-beam effect, and *ex situ* characterization in coin-type cells.

Initially, SiN_x layers on Si substrate are hydrophobic after production and are vulnerable to be contaminated by organic adsorption layer. This can cause the charging of SiN_x window during electron transfer across the solid/liquid interface, due to inelastic scattering. To avoid air contamination, we prepared and assembled the liquid cells in a clean room with specialized nanofabrication setups, and conducted electrolyte injection and chip sealing in an Ar-filled glove box (H_2O<0.01 ppm, O_2<0.01 ppm). Next, we conducted a quantitative analysis of the e-beam effect on electrochemical reactions in a liquid cell under a dose rate of 1.2 e $Å^{-2}$ s^{-1} (Fig. R16a, b), which accounted for only 2.46% of the measured current density. We found that if the electric field was excluded, individual e-beam cannot drive the heterogenous deposition of Li_2S on SiN_x or Ti electrode during 164 s observation (Fig. R16c). This suggested that the charging effect of SiN_x window was negligible. Instead, Li_2S deposition mainly occurred on the electrode interface during potentiostatic discharge, due to the necessity of charge transfer for LiPSs electrochemical reactions, which can only be driven by an electric

field, not an e-beam. Similar electrochemical behavior at electrode/electrolyte interface under low dose rates has also been reported in the deposition of Li metal or SEI layer[12-15]. Finally, we constructed a SiN_x layer via plasma enhanced chemical vapour deposition (PECVD) on a Ti current collector to investigate the effect of SiN_x layer on electrochemical reactions over a larger range. After disassembling the coin-type cells, *ex situ* SEM images showed that Li_2S nucleation occurred only on the conductive Ti surface (Fig. R16d). In contrast, the conversion from Li_2S_6 to Li_2S was blocked on SiN_x surface due to its insulting properties. Overall, the above investigation revealed that the surface functionality of SiN_x layer would not affect the electrochemical conversion of LiPSs on electrode/electrolyte interfaces.

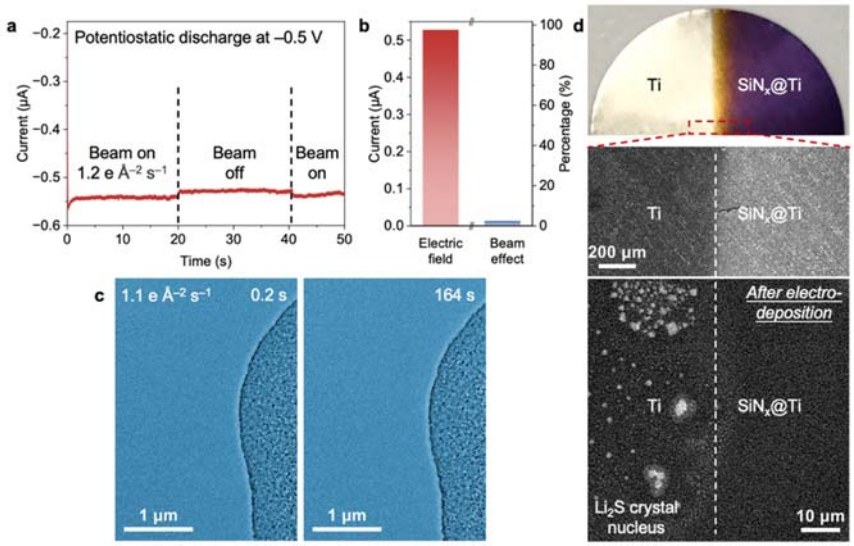

Fig. R16 | E-beam effect on the electrochemical deposition of Li_2S. (a, b) Measured current during potentiostatic discharge at –0.5 V with e-beam on (1.2 e $Å^{-2}$ s^{-1})/off. (c) Exclusion of e-beam effect on heterogenous deposition of Li_2S. (d) The digital photograph and SEM images of Ti and SiN_x@Ti surfaces before and after Li_2S deposition in coin-type cells. SiN_x layer on Ti current collector was constructed by PECVD. Li_2S deposition was conducted by galvanostatic discharge at 16 μA cm^{-2} with 100 mM Li_2S_6 electrolyte in coin-type cells from OCP to 1.7 V.

Revision to Comment 1: The corresponding contents have been added in Extended Data Fig. 1e, f and Fig. S2, 8, 29, 30. The discussions have been added in Supplementary Discussion 1, 2, and 6 (instrumental advancements for high-resolution

observation, e-beam effects, and consistency of *in situ* and *ex situ* experiments).

Comment 2: *In abstract, the authors mentioned the limitations of in situ characterization tools for tracing the reaction of unstable LiPSs with high temporal and spatial resolution. Rehman et al. (Ener. Environ. Sci., 15, 1423-1460 (2022), cited in Ref. 8) also noted that sulfur is too sensitive to the high-energy e-beams, making imaging sulfur with TEM extremely difficult. Furthermore, even cryo-EM has not revealed the atomic details and structural change of LiPSs intermediates. The authors asserted that their in-situ electrochemical TEM (EC-TEM) using an electric field instead of conventional e-beam-driven charging/discharging is superior and operates differently. However, we do not believe this mitigates the intrinsic susceptibility of sulfur (and LiPSs intermediates) to beam damage during imaging. In addition, it is well-known that Si_3N_4-based liquid TEM cells impede high-resolution imaging due to their relatively thick and high atomic number element windows with poor electron transmission. The authors should provide a reasonable explanation for the acquisition of such high-resolution TEM images of LiPSs and Li_2S, even in liquid TEM cells.*

Response to Comment 2: The issues raised by the referee are common concerns within the *in situ* TEM field, which prompted us to undertake a deeper reflection. We have endeavored to elaborate on three key aspects: (1) the e-beam effects on the LiPSs intermediates in liquid cells, (2) the e-beam damage mechanism on Li_2S, and (3) the method for HRTEM observation in liquid cells.

E-beam effects on the LiPSs intermediates in liquid cells: As noted by the reviewer, the solid discharge products and LiPSs intermediates are susceptible to e-beam damage. Time-series TEM images revealed that a medium dose rate of 11.5 e $Å^{-2}$ s^{-1} caused the decomposition after 34.4 s, with the generation of nanobubbles simultaneously (Fig. R17a). However, decreasing the dose rate to 1.54 and 1.13 e $Å^{-2}$ s^{-1} effectively prevented the side reactions over the same observation time, stabilizing both solid deposits and LiPSs electrolyte (Fig. R17b, c). Meanwhile, the spatial resolution was maintained for real-time observation. While previous e-beam-driven works have reported the deposition of Li_2S from S_8@carbon composites using carbon sphere, graphene, or carbon nanotube,[16,17] they have not observed soluble LiPSs intermediates

or metastable Li_2S_2. This is likely due to the instability of these intermediates and the susceptibility of Li_2S_n ($n \leq 2$) deposits to beam damage, which causes their decomposition. The above investigation indicates that the deposition of Li_2S triggered by an external electric field can mitigate e-beam damage to metastable intermediates during observation under low e-beam dose rates. As a result, all electrochemical studies we carried out in liquid cells were conducted with dose rates below 1.5 e $Å^{-2}$ s^{-1}.

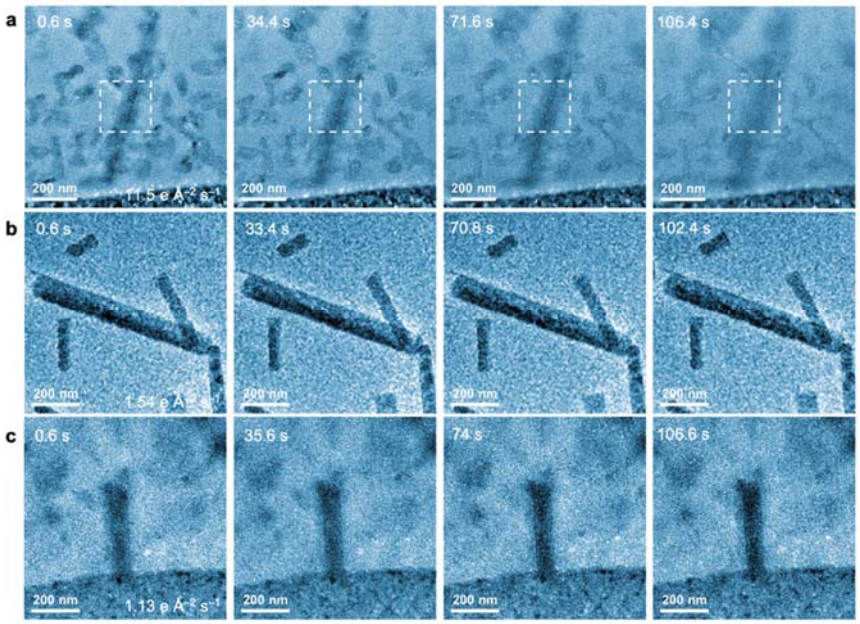

Fig. R17 | E-beam effect on the electrochemically deposited Li_2S micro-rods. (a, b) Time-series TEM images of Li_2S at the dose rates of 11.5, 1.54, and 1.13 e $Å^{-2}$ s^{-1}, respectively.

E-beam damage mechanism on Li_2S: Imaging Li-S batteries in electron microscope has always been inherently challenging[4,18], due to the spontaneous sublimation of sulfur under high vacuum, the high sensitivity of Li_2S to moisture ($Li_2S + H_2O \rightarrow LiOH + H_2S\uparrow$, Fig. R18a), and the unstable structure of LiPSs species. We first focused on the e-beam damage mechanism on Li_2S. Time-series TEM images revealed that commercial Li_2S was extremely vulnerable to e-beam, which shrank and decomposed with the generation of nanobubble inside crystal in 8.6 s under a dose rate of 69 e $Å^{-2}$ s^{-1} (Fig. R18b-d). To better understand the e-beam damage mechanism, we conducted *in situ* heating experiments on commercial Li_2S in vacuum from 20 °C to 800 °C, with

a dose rate of 3 e $Å^{-2}$ s^{-1} (Fig. R19a-c). When subjected to an individual e-beam without an increase in temperature, we observed no obvious structural variations in Li_2S over 30 s. This indicates that low e-dose observations would not cause severe structural damage (Fig. R19d). By contrast, as the temperature increased (Fig. R19e), nanobubbles appeared inside the Li_2S crystal (160.2 s), which shrank continuously (207 s), and worsened during heating up to 800°C (267.2 s). The e-beam effect on Li_2S can be mainly attributed to the ionization, radiolysis, and heating, due to its poor electrical and thermal conductivity[4,5]. However, we discovered that by simply ultrasonically mixing commercial Li_2S with graphene (Fig. R20a, b), the e-beam effect can be significantly alleviated. This should be attributed to the excellent electrical and thermal conductivity of graphene, enabling atomic-resolution and long-time observation of Li_2S@graphene. In the time-series HRTEM images (Fig. R20c), we were able to clearly observe the atomic structure of Li_2S@graphene even at a high dose rate of 11000 e $Å^{-2}$ s^{-1} and a long period of 134.6 s. Similar atomic structure of carbon-coated Li_2S have also been observed in previously reported works[19-21]. E-beam damage mechanism was further confirmed after Li_2S deposition in coin-type cells. Time-series HRTEM images revealed the stable atomic structure of Li_2S nanocrystalline deposited on Mo NCs/N-G nanosheet (Fig. R21a), while Li_2S micro-rod deposited on bare Ti electrode was highly susceptible to e-beam damage (Fig. R21b). This also explains how we were able to observe the atomic structure of Li_2S-Mo NCs/N-G after electrochemical deposition in liquid cells (Fig. 3), which will be discussed in detail in *Response 6* (*Acquisition of high-quality HRTEM images in an electrochemical liquid cell*).

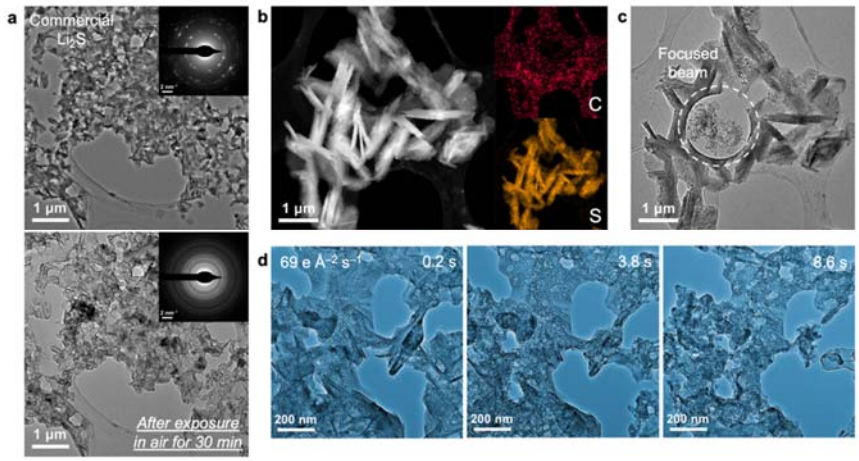

Fig. R18 | E-beam effect on commercial Li_2S. (a) TEM images of commercial Li_2S before and after exposure in air. (b) STEM image and EDS mappings of the original commercial Li_2S. (c) TEM image of commercial Li_2S after focusing e-beam at the marked area. (d) Time-series TEM images of commercial Li_2S at a dose rate of 69 e $Å^{-2}$ s^{-1}, showing sever structure damage due to the focused e-beam.

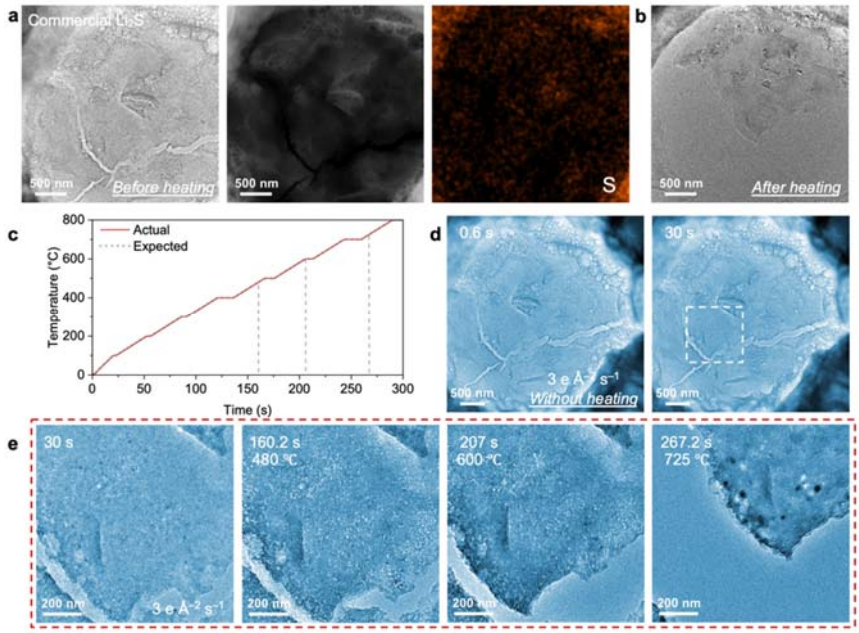

Fig. R19 | *In situ* heating of commercial Li_2S in vacuum. (a) (S)TEM images and EDS mapping of commercial Li_2S before heating. (b) TEM image of commercial Li_2S after heating in vacuum. (c) Heating time as a function of heating temperature (actual and expected). (d) Time-series TEM images of commercial Li_2S at a dose rate of 3 e $Å^{-2}$ s^{-1} without increasing temperature. (e) Time-series TEM images of commercial Li_2S at different temperature at the same dose rate of 3 e $Å^{-2}$ s^{-1}.

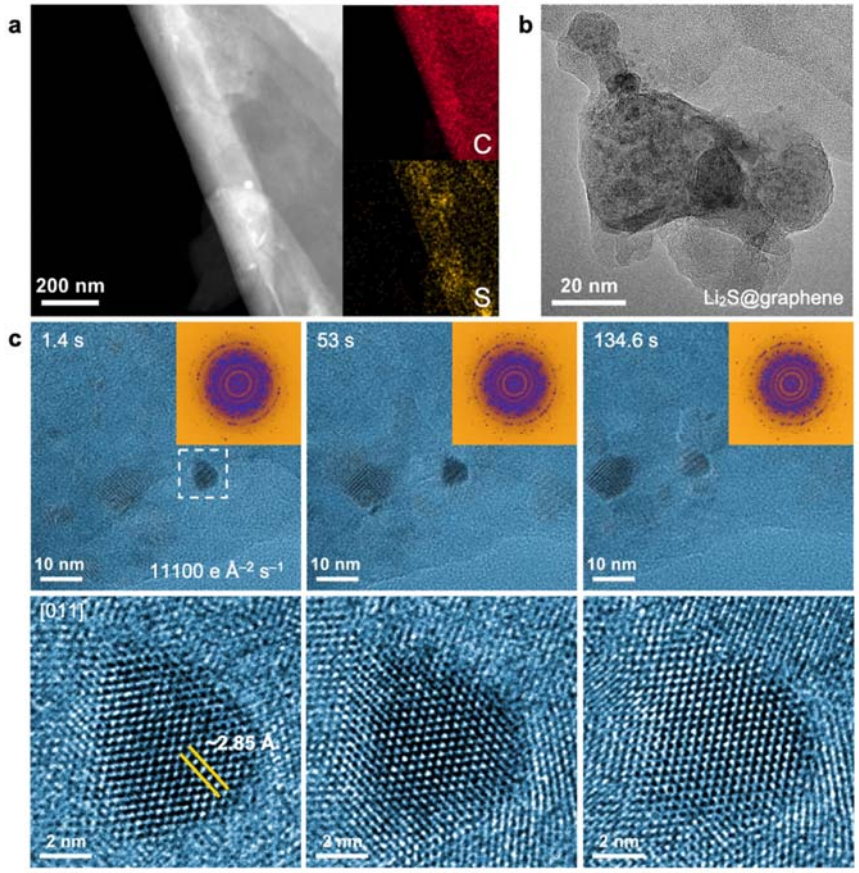

Fig. R20 | E-beam effect on Li_2S@graphene. (a, b) (S)TEM images and EDS mappings of Li_2S@graphene prepared by ultrasonically mixing commercial Li_2S with graphene in deionized water for 30 min. (c) Time-series HRTEM images, corresponding FFT patterns, and partial enlarged details of Li_2S@graphene at a dose rate of 11000 e $Å^{-2}$ s^{-1}, showing the alleviated electron damage and stable atomic structure of Li_2S nanocrystalline.

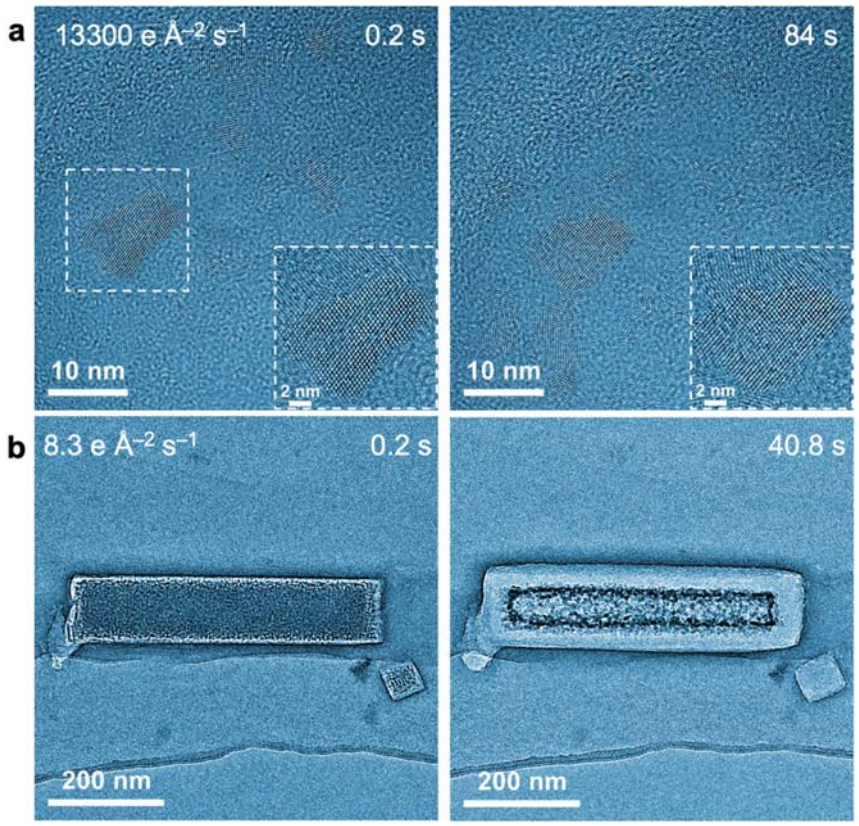

Fig. R21 | E-beam effect on Li_2S deposited in coin-type cells. (a) Time-series HRTEM images of Li_2S nanocrystalline deposited on Mo NCs/N-G nanosheet in a Cu grid. The inset is the partial enlarged details of the atomic structure. The e-beam dose rate was 13300 e $Å^{-2}$ s^{-1}. (b) Time-series TEM images of Li_2S micro-rods deposited on bare Ti electrode in a Cu grid. The e-beam dose rate was 8.3 e $Å^{-2}$ s^{-1}.

Method for HRTEM observation in liquid cells: In *Response 1*, we mainly discussed the improvement of spatial resolution during electrochemical reactions in liquid cells, by reducing the thickness of spacer and SiN_x observation windows. In addition to the instrumental advancement, we also used an "e-beam bubble generation" method to further enhance the spatial resolution experimentally by locally squeezing out the liquid layer, which had been previously adopted in our works[6-8]. E. A. Stach et al. systematically conducted a thorough analysis of the chemical and structural properties at the nanoscale level in liquid cells[22]. Their findings indicate that when a gas bubble is generated, the spatial resolution and signal-to-noise ratio (SNR) of images obtained in the thin-film condition are comparable to those observed for samples in a dry state. In

our experiments, after completing the electrochemical deposition of Li_2S nanocrystalline on Mo NCs/N-G nanosheets, we generated bubbles by focusing e-beam, adjusted their shrinkage or enlargement by changing magnification, as schematically illustrated (Fig. R22a). After generating and stabilizing the bubbles, TEM images revealed a significant reduction in the thickness of liquid layer and the background was almost transparent (Fig. R22b). If the thin-film wetting layer was completely removed (Fig. R22c, d), imaging resolution would depend on the thickness of the bottom/top SiN_x layers theoretically, thereby achieving the ultimate spatial resolution. We measured the relative thickness (t/λ, where t is the absolute thickness and λ is the mean free path) of different areas in liquid cells after bubble stabilization[23-26], as revealed by ADF-STEM and EELS images (Fig. R23a). The average values of Li_2S nanocrystalline (I) and Mo NC/N-G nanosheets (II), accounting for 0.77±0.16 and 0.29±0.02, were slightly larger than that of SiN_x layers (III) with 0.16±0.04 (Fig. R23b, c). Time-series HRTEM images revealed the atomic structure of Li_2S nanocrystalline along the [100] direction over 7.6 s (Fig. R24a, b). Above all, benefited from the efforts of both instrumental and experimental advancements, we can track the dynamic electrochemical reactions and obtain the atomic structure of the solid discharge products in liquid cells simultaneously, achieving high temporal-spatial resolution.

Meanwhile, it should be noted that concerns may arise from the uncontrollable liquid layer thickness and the strong e-beam. As a result, the improvement of resolution by generating bubbles may not accurately reflect the intended physical surroundings of the intact electrolyte. Actually, all of our *in situ* electrochemical experiments were performed at a low e-beam dose rate, specifically below 1.5 e $Å^{-2}$ s^{-1}. The structure characterization of the rod-like Li_2S deposited on Ti electrode (without active center) was also carried out at a low e-beam dose, due to its intrinsic susceptibility to e-beam damage. Atomic-scale HRTEM characterization was only conducted on the Li_2S nanocrystalline deposited on Mo NCs/N-G nanosheets after the complete electrochemical reactions, since the structure stability of Li_2S@graphene under high e-beam dose rates has already been verified.

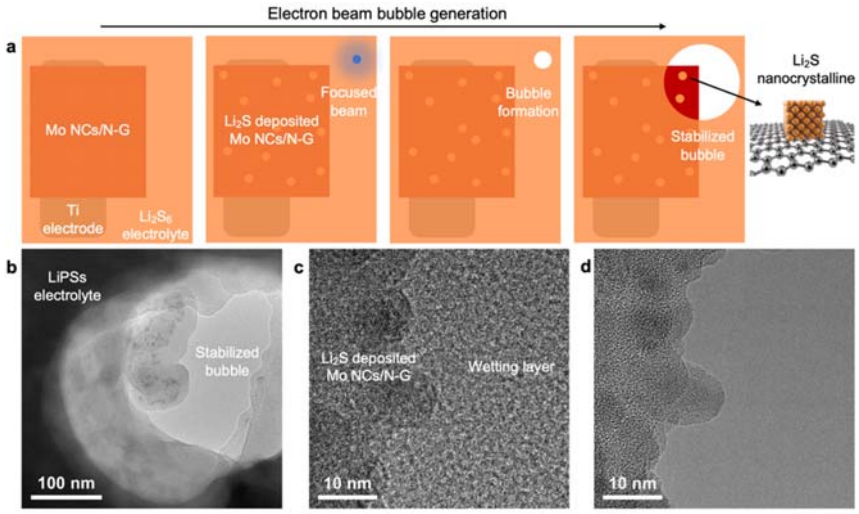

Fig. R22 | Method for HRTEM observation in electrochemical liquid cells. (a) Schematic illustration of "e-beam bubble generation" method for HRTEM observation of Li_2S nanocrystalline deposited on Mo NCs/N-G nanosheet. Following the electrochemical deposition of Li_2S in Li_2S_6 electrolyte through a potentiostatic discharge at –0.5 V for 120 s, the e-beam was focused on the bulk electrolyte, which decomposed and generated gas, forming a gas-liquid-solid triple-phase. Once the bubble area was stabilized, the atomic structure of Li_2S nanocrystalline can be obtained. (b) TEM images showing different areas of the LiPSs electrolyte, Li_2S nanocrystalline deposited on Mo NCs/N-G, and the stabilized bubble area. (c, d) HRTEM images before and after the removal of the thin-film wetting layer of electrolyte.

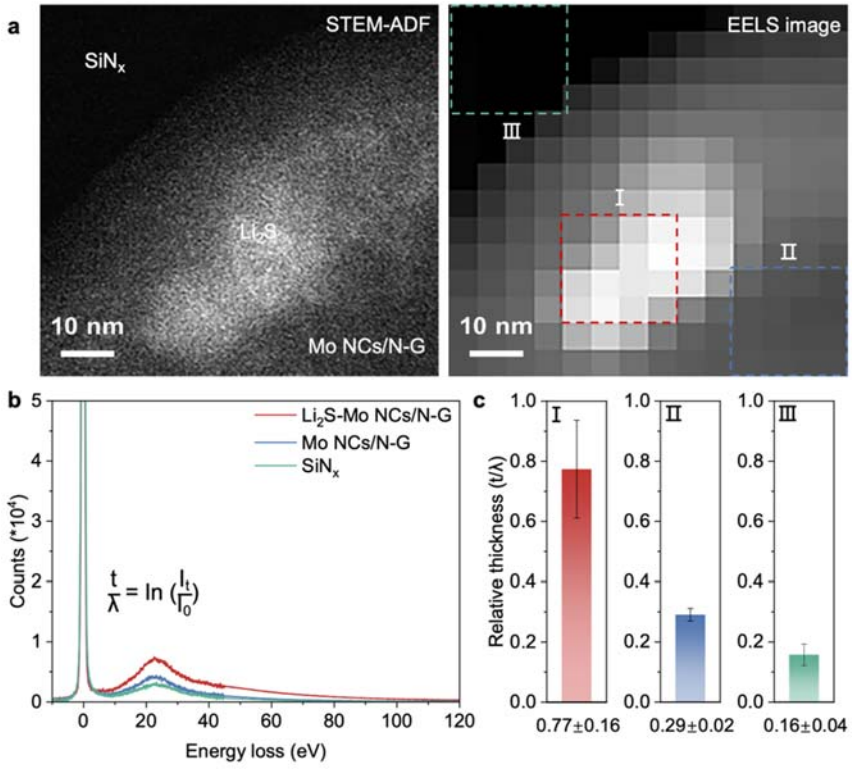

Fig. R23 | Measurement of relative thickness of electrolyte layer by EELS. (a) ADF-STEM image and the corresponding EELS image for relative thickness measurement in liquid cells. (b) Typical low-loss EELS of Li_2S nanocrystalline (I), Mo NC/N-G nanosheets (II), and SiN_x layers (III) as marked in the EELS image. (c) Average relative thickness obtained by the log-ratio method in Digital Micrograph software. The error bars were from the multiple EELS curves.

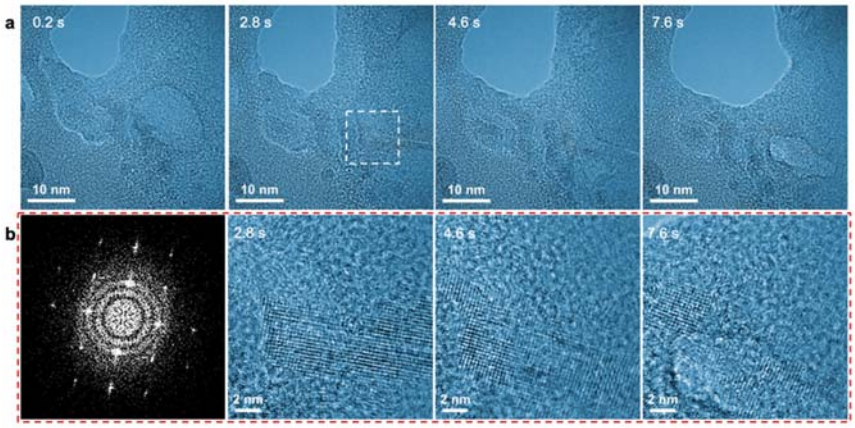

Fig. R24 | Atomic structure of Li_2S nanocrystalline in a liquid cell. (a, b) Time-series HRTEM images of Li_2S nanocrystalline deposited on Mo NCs/N-G obtained in an electrochemical liquid cell. The red frame is the corresponding FFT pattern and the partial enlarged details of Li_2S atomic structure at the same image resolution.

Revision to Comment 2: The corresponding contents have been added in Extended Data Fig. 5 and Fig. S3-7. The discussions have been added in Supplementary Discussion 2 and 3 (e-beam effects and method for HRTEM observation in liquid cells).

Comment 3: *On page 4, the authors presented two different types of nucleation-growth pathways: a single-step deposition of rod-like Li_2S and a two-step deposition via Li_2S_2. In the main text, however, the authors overlooked a single-step deposition and described a two-step deposition via Ostwald ripening in detail, which has not yet been reported. Then, can the authors statistically explain whether a two-step deposition is the dominant mechanism without active centers over a single-step one? In the same context, why is 'the depletion area' (contrast variation dur to the consumption of soluble LiPSs) invisible during a single-step deposition in extended data Fig. 2?*
In addition, the authors mentioned that "if the localized concentration of LiPSs species was sufficient, Li_2S could also be directly deposited through a single-step," showing simultaneous occurrences of a single-step and two-step deposition reaction in identical liquid TEM cells, which can be attributed to heterogeneous concentration in electrolytes. Then do the authors believe that single-step reactions preferentially occur in highly concentrated electrolytes?
- On page 4, typo (marked as particle #1 and #2 in Fig. 1b): Fig. 1b → Fig. 2b.
- On page 4, typo: Fig. 2a ↔ Fig. 2b
- Authors should provide corresponding positions in TEM images to SAED patterns of granular Li_2S_2 and rod-like Li_2S in Fig. 2c and 2e.

Response to Comment 3: Thank you for your valuable comments regarding the mechanism of different Li_2S deposition pathways over the bare Ti electrode surface. We have conducted further experiments and discussions to better address your concerns. Our efforts focused on four key aspects: (1) statistical analysis of single-step and two-step mechanism, (2) impact of electrolyte concentration on nucleation-growth pathways, (3) discussion of the depletion area, and (4) correction of typos and supplement of TEM images.

Statistical analysis of single-step and two-step mechanism: We conducted *in situ* electrochemical deposition of Li_2S on a Ti electrode surface at different discharge

potentials of –0.1 and –0.5 V, and statistically analyzed the particle size distribution and growth rate at various reaction times. At a discharge potential of –0.5 V (Fig. R25), time-series TEM images demonstrated a two-step deposition process of Li_2S micro-rods, which revealed a similar mass-redistribution of particles #7/#8 (t_0+21.4 s) and particles #9/#10 (t_0+37 s). HAADF-STEM images displayed the formation of both granular and rod-like solid discharge products on the Ti electrode surface (Fig. R26). By counting the quantities, we found that granular Li_2S_2 was slightly more prevalent than rod-like Li_2S. By contrast, when we conducted potentiostatic discharge at –0.1 V, the current density was reduced by half compared to that at –0.5 V (Fig. R27a). As revealed in Fig. R27b and c, time-series TEM images and projection area variation revealed that solid discharge products primarily nucleated in granular structures on the electrode surface during the initial deposition (0.6s and 36.6s), and gradually transformed into rod-like/plate-like structures (72.6s and 125.4s). By counting the number of solid discharge products at different discharge times, we found that granular products dominated at the early stage of deposition (Fig. R27d). As the deposition progressed, granular products transformed into rod-like/plate-like Li_2S in succession, resulting in their dominance at 125.4 s, accounting for 66.7% of the total. This reaction pathway corresponded to a typical two-step deposition process, which was further confirmed in the local enlarged detail of time-series TEM images (Fig. R27e).

We further analyzed the projection area variation of Li_2S micro-rods at various discharge potentials according to the Lifshitz-Slyozov-Wagner model (Fig. R27b and Fig. R28). It revealed that both particles depositing at –0.1 V and particles depositing at –0.5 V corresponded to the reaction-limited stages, suggesting that charge transfer at electrode surface controlled the electrochemical deposition of Li_2S_2 and Li_2S under both conditions. Since the conversion of Li_2S_6 to Li_2S ($Li_2S_6 + 10Li^+ + 10e^- = 6Li_2S$) required more electrons per unit than that of Li_2S_2 ($Li_2S_6 + 4Li^+ + 4e^- = 3Li_2S_2$), this led to the difference during nucleation-growth at −0.1 V and −0.5 V. Therefore, our findings suggest that charge transfer at the electrode-electrolyte interface primarily determined the nucleation-growth pathway of solid Li_2S_2/Li_2S. The two-step pathway is dominant during the electrochemical deposition of Li_2S on the Ti electrode surface

in our *in situ* TEM experiments.

Impact of electrolyte concentration on nucleation-growth pathways: The concerns regarding the occurrence of single-step or two-step pathways arises from whether it is determined by the charge transfer or the supply of LiPSs species. When the discharge potential was adjusted to –0.1 V with the same electrolyte concentration, the solid discharge products primarily deposited in granular structures during the initial stage, which consecutively transformed into rod-like/plate-like structures during the deposition. Through a statistical analysis of growth rate at different discharge potentials, we found that the deposition of particles (#1, #2, #3, #4) at –0.5 V (Fig. S12 and Fig. R28) and particles (#5, #6) at –0.1 V (Fig. R27b) both corresponded to reaction-limited stages. Therefore, it suggests that it was the charge transfer at the electrode surface, rather than the concentration of LiPSs species, controlled the nucleation-growth of solid Li_2S_2/Li_2S through either a single-step or a two-step pathway. The electrochemical deposition of Li_2S preferred to undergo a two-step pathway intrinsically at 0.1 V. According to the referee's insightful comment and additional experiment, we have revised the description in the updated version.

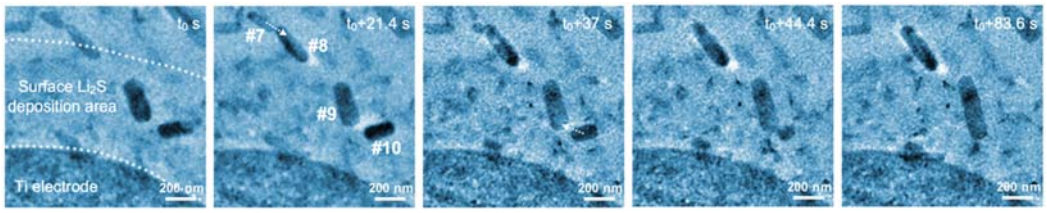

Fig. R25 | Two-step deposition of Li_2S at –0.5 V without mediation of active centers. Time-series TEM images showing two-step Li_2S deposition in liquid-cell EC-TEM. TEM image (t_0 s) revealed solid Li_2S deposited on the surface of Ti electrode. The moving direction is indicated by the dotted single-sided arrows (t_0+21.4 s).

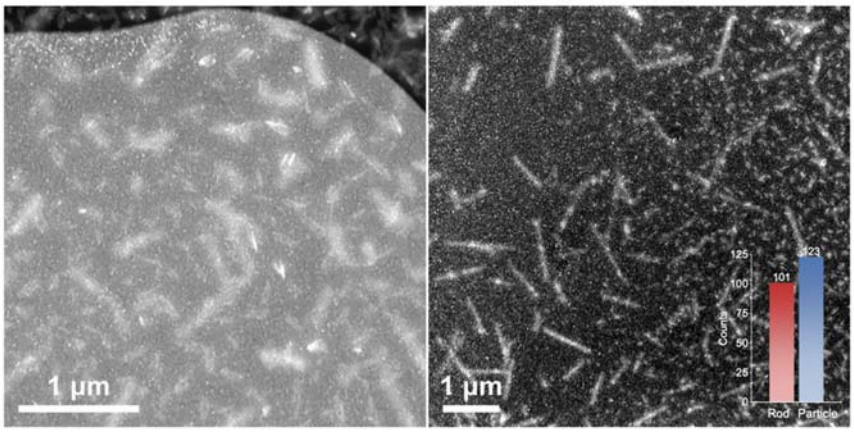

Fig. R26 | Statistical analysis of deposited Li_2S at –0.5 V without mediation of active centers. STEM images and the corresponding statistics of granular and rod-like products.

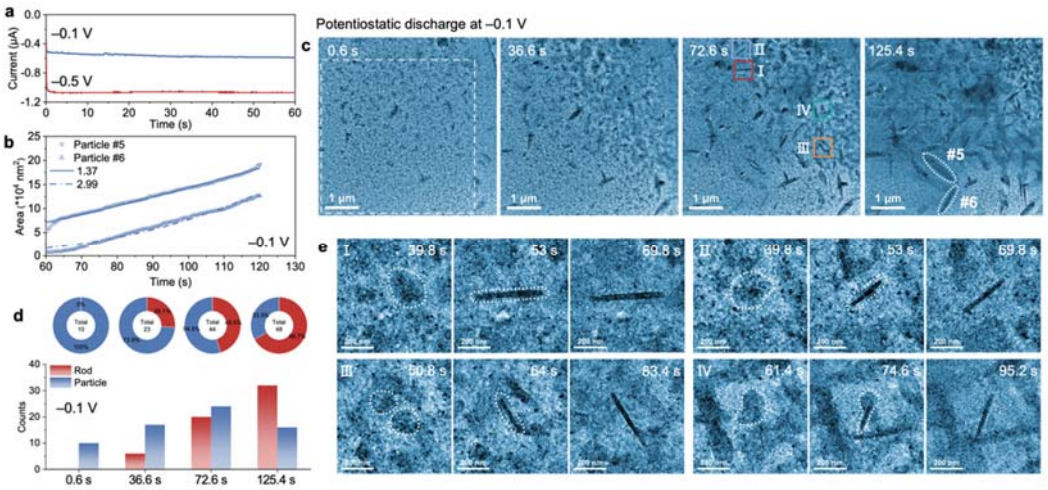

Fig. R27 | Deposition of Li_2S at –0.1 V without mediation of active centers. (a) The applied electric field of electrochemical liquid cells with different discharge potentials of –0.1 and –0.5 V, respectively. (b) The projection area variation as a function of time of particles #5 and #6 in Fig. R27c. (c) Time-series TEM images from Supplementary Movie S3 showing two-step Li_2S deposition in liquid-cell EC-TEM. (d) Statistics of rod and particle quantity at specific times corresponding to the white frame areas in Fig. R27c (discharge at –0.1 V). (e) Time-series TEM images of typical two-step deposition of Li_2S via metastable Li_2S_2 (marked by white dotted lines). TEM images of I-IV corresponded to the typical areas in Fig. R27c (72.6 s).

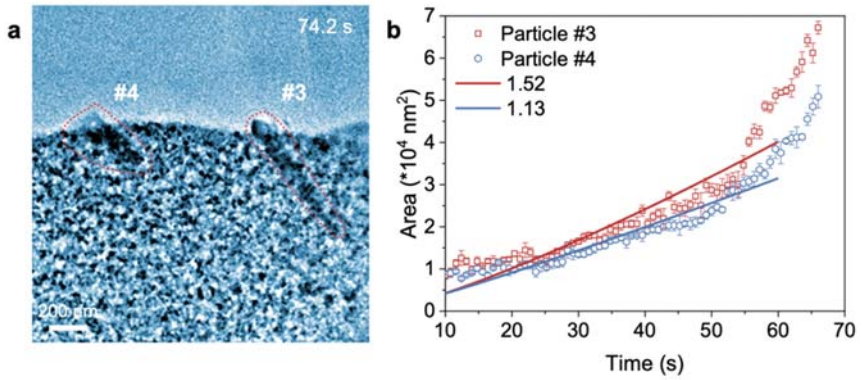

Fig. R28 | Statistics of Li_2S deposition without mediation of active centers through a single-step pathway. (a) Area variation of particles #3 and #4 as a function of time during potentiostatic discharging through a single-step pathway. A power function was used to fit the area variation over time (Area $\propto t^n$) according to LSW model, where $n \geq 1$ represents reaction-limited growth, and $n<1$ represents diffusion-limited growth.

Discussion of the depletion area: The formation of the depletion area is primarily attributed to the dramatic decrease in the concentration of LiPSs electrolyte in a localized area, coupled with the sluggish diffusion rate of reactants at the electrode/electrolyte interface that cannot supply timely. In Fig. 2b, we observed the appearance of a depletion layer during the mid-to-late stages of the two-step deposition process. This occurred at the same time as we observed a slowing down or halting of the growth of granular particles #1 and #2, as indicated by the turning point in the projection area variation (Fig. 2a). By contrast, solid discharge products (particles #3 and #4) showed uniform growth in the single-step pathway (Fig. R28), suggesting that the reactant at the interface was not significantly reduced and therefore no depletion layer was observed. Therefore, it is important to note that the appearance of depletion layers is random at micro-/nano- scales, and there can be inconsistency in local observation areas.

Correction of typos and supplement of TEM images: We are very sorry for the typos in the manuscript and the missing TEM images of SAED patterns. We have corrected the typos on page 4. The TEM images of granular Li_2S_2 and rod-like Li_2S corresponding to SAED patterns in Fig. 2 has been provided (Fig. R29).

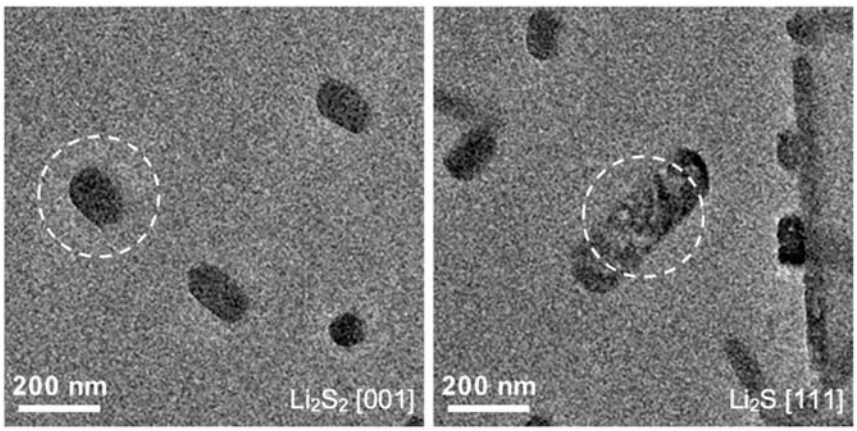

Fig. R29 | TEM images of SAED patterns of Li_2S_2 and Li_2S. TEM images of SAED patterns of granular Li_2S_2 and rod-like Li_2S in Fig. 2c and 2e.

Revision to Comment 3: The corresponding contents have been added in Extended Data Fig. 3 and Fig. S10-13. The discussions have been added in manuscript (page 6, line 1-13).

Comment 4: *In extended data Fig. 5, the authors analyzed the oxidation states of Mo using XANES and XPS. They claimed the existence of Mo^{4+} and Mo^{6+} using XPS peak deconvolution, but they did not provide any related references. In addition, it is well-known that XANES is a much more precise tool than XPS to detect the oxidation state of transition metals. Therefore, the estimation of oxidation states of Mo should be based on XANES analysis.*

Response to Comment 4: We agreed with the referee's comments that XANES is more sensitive and precise in detecting the bulk oxidation state and coordination environment of transition metals than XPS. As a result, we used the Mo 3d XPS spectrum to analyze the valence state of metallic Mo. We observed three main peak areas in the Mo 3d XPS spectrum, marked in red, blue, and green colors, which indicated different oxidation states (Fig. R30a). We further split them into the doublet peaks at 228.48 and 229.88 eV (Mo^0), 231.58 and 233.68 eV (Mo^{4+}), and 234.88 and 236.48 eV (Mo^{6+}) corresponding to Mo $3d_{5/2}$ and Mo $3d_{3/2}$[27-30]. Then, we employed linear combination fitting on the XANES result to quantitatively analyze the weight percentage of valence states of Mo^0, Mo^{+4}, and Mo^{+6}, by using Mo-foil, MoO_2, and MoO_3 as the standard

samples (Fig. R30b and Fig. R31a). The percentage of Mo^{0}, Mo^{+4}, and Mo^{+6} in Mo nanoclusters were 10%, 57%, and 33%, respectively (Fig. R31b), which are similar as that by XPS analysis.

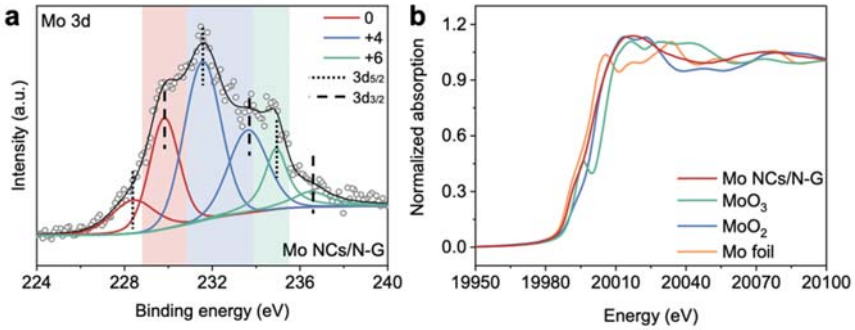

Fig. R30 | (a) Mo 3d XPS spectrum of Mo NCs/N-G. (b) XANES of Mo NCs/N-G and reference samples of Mo-foil, MoO_2, and MoO_3.

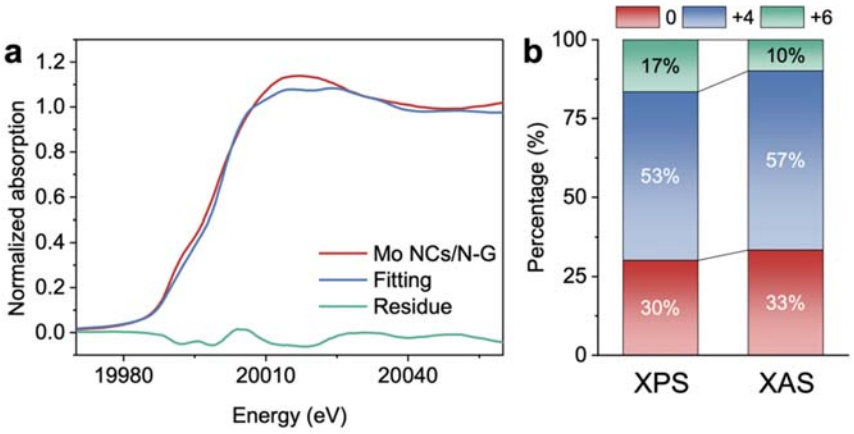

Fig. R31 | (a) XANES linear combination fitting of Mo NCs/N-G, using the reference samples of Mo-foil, MoO_2, and MoO_3. The fitting residual is expected due to the different coordination of Mo nanoclusters in Mo NCs/N-G compared to those in Mo-foil, MoO_2, and MoO_3. (b) Percentage of Mo nanoclusters in Mo NCs/N-G with different valence of Mo^{0}, Mo^{+4}, and Mo^{+6}, which were calculated based on Mo 3d XPS spectrum and XANES linear combination fitting. The valence distribution acquired through XANES linear combination fitting was verified by results obtained by the integrated areas of XPS peaks, and the slight difference should be attributed to the detection depth of the characterization techniques.

Revision to Comment 4: The corresponding contents have been added in Fig. S16 and 17. The discussions have been added in manuscript (page 6, line 25-28).

Comment 5: *As mentioned above, the authors should provide corresponding sample imaging positions at a low magnification for HR-TEM images in Fig. 3i.*

Response to Comment 5: HRTEM images in Fig. 3i were obtained after a potentiostatic discharge at –0.5 V, as shown in Fig. 3d and Supplementary Movie S4. While we provided HRTEM images of Li_2S-Mo NCs/N-G at a lower magnification (Fig. R32), it did not reveal a larger observation area after the complete electrochemical deposition and e-beam bubble generation.

Given the feasibility of obtaining atomic-scale HRTEM images of Li_2S-Mo NCs/N-G by using a 10 nm SiN_x window liquid cell, we repeated the electrochemical deposition of Li_2S on Mo NCs/N-G nanosheets and obtained TEM images at different magnifications. The low-magnification TEM image after e-beam bubble generation demonstrated that the background was almost transparent while Li_2S-Mo NCs/N-G remained intact (Fig. R33a). We further obtained high-resolution time-series HRTEM images of Li_2S nanocrystalline on the surface of the Mo NC/N-G nanosheet (Fig. R33b, c), showing the atomic structure of Li_2S nanocrystalline along the [100] direction. Detailed discussion of the conditions for obtaining HRTEM images will be presented in *Response 6*.

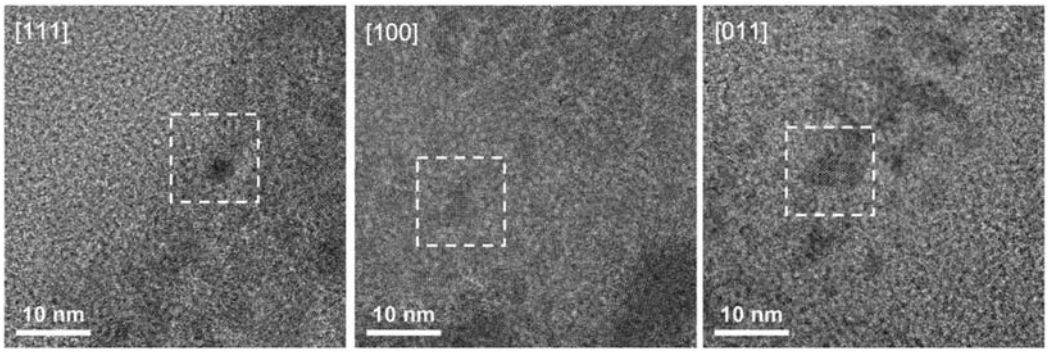

Fig. R32 | HRTEM images at a lower magnification. HRTEM images of Li_2S nanocrystalline deposited on Mo NCs/N-G in a liquid cell, along [111], [100], and [011] directions.

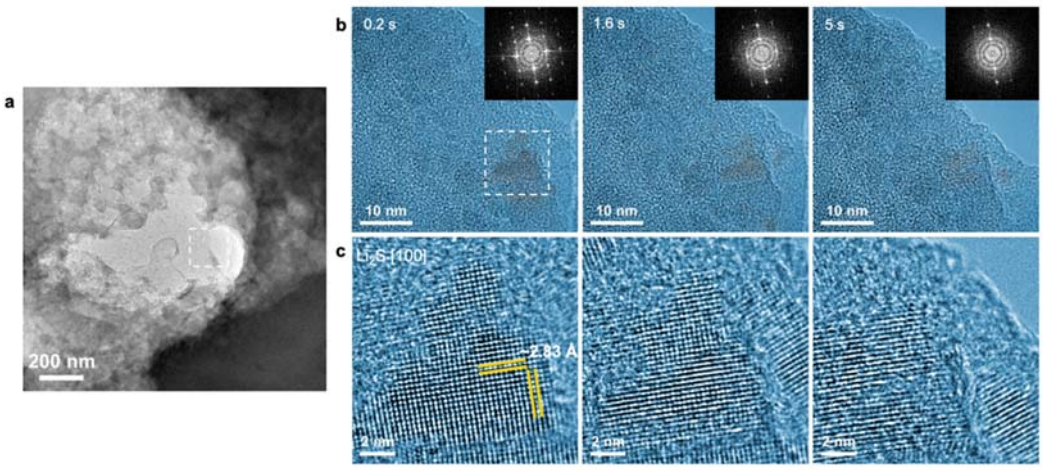

Fig. R33 | TEM images after Li_2S electrochemical deposition and e-beam bubble generation. (a) TEM image of Li_2S nanocrystalline deposited on Mo NCs/N-G in a liquid cell. Atomic-structure observation area of Li_2S-Mo NCs/N-G was marked by the red frame. (b, c) Time-series HRTEM images, the corresponding FFT patterns, and the partial enlarged details of Li_2S nanocrystalline deposited on Mo NCs/N-G obtained in an electrochemical liquid cell.

Revision to Comment 5: The corresponding contents have been added in Extended Data Fig. 5i and Fig. S20.

Comment 6: *Obtaining images with atomic resolution for Fig. 3i is extremely challenging. The experimentally acquired images appear to have undergone noise cancellation. Please include raw data for Fig. 3i in the supplementary information or extended Figures. In addition, the authors should elaborate on the experimental conditions in this section. The reviewer is concerned that disagreements will arise if this manuscript is later published. Therefore, the authors should illuminate how to acquire high-resolution images under unfavorable conditions of strong e-beams, thick electrolytes relative to LiPSs, and relatively high atomic numbers relative to LiPSs.*

Response to Comment 6: We would like to express our sincere appreciation for the valuable comment and suggestion. Before discussing the HRTEM image of Li_2S-Mo NCs/N-G, it is important to note that atomic-scale and high-resolution observation was only conducted on Li_2S-Mo NCs/N-G after the complete electrochemical deposition. The structure of solid Li_2S_2/Li_2S on Ti electrode surface was studied by SAED patterns

under low e-beam dose rates due to their high e-beam susceptibility. Therefore, we summarized the acquisition of high-quality HRTEM images in an electrochemical liquid cell into the four key aspects, including: (1) configuration of liquid cell (spacer and SiN_x layer), (2) thickness of liquid layer (bubble generation), (3) image acquiring conditions (image resolution, exposure time), and (4) post-image processing (radial Wiener filter).

First, we applied a 100 nm-thick spacer to assemble the bottom and top chips of liquid cells, and constructed a ~10 nm SiN_x window cell, which helped improve spatial resolution and minimized the impact of background noise. The instrumental advancement has been discussed in detail in *Response 1* (*Improvement of spatial resolution in liquid cells*). Second, we used an "e-beam bubble generation" method to locally squeeze out the liquid layer after the complete electrochemical deposition and investigate the atomic structure of Li_2S-Mo NCs/N-G. The method and the quantitative analysis of relative thickness has been provided in *Response 2* (*Method for HRTEM observation in liquid cells*). While graphene has been shown to reduce beam damage of Li_2S nanocrystalline in both *in situ* and *ex situ* experiments, it is still important to keep the e-beam at a relatively low dose rate, to ensure the stability of the liquid layer during HRTEM image acquisition. Third, for image acquiring conditions, we used the FEI Talos-F200s TEM operating at 200 kV. The HRTEM image was captured using Velox software at a dose rate of ~10000 e $Å^{-2}$ s^{-1}, with a resolution of 4096×4096 pixels and an exposure time of 500 ms.

Last but not least, to mitigate the impact of carbon contamination and amorphous SiN_x layer-induced background noise in HRTEM images of Li_2S nanocrystals, we utilized the radial Weiner filter for post-image processing, with the highest frequency of 80 and edge smoothing of 5%. While a simple Fourier space periodic mask is commonly used to extract crystal structure, this method can introduce artifacts or periodic features that are not part of the crystal structure. Therefore, we employed the radial Wiener filter to eliminate amorphous background noise[31,32]. This method estimates the background by taking the average value after excluding the intensity corresponding to Bragg diffraction from periodic structures, and it calculates the rotation average of the Fourier

transform of the entire image. The HRTEM images in Fig. 3i before and after applying the radial Wiener filtering, and the corresponding FFT patterns, were provided in Fig. R34. The original FFT patterns of Li_2S nanocrystalline showed concentric rings corresponding to diffraction patterns of non-crystalline materials (I). These ring patterns were caused by non-periodic parts of the image arising from amorphous surface layers. The Fourier transform (F_o) of the observed image is the sum of the true signal from the crystalline part (F_c) and the non-periodic background from the non-crystalline part (F_b), represented as $F_o = F_c + F_b$. The true signal F_c is limited to diffraction spots and is typically strong, while the non-periodic background F_b is more uniformly distributed. The Wiener filter seeks a solution that minimizes the sum of the square differences between the true signal F_c and its estimated value $\hat{F}_w$ ($\sum|\hat{F}_w - F_c|^2 \rightarrow$ minimum). As a result, after radial Wiener filtering, the concentric rings from non-crystalline surface layers were greatly reduced, while diffraction spots from the periodic Li_2S nanocrystalline were preserved in the processed HRTEM images and FFT images (II).

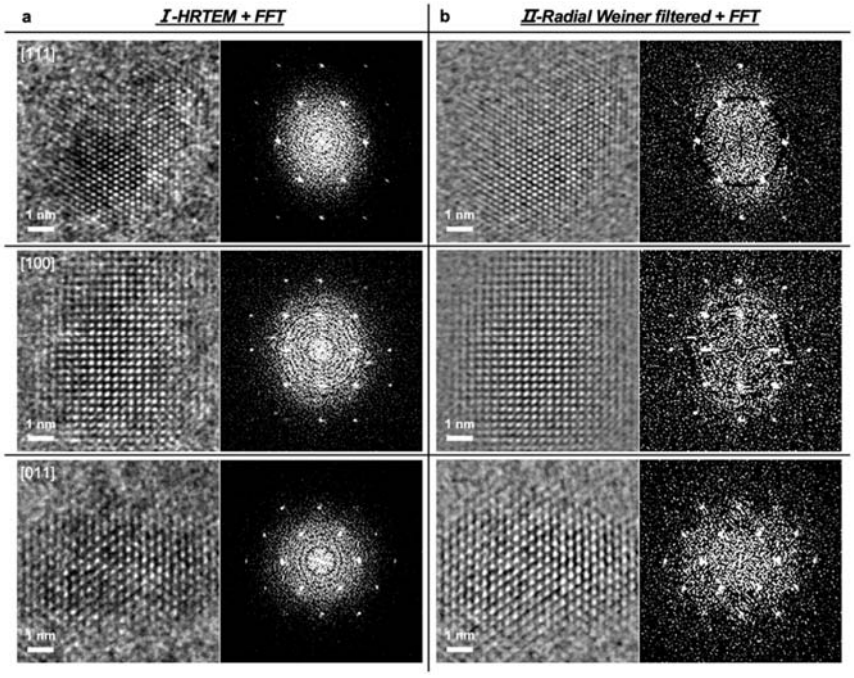

Fig. R34 | Post-image processing of Li_2S atomic structure by radial Weiner filter. The raw data of HRTEM images in Fig. 3i before and after radial Wiener filtering, as

well as the corresponding FFT patterns.

Revision to Comment 6: The corresponding contents have been added in Fig. S21. The discussions have been added in Supplementary Discussions 4 (image acquiring conditions and post-image processing).

Comment 7: *On page 7, I believe that the term 'non-equilibrium' Li_2S means polycrystalline (or amorphous) products in Mo-NCs/N-G, in contrast to single-crystal Li_2S in a bare electrode. Additionally, the authors mentioned that multiple droplets (shown in Supplementary Movie. S6) should not be assigned to crystallized or nucleated Li_2S_2/Li_2S. I do not support the idea that the multiple droplets are highly concentrated Li_2S_n ($2<n<6$) from TEM images. The authors should provide a reasonable explanation as to why they recognized that this behaviour is distinct from conventional step-by-step reaction.*

Response to Comment 7: Thank you for your concern regarding the composition of the droplet-like dense phase and its impact on the conversion pathway of LiPSs. In order to confirm the structure and composition of the droplet-like dense phase, we conducted a comprehensive investigation using high-resolution S(TEM) images, SAED patterns, EDS mappings, and EELS.

Characterization of droplet-like dense phase: After a potentiostatic discharge at –0.5 V for 100 s, HRTEM images were obtained, along with their FFT and SAED patterns. The results revealed the droplet-like dense phase and the crystallized structure of Li_2S nanocrystalline (Fig. R35a, b). HAADF-STEM images, EDS mappings and linear elemental analysis confirmed a higher concentration of sulfur in both structures (Fig. R35c, d). EELS were also performed to differentiate the concentrated droplets from the crystallized Li_2S (Fig. R35e). The characteristic sulfur near-edge peaks, $L_{2,3}$ edges (2p to unoccupied 3d orbitals) and L_1 edges (2s to unoccupied 3d orbitals), were found at 162-185 eV and 238 eV, respectively[16,33,34]. These peaks were absent in the bulk electrolyte, but were identified in the droplet-like dense phase with two peaks at 173.5 eV and 180.7 eV. The S-$L_{2,3}$ and S-L_1 edges peaks in the Li_2S nanocrystalline were

significantly stronger and showed a chemical redshift compared to the droplet-like dense phase, which should be attributed to the electrochemical reduction and conversion from S_n^{2-} ($2<n<6$) to S^{2-}.

Besides, we conducted a wider range observation in both bright field and dark field to investigate the structure of droplet-like dense phase. TEM and HAADF-STEM images showed that multiple droplet-like dense phases formed on the surface of Mo NCs/N-G nanosheets (Fig. R36). To solve the scattering and artifacts in HRTEM images resulting from amorphous SiN_x windows, disordered electrolyte, and the contrast transfer function of the electron microscope, a Gaussian filter was applied to suppress high-spatial frequency noise and enhance the boundary of dense phase areas. Both raw and post-processed HRTEM images confirmed the structure of nanoparticles inside dense phase areas (Fig. R37a, b). The contrast of the HAADF-STEM image, which is positively correlated with atomic number (Z), is determined by the elastically scattered electrons reaching the HAADF detector. In our analysis, we found that Li_2S nanocrystalline exhibited a higher contrast compared to droplet-like dense phase, as the former was the FCC close-packed structure of Li^+ and S^{2-} ions, while the later was the mixed structure of ions and solvent molecules. From the linear analysis of HAADF intensity, the contrast contribution can be attributed to Li_2S nanocrystalline, LiPSs dense phase, electrolyte, and the background, respectively (Fig. R37c-e). This was further confirmed in multiple areas and the linear HAADF intensity analysis. The results revealed that Li_2S nanocrystalline had a sharper and higher intensity, while LiPSs dense phase exhibited a more fluctuant and weaker intensity (Fig. R38). Therefore, based on the investigation of both chemical composition, valence state and image contrast, we can confirm that the droplet-like dense phase is the highly concentrated Li_2S_n ($2<n<6$).

Discussion of collective charge transfer behavior compared with step-by-step mechanism: In our *in situ* EC-TEM experiments, we observed that the reaction at bare Ti electrode surface followed a step-by-step nucleation-growth process: (Step-I) the formation of Li_2S_2/Li_2S nuclei, (Step-II) the continuous growth of Li_2S micro-rods. Conversely, at Mo NCs/N-G nanosheet surface, we observed that the gathering of LiPSs

induced the direct Li_2S crystallization. No other soluble or insoluble intermediates were formed during this process, indicating that LiPSs reacted as a whole in the droplet-like dense phase, and transformed directly from the LiPSs dense phase into crystallized Li_2S. Since the conversion from soluble Li_2S_6 to Li_2S requires sustained electron transfer ($Li_2S_6 + 10Li^+ + 10e^- = 6Li_2S$), the gathered LiPSs should be continuously reduced under an electric field. Based on the supplemented structural characterization (HRTEM, SAED, EDS, EELS) of LiPSs droplets and Li_2S nanocrystalline, we further confirmed the direct transformation of LiPSs dense phase into crystallized Li_2S.

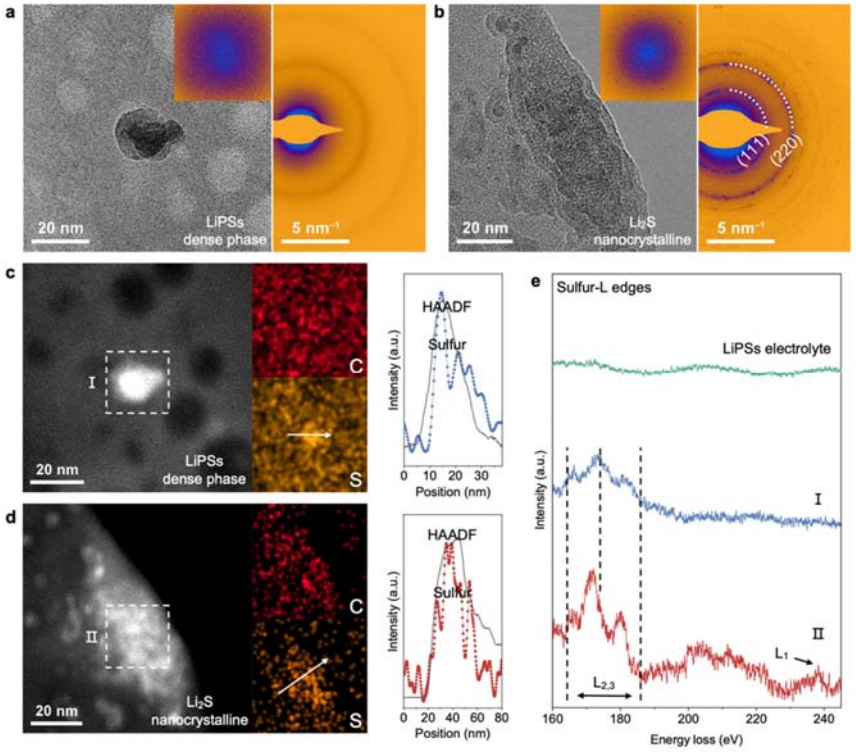

Fig. R35 | Characterization of LiPSs dense phase from structure and element. (a, b) TEM images, along with the corresponding FFT and SAED patterns of LiPSs droplet and Li_2S nanocrystalline. (c, d) STEM images, EDS mappings and the corresponding linear elemental analysis of LiPSs droplet and Li_2S nanocrystalline. (e) EELS of the sulfur L edges of blank LiPSs electrolyte, LiPSs droplet (area I in Fig. R12c), and Li_2S nanocrystalline (area II in Fig. R12d). The EELS were processed according to the following steps: zero-loss peak calibration, background removement (power law), and plural scattering removement (Fourier-ratio).

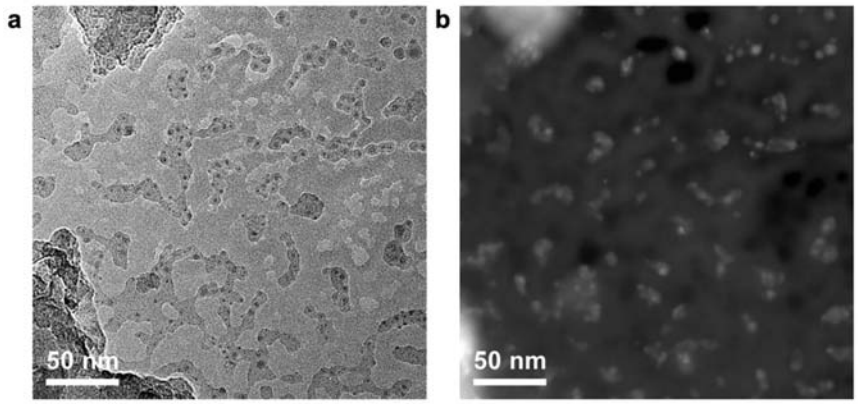

Fig. R36 | Characterization of LiPSs dense phase. (a, b) TEM and HAADF-STEM images of Mo NCs/N-G nanosheet after electrochemical deposition in electrochemical liquid cell, showing the LiPSs dense phase and Li_2S nanocrystalline.

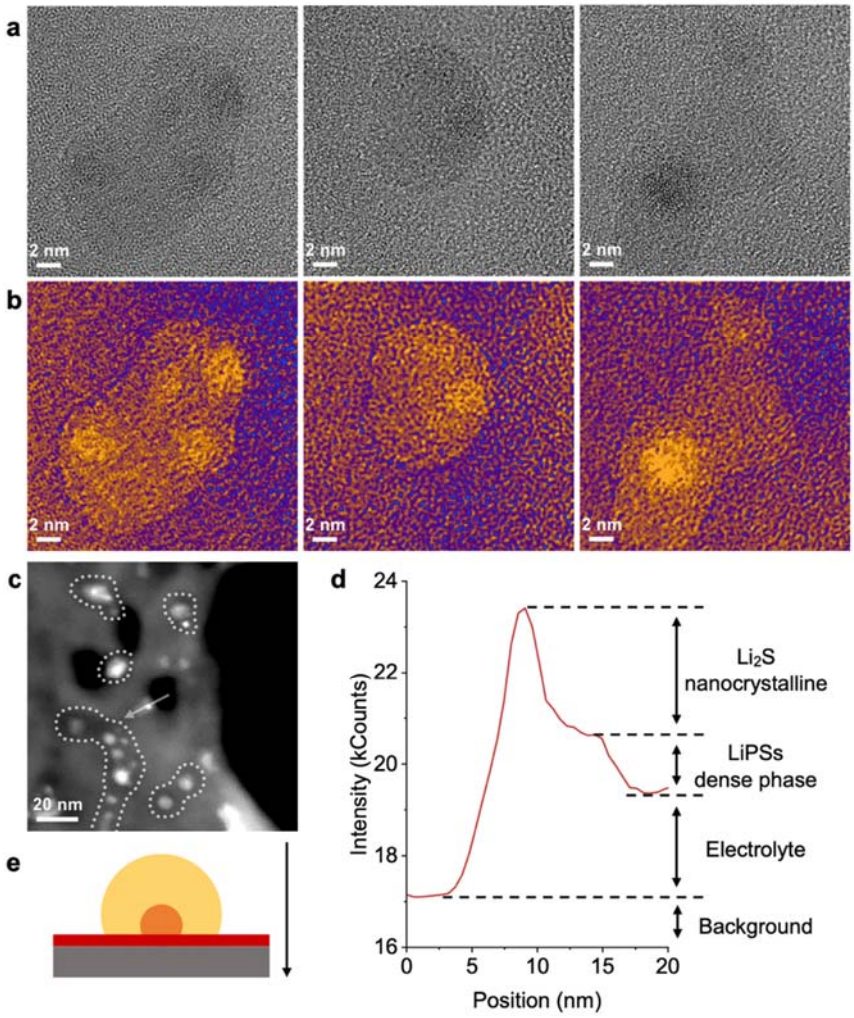

Fig. R37 | Characterization of LiPSs dense phase from HAADF intensity. (a, b) Raw and post-processed HRTEM images using a Gaussian filter. To solve the scattering

and artifacts in HRTEM images resulting from amorphous SiN_x windows, disordered electrolyte, and the contrast transfer function of the electron microscope, a Gaussian filter was applied to suppress high-spatial frequency noise and enhance the boundary of dense phase areas. (c, d) Partial enlarged details of HAADF-STEM image and the corresponding linear HAADF intensity analysis. The areas of LiPSs dense phase were marked by the white dotted lines. The linear HAADF intensity analysis was marked by the white arrows. The particles with brighter contrast in the dense phase areas were Li_2S nanocrystalline. (e) Schematic illustration of the path of scattered electrons.

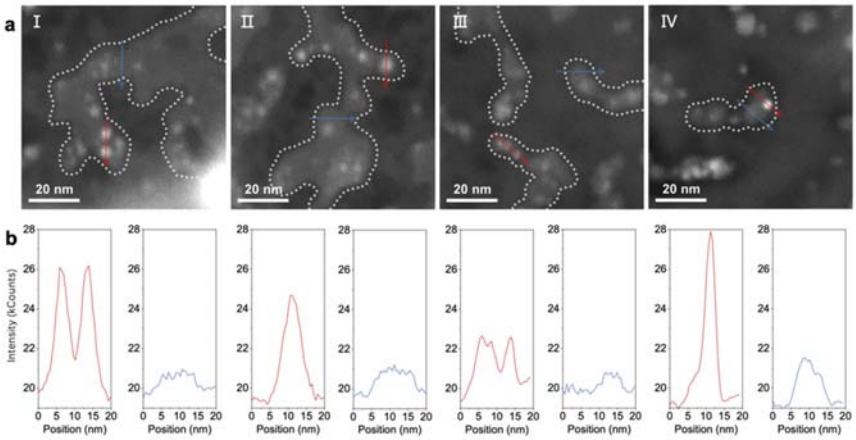

Fig. R38 | Confirmation of LiPSs dense phase from HAADF intensity. (a, b) Partial enlarged details of HAADF-STEM images and the corresponding linear HAADF intensity analysis. The areas of LiPSs dense phase were marked by the white dotted lines. The particles with brighter contrast in the dense phase areas were Li_2S nanocrystalline. The red and blue arrows/curves corresponded to Li_2S nanocrystalline and LiPSs dense phase, respectively.

Revision to Comment 7: The corresponding contents have been added in Fig. 4c, Extended Data Fig. 7, and Fig. S22, 23. The discussions have been added in manuscript (page 8, line 25–page 9, line 8).

Comment 8: *How is it verified in DFT calculations that the strong interaction between Mo active centers and LiPSs droplets successfully suppresses the step-by-step evolution of soluble LiPSs and causes the instantaneous crystallization of Li_2S?*

Response to Comment 8: From the experimental results of *in situ* EC-TEM, the long-range interaction of Mo active center with LiPSs enabled the gathering of soluble LiPSs

into a droplet-like dense phase, inducing an instantaneous crystallization of solid Li_2S and suppressing the traditional step-by-step transformation. To verify the interaction between the electrode surfaces and Li_2S_6 molecules, we constructed MD models of S_6^{2-} and Li^+ ions with different concentrations over Mo NCs/N-G and Ti electrode surfaces (Fig. R39). The simulations revealed that Mo NCs/N-G gathered the S_6^{2-} and Li^+ ions from bulk solution to the electrode surface, which was independent of electrolyte concentration. Statistical analysis confirmed that Mo NCs/N-G exhibited stronger long-range attraction than Ti surface. Specifically, at the Mo NCs/N-G interface, the number of S atoms gradually increased over time (Fig. R40).

In addition, we used *ab initio* molecular dynamics (AIMD) simulations to investigate the charge transfer between Mo active centers and Li_2S_6 in the dense phase. We simulated the charge transfer and distribution in a model system containing Li_2S_6 molecules in the dense phase with the concentration of 17.9 wt% before and after applying an electrode potential. The electrode potential was provided by electron-donating Li atoms added below Mo NCs/N-G electrode. From the top view, we defined S_6 ions in the external, middle, and internal layers based on their distance from the Mo active centers (Fig. R41). At the moment when electrode potential was applied, the number of electrons in S_6 ions remained almost unchanged compared to its original state. However, after a relaxation period of 8 ps, S_6 ions undergo an obvious increase of electrons numbers and transfer. Specifically, compared with S_6 ions in the internal layer (3.78 – 3.34 = 0.44e), S_6 ions in the middle layer received even more electrons (2.42 – 1.73 = 0.69e), and S_6 ions in the external layer also gained some electrons (1.52 – 1.37 = 0.15e). AIMD results revealed that electrons can be transfer from Mo active centers to S_6 ions in the droplet-like dense phase from internal to external layers, not just the LiPSs molecules contact with active centers. Overall, our MD simulations showed that Mo active centers can induce a long-range gathering effect, while AIMD simulations demonstrated extremely fast electron transfer in these gathered LiPSs molecules. Therefore, Mo active centers can induce an instant reduction of LiPSs dense phase into solid Li_2S, which suppresses the step-by-step evolution of soluble LiPSs in the electrode without active centers.

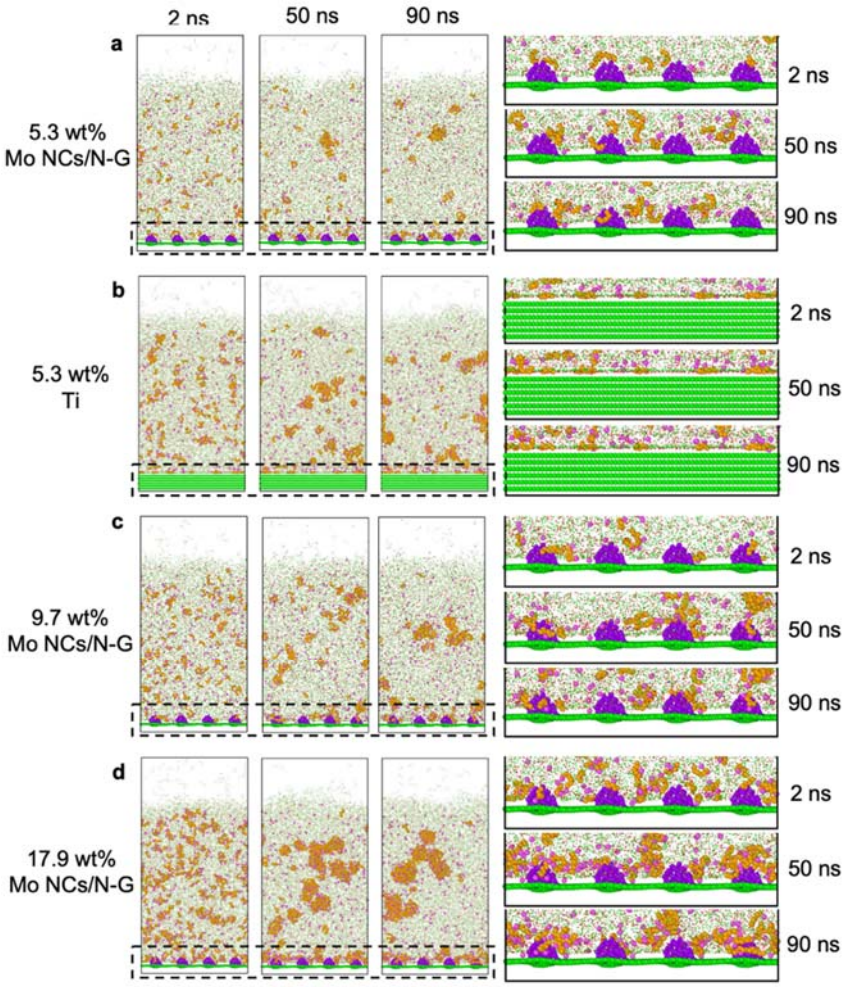

Fig. R39 | Time-series MD simulations of Li_2S_6 movement on the surface of Mo NCs/N-G and Ti. (a, b) Snapshots of MD simulations on different surfaces of Mo NCs/N-G and Ti with Li_2S_6 concentration 5.28 wt%. Snapshots of MD simulations on the surface of Mo NCs/N-G with different Li_2S_6 concentrations of (c) 9.68 wt% and (d) 17.93 wt%. The right row was the enlarged view of the interface details, and the initial S_6^{2-} and Li^+ ions were randomly dispersed in the electrolyte. After the NVT relaxation of 2 ns, the sampling results indicated that Mo NCs/N-G had a strong long-range attraction with S_6^{2-} and Li^+ ions.

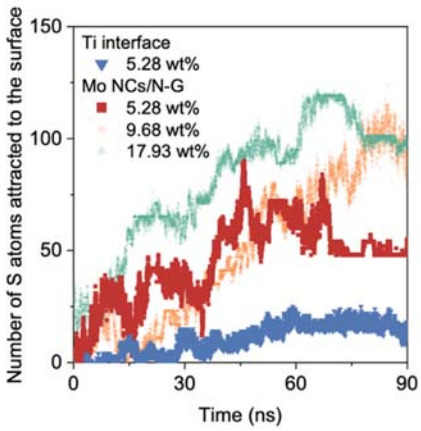

Fig. R40 | Statistical analysis of S atom variation. Statistics of S atoms attracted to the electrode surfaces of Mo NCs/N-G and Ti with different electrolyte concentration.

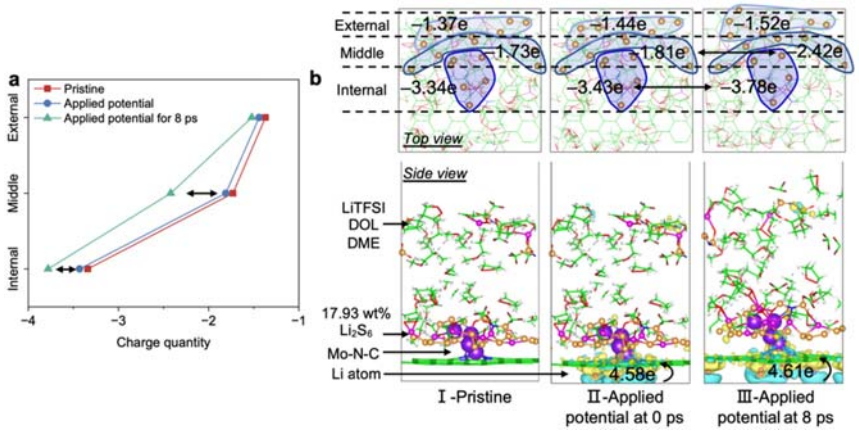

Fig. R41 | AIMD simulation of charge variation in S_6 ions. (a) Statistics of charge variation of S_6 ions in the internal, middle, and external layers. (b) AIMD simulation of charge variation of S_6 ions around Mo active centers from a top view and a side view. S_6 ions in the dense phase are divided into internal, middle, and external layers according to the distances from Mo active centers when viewed from the top. The charge distribution diagrams, shown from left to right, include (I) pristine structure relaxed for 20 ps before applying the electrode potential, simulations at (II) 0 ps and (III) 8 ps after applying the electrode potential. Considering the dynamic charge distribution, the ions in the dense phase were defined as S_6 ions.

Revision to Comment 8: The corresponding contents have been added in Extended Data Fig. 8 and Fig. S24-26. The discussions have been added in manuscript (page 9, line 25-30 and page 10, line 13-22) and Supplementary Discussions 5 (simulations of gathering and charge transfer in dense phase).

Comment 9: *In extended data Fig. 3, the authors simulated the crystal structure of tetragonal Li_2S_2 and hexagonal Li_2S_2 based on other materials such as Li_2O_2 and so on. However, they simulated hexagonal materials instead of Li_2S_2. This evidence is insufficient to establish that the structure of Li_2S_2 is tetragonal. Thus, the author should explain why they simulated hexagonal materials instead of hexagonal Li_2S_2.*

Response to Comment 9: There has been a long-standing debate over the crystal structure of metastable Li_2S_2. Initially, it was believed that Li_2S_2 had a hexagonal structure due to its similarity with Li_2O_2. However, we found that the simulated SAED pattern of hexagonal Li_2S_2 was inconsistent with our experimental results. To resolve this concern, we constructed and simulated the hexagonal Li_2S_2 based on the structures from the Materials Project for A_2B_2 compounds (A = Li, Na, K, Rb, B = O, S, Se) including Li_2O_2 (mp-841), Na_2O_2 (mp-2340), Na_2S_2 (mp-2400), Na_2Se_2 (mp-15668), K_2O_2 (mp-998917), K_2S_2 (mp-1287), and Rb_2S_2 (mp-9062), from the database version v2022.10.28. Upon further analysis, we found that the tetragonal structure of Li_2S_2 had a lower energy formation energy (E_f) than the hexagonal Li_2S_2 structures (Fig. R42). Additionally, the simulated and experimental SAED patterns were also consistent with the tetragonal Li_2S_2 structure along [001] and [111] directions (Extended data Fig. 2). Therefore, we concluded that Li_2S_2 was more likely to be a tetragonal structure. We feel sorry for the ambiguity in our previous description of Li_2S_2 structure simulation, and have updated the description accordingly in the revised version.

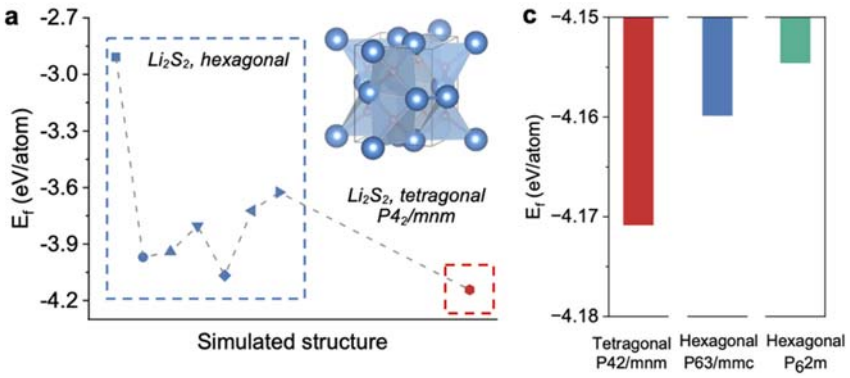

b

Simulated structures			Lattice parameters		
Li_2S_2 structures		Basic crystals	a (Å)	b (Å)	c (Å)
Tetragonal Li_2S_2	P42/mnm	Li_2S_2	5.07490	5.07490	6.11360
Hexagonal Li_2S_2	P63/mmc	Li_2O_2	3.18040	3.18040	7.70350
	$P\bar{6}2m$	Na_2O_2	6.27940	6.27940	4.50690
	P63/mmc	Na_2S_2	4.51430	4.5143	10.28410
	P63/mmc	Na_2Se_2	4.72570	4.7257	10.78840
	$P\bar{6}2m$	K_2O_2	7.14375	7.14375	5.12296
	$P\bar{6}2m$	K_2S_2	8.58610	8.58610	5.92090
	$P\bar{6}2m$	Rb_2S_2	8.96560	8.96560	6.19740

Fig. R42 | Energy comparison of Li_2S_2 with different crystal structures. (a) The energy comparison of tetragonal Li_2S_2 with different hexagonal Li_2S_2. Hexagonal Li_2S_2 candidates were simulated based on the hexagonal A_2B_2 structures (A = Li, Na, K, Rb, B = O, S, Se) with fixed lattice parameters. The inset is the crystal structure of tetragonal Li_2S_2 unit cell with the lowest E_f. The red and blue balls represent Li and S atoms, respectively. (b) The corresponding lattice parameters of tetragonal Li_2S_2 and hexagonal Li_2S_2, including hexagonal Li_2O_2, Na_2O_2, Na_2S_2, Na_2Se_2, K_2O_2, K_2S_2, and Rb_2S_2). (c) The energy comparison of tetragonal P42/mnm Li_2S_2 with different hexagonal Li_2S_2. Hexagonal Li_2S_2 candidates were simulated based on the P63/mmc and $P\bar{6}2m$ space groups with unfixed lattice parameters.

Revision to Comment 9: The corresponding contents have been added in Fig. 2c and Extended Data Fig. 2.

Reviewer #3:

General Comment: *In this work, the authors visualized the transformation of LiPSs over electrode interfaces at atomic scale by using in situ liquid-cell electrochemical transmission electron microscopy. They found the gathering-induced collective charge transfer of LiPSs on nanocluster active center immobilized surface and the induced instaneous deposition of nonequilibrium Li_2S nanocrystals from LiPSs dense liquid phase. It is a challenge work and found an interesting results. Therefore, I recommended it to be published after the following issues being addressed.*

Response to General Comment: We sincerely appreciate your recognition and general summary, which has motivated us to carefully revise the current version of our manuscript. We have seriously taken your valuable comments and suggestions into consideration and made the necessary revisions.

Comment 1: *Based on the authors' mentioned mechanism, the gathering of the LiPSs into droplet-like dense phase is important for the one step deposition. How to confirm the formation of the dense phase? Moreover, whether electric field or adsorption is the driving force for the gathering of LiPSs? Does the long chain LiPSs were not oxidized to short chain LiPSs during the gathering process under the electric field? More evidences are needed to address these issues.*

Response to Comment 1: Thank you for your valuable comments. To address your concerns more effectively, we would like to spilt your questions into three aspects. Please find our point-by-point responses below:

Characterization of droplet-like dense phase: In order to confirm the structure and composition of the droplet-like dense phase, we conducted the investigations using high-resolution S(TEM) images, SAED patterns, EDS mappings, and EELS. After a potentiostatic discharge at –0.5 V for 100 s, HRTEM images, along with their FFT and SAED patterns revealed the droplet-like dense phase and the crystallized structure of Li_2S nanoparticles (Fig. R43a, b). HAADF-STEM images, EDS mappings and linear elemental analysis confirmed a higher concentration of sulfur in both structures (Fig. R43c, d). EELS detected the characteristic S-$L_{2,3}$ edge peaks of droplet-like dense phase

at 173.5 eV and 180.7 eV, which were absent in the blank Li_2S_6 electrolyte, and were significantly stronger in the Li_2S nanocrystalline (Fig. R42e) [16,33,34]. The S-$L_{2,3}$ and S-L_1 edges peaks in the Li_2S nanocrystalline also showed a chemical redshift compared to the droplet-like dense phase, resulting from the electrochemical reduction and conversion from soluble S_n^{2-} ($2<n<6$) to solid S^{2-}.

In addition, we conducted a wider range observation in both bright field and dark field to investigate the structure of droplet-like dense phase. TEM and HAADF-STEM images showed that multiple droplet-like dense phases formed on the surface of Mo NCs/N-G nanosheets (Fig. R44). To solve the scattering and artifacts in HRTEM images resulting from amorphous SiN_x windows, disordered electrolyte, and the contrast transfer function of the electron microscope, a Gaussian filter was applied to suppress high-spatial frequency noise and enhance the boundary of dense phase areas. Both raw and post-processed HRTEM images confirmed the structure of nanoparticles inside dense phase areas (Fig. R45a, b). The contrast of the HAADF-STEM image, which is positively correlated with atomic number (Z), is determined by the elastically scattered electrons reaching the HAADF detector. In our analysis, we found that Li_2S nanocrystalline exhibited a higher contrast compared to droplet-like dense phase, as the former was the FCC close-packed structure of Li^+ and S^{2-} ions, while the later was the mixed structure of ions and solvent molecules. From the linear analysis of HAADF intensity, the contrast contribution can be attributed to Li_2S nanocrystalline, LiPSs dense phase, electrolyte, and the background, respectively (Fig. R45c-e). This was further confirmed in multiple areas and the linear HAADF intensity analysis. The results revealed that Li_2S nanocrystalline had a sharper and higher intensity, while LiPSs dense phase exhibited a more fluctuant and weaker intensity (Fig. R46). Therefore, based on the investigation of both chemical composition and image contrast, we can confirm that the droplet-like dense phase is the highly concentrated Li_2S_n ($2<n<6$).

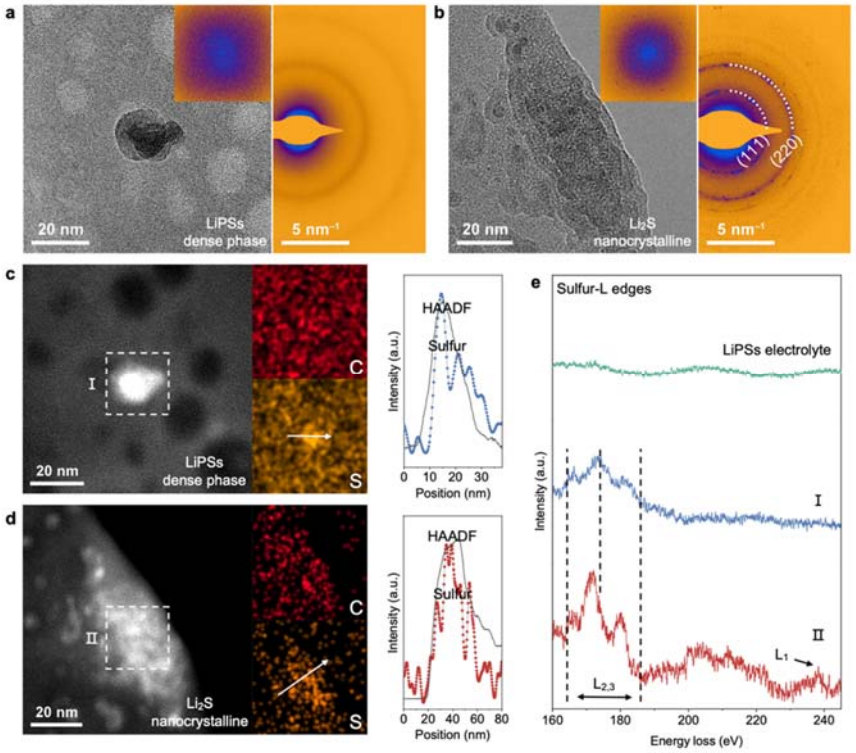

Fig. R43 | Characterization of LiPSs dense phase from structure and element. (a, b) TEM images, along with the corresponding FFT and SAED patterns of LiPSs droplet and Li_2S nanocrystalline. (c, d) STEM images, EDS mappings and the corresponding linear elemental analysis of LiPSs droplet and Li_2S nanocrystalline. (e) EELS of the sulfur L edges of blank LiPSs electrolyte, LiPSs droplet (area I in Fig. R12c), and Li_2S nanocrystalline (area II in Fig. R12d). The EELS were processed according to the following steps: zero-loss peak calibration, background removement (power law), and plural scattering removement (Fourier-ratio).

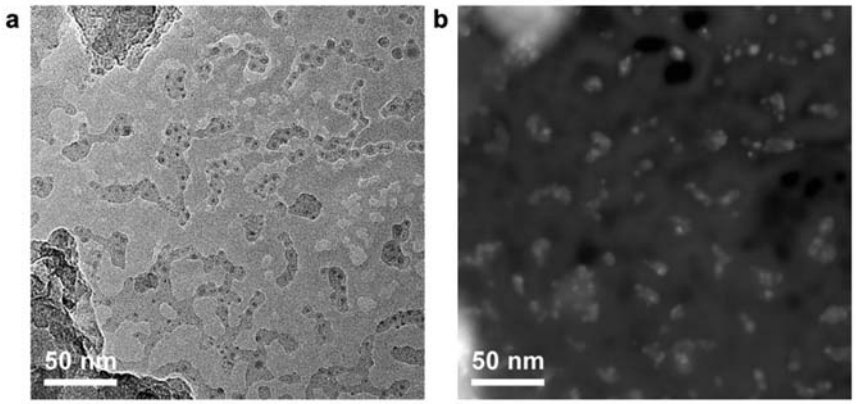

Fig. R44 | Observation of multiple LiPSs dense phases. (a, b) TEM and HAADF-STEM images of Mo NCs/N-G nanosheet after electrochemical deposition in electrochemical liquid cell, showing the LiPSs dense phase and Li_2S nanocrystalline.

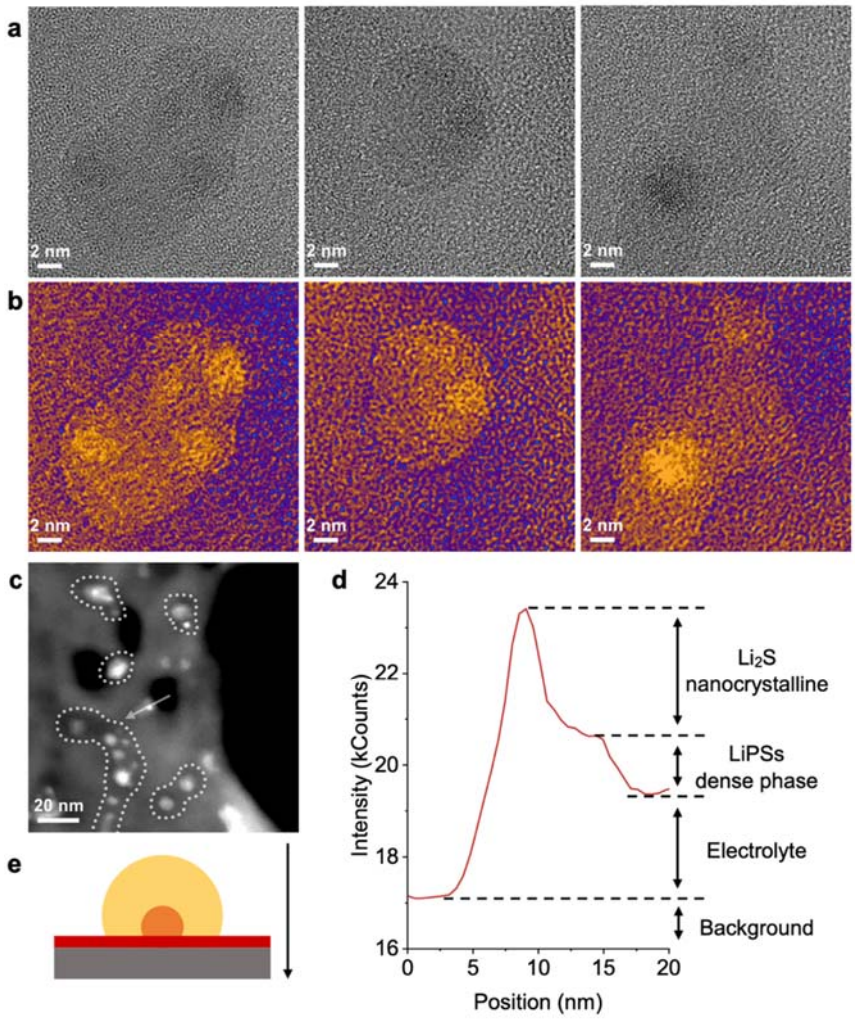

Fig. R45 | Characterization of LiPSs dense phase from HAADF intensity. (a, b) Raw and post-processed HRTEM images using a Gaussian filter. To solve the scattering and artifacts in HRTEM images resulting from amorphous SiN_x windows, disordered electrolyte, and the contrast transfer function of the electron microscope, a Gaussian filter was applied to suppress high-spatial frequency noise and enhance the boundary of dense phase areas. (c, d) Partial enlarged details of HAADF-STEM image and the corresponding linear HAADF intensity analysis. The areas of LiPSs dense phase were marked by the white dotted lines. The linear HAADF intensity analysis was marked by the white arrows. The particles with brighter contrast in the dense phase areas were Li_2S nanocrystalline. (e) Schematic illustration of the path of scattered electrons.

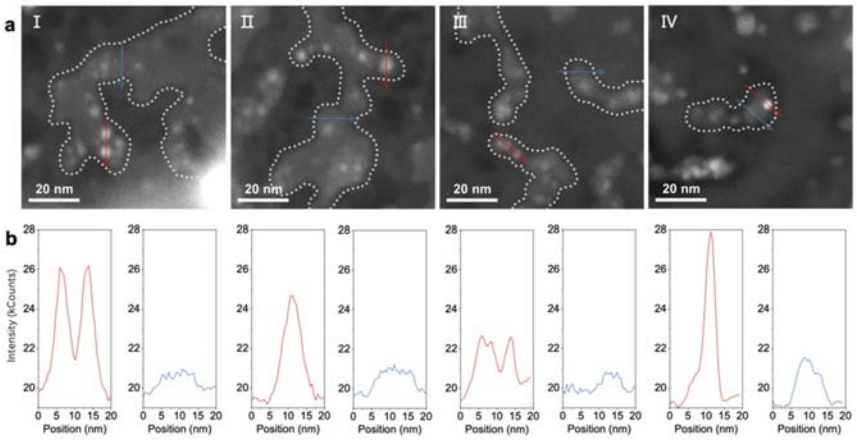

Fig. R46 | Confirmation of LiPSs dense phase from HAADF intensity. (a, b) Partial enlarged details of HAADF-STEM images and the corresponding linear HAADF intensity analysis. The areas of LiPSs dense phase were marked by the white dotted lines. The particles with brighter contrast in the dense phase areas were Li_2S nanocrystalline. The red and blue arrows/curves corresponded to Li_2S nanocrystalline and LiPSs dense phase, respectively.

The driving force for the gathering of LiPSs: To study the adsorption effects on various surfaces, we conducted UV-vis spectra using Li_2S_6 electrolyte and compared the results between Ti mesh and Mo NCs/N-G decorated Ti mesh (Fig. R47). After a 12-hour static adsorption, the electrolyte in the Mo NCs/N-G decorated Ti mesh appeared clearer and more transparent compared to the orange-red appearance of the Ti mesh and pure Li_2S_6 electrolyte. The UV-vis spectra showed a significant reduction in the absorption peak at ~420 nm, which signifies S_6^{2-} ions, in the Mo NCs/N-G decorated Ti mesh. This indicates that the strong adsorption effect on Li_2S_6 is largely due to the presence of Mo NCs/N-G nanosheets. To verify the interaction between the electrode surfaces and Li_2S_6 molecules, we constructed MD models of S_6^{2-} and Li^+ ions with different concentrations over Mo NCs/N-G and Ti electrode surfaces (Fig. R48). The simulations revealed that Mo NCs/N-G gathered the S_6^{2-} and Li^+ ions from bulk solution to the electrode surface, which was independent of electrolyte concentration. Statistical analysis confirmed that Mo NCs/N-G exhibited stronger long-range attraction than Ti surface. Specifically, at the Mo NCs/N-G interface, the number of S atoms gradually increased over time (Fig. R49).

Due to the fact that droplet-like dense phases were formed on the working electrode during potentiostatic discharge, the electric field should drive the diffusion of S_n^{2-} anions to the counter electrode under a negative potential of –0.5 V. The electric field performed an opposite effect with Mo NCs/N-G. Therefore, taking into account visible absorption experiments, MD simulations, and the intrinsic effect of the built-in electric field on the movement of S_n^{2-} anions, the aggregation of LiPSs should be attributed to the long-range interaction and adsorption of Mo NCs/N-G nanosheets.

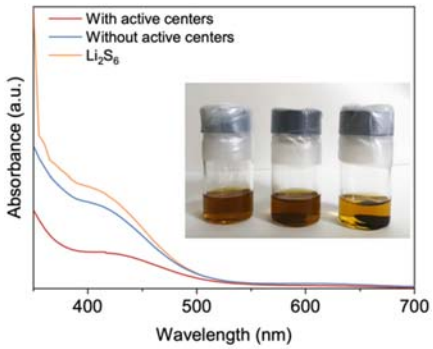

Fig. R47 | Static adsorption of LiPSs on Mo NCs/N-G nanosheets. UV-vis spectra and digital photograph after a 12-hour static Li_2S_6 adsorption of Ti mesh and Mo NCs/N-G decorated Ti mesh. 0.02 M Li_2S_6 was used the electrolyte. The Mo NCs/N-G areal loading was controlled at around 0.5 mg cm^{-2} (16 mm in diameter), prepared by ball milling the mixture of 80 wt% active materials and 20 wt% LA133 aqueous binder.

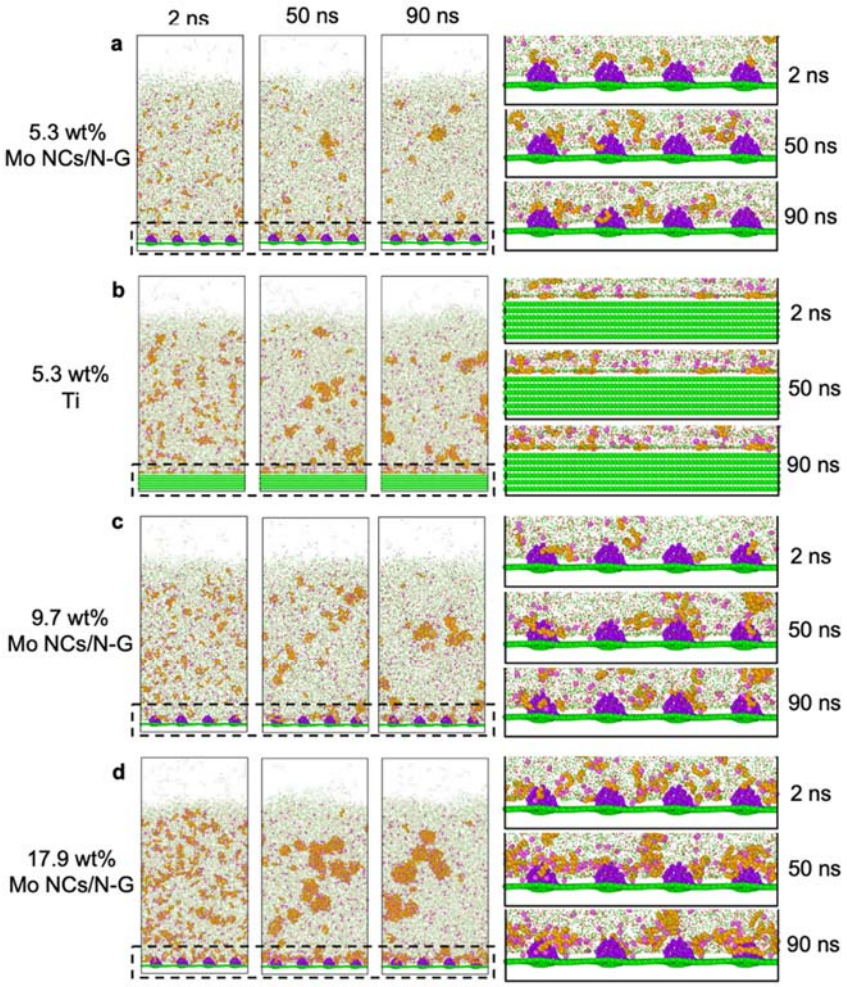

Fig. R48 | Time-series MD simulations of Li_2S_6 movement on the surface of Mo NCs/N-G and Ti. (a, b) Snapshots of MD simulations on different surfaces of Mo NCs/N-G and Ti with Li_2S_6 concentration 5.3 wt%. Snapshots of MD simulations on the surface of Mo NCs/N-G with different Li_2S_6 concentrations of (c) 9.7 wt% and (d) 17.9 wt%. The right row was the enlarged view of the interface details, and the initial S_6^{2-} and Li^+ ions were randomly dispersed in the electrolyte. After the NVT relaxation of 2 ns, the sampling results indicated that Mo NCs/N-G had a strong long-range attraction with S_6^{2-} and Li^+ ions.

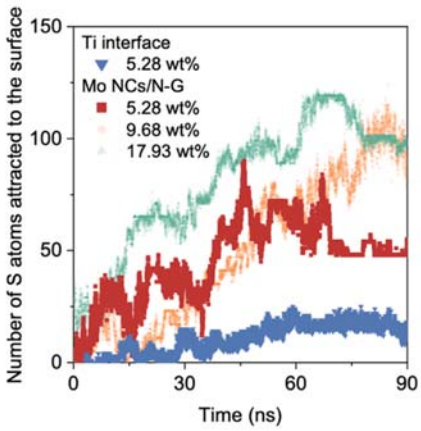

Fig. R49 | Statistical analysis of S atom variation. Statistics of S atoms attracted to the electrode surfaces of Mo NCs/N-G and Ti with different electrolyte concentration.

Conversion of LiPSs during the gathering process: In our *in situ* EC-TEM experiments, we observed that the reaction at the bare Ti electrode surface followed a step-by-step nucleation-growth process: (Step-I) the formation of Li_2S_2/Li_2S nuclei, and (Step-II) the continuous growth of Li_2S micro-rods. In contrast, at the Mo NCs/N-G nanosheet surface, we observed the gathering of LiPSs inducing direct Li_2S crystallization. No other soluble or insoluble intermediates were formed during this process, indicating that LiPSs reacted as a whole in the droplet-like dense phase, and transformed directly from the LiPSs dense phase into crystallized Li_2S. Since the conversion from soluble Li_2S_6 to Li_2S requires sustained electron transfer ($Li_2S_6 + 10Li^+ + 10e^- = 6Li_2S$), the gathered LiPSs should be continuously reduced under an electric field where electrons from the electrode interface were shared in the dense phase.

The *ab initio* molecular dynamics (AIMD) simulations were used to investigate the charge transfer between Mo active centers and Li_2S_6. The simulations involved a system containing Li_2S_6 molecules in the dense phase with the concentration of 17.9 wt% before and after applying an electrode potential. The potential was provided by electron-donating Li atoms added below the Mo NCs/N-G electrode. From the top view, S_6 ions were defined in the external, middle, and internal layers based on their distance from the Mo active centers (Fig. R50). At the moment when electrode potential was applied, the number of electrons transferred in S_6 ions almost remained unchanged

compared to its original state. However, after a relaxation period of 8 ps, S_6 ions received a significant increase in the number of electrons transferred from the electrodes. Specifically, S_6 ions in the middle layer received even more electrons (2.42 – 1.73 = 0.69e) than those in the internal layer (3.78 – 3.34 = 0.44e), while S_6 ions in the external layer also gained some electrons (1.52 – 1.37 = 0.15e). The AIMD results revealed that electrons can be transfer from Mo active centers to S_6 ions in the droplet-like dense phase from internal to external layers, not just the LiPSs molecules near the active centers. Therefore, both the experimental and simulation results demonstrate that during the gathering process, the gathered long-chain LiPSs in the dense phase are continuously reduced to short-chain LiPSs under an electric field, inducing a direct crystallization of solid Li_2S nanocrystalline.

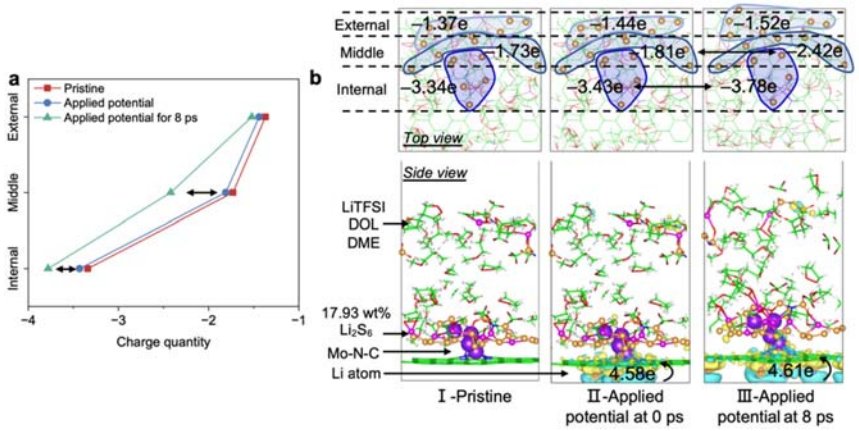

Fig. R50 | AIMD simulation of charge variation in S_6 ions. (a) Statistics of charge variation of S_6 ions in the internal, middle, and external layers. (b) AIMD simulation of charge variation of S_6 ions around Mo active centers from a top view and a side view. S_6 ions in the dense phase are divided into internal, middle, and external layers according to the distances from Mo active centers when viewed from the top. The charge distribution diagrams, shown from left to right, include (I) pristine structure relaxed for 20 ps before applying the electrode potential, simulations at (II) 0 ps and (III) 8 ps after applying the electrode potential. Considering the dynamic charge distribution, the ions in the dense phase were defined as S_6 ions.

Revision to Comment 1: The corresponding contents have been added in Fig. 4c, Extended Data Fig. 7, 8, and Fig. S22, 23, 26, 28. The discussions have been added in manuscript (page 8, line 25–page 9, line 8, page 9, line 25-30, and page 10, line 13-22).

and Supplementary Discussions 5 (simulations of gathering and charge transfer in dense phase).

Comment 2: *As we known, the LiPSs, Li_2S_2 and Li_2S are sensitive to the e-beam irradiation. What about the effect of e-beam on the HRTEM image and the electrochemical reaction during the in situ experiments.*

Response to Comment 2: Thank you for your concerns about the e-beam effect. Following your valuable comments, we investigated the effects of e-beams on the high-resolution structure of Li_2S, the decomposition of LiPSs electrolyte, and the electrochemical reactions, respectively.

E-beam effect on the high-resolution structure: Initially, we observed the structure of commercial Li_2S under a dose rate of 69 e $Å^{-2}$ s^{-1}. Time-series TEM images showed that it was susceptible to beam damage, which shrank and decomposed with the generation of nanobubble inside crystal in 8.6 s (Fig. R51). The e-beam damage in pure Li_2S should be mainly attributed to the ionization, radiolysis, and heating.[4,5] In contrast, by simply ultrasonically mixing commercial Li_2S with graphene, the e-beam effect can be largely alleviated, benefited from the good electrical and thermal conductivity of graphene. As a result, we were able to achieve atomic-resolution and long-time observation of Li_2S@graphene under a high dose rate of 11000 e $Å^{-2}$ s^{-1} (Fig. R52). This also explains how we were able to observe Li_2S nanocrystalline on Mo NCs/N-G nanosheet. In a repeated experiment, after an electrochemical deposition in a liquid cell, time-series HRTEM images revealed the atomic structure of Li_2S nanocrystalline on Mo NCs/N-G nanosheet along [100] direction (Fig. R53).

E-beam effect on electrolyte and solid Li_2S_2/Li_2S: We investigated the e-beam effect on LiPSs electrolyte and electrochemically deposited Li_2S_2/Li_2S in a liquid cell. Under a dose rate of 11.5 e $Å^{-2}$ s^{-1}, solid Li_2S_2/Li_2S underwent gradual decomposition over the course of 106.4 s (Fig. R54a), similar to the commercial Li_2S (Fig. R51). The accumulation of carbon contamination in the electrolyte resulted in a degradation of image resolution. By reducing the dose rate to 1.54 and 1.13 e $Å^{-2}$ s^{-1}, Li_2S remained

stable during the same observation time, and the carbon contamination was also greatly reduced (Figs. R54b, c). Meanwhile, the spatial resolution was maintained for real-time observation. Therefore, it is evident that a high e-beam dose rate can lead to the decomposition and carbon contamination of the electrolyte, which can be prevented by reducing the e-beam dose rate to below 1.5 e $Å^{-2}$ s^{-1}.

E-beam effect on electrochemical reactions: To examine the influence of e-beam on electrochemical reactions, we applied individual e-beams without an electric field. Time-series TEM images indicated that the e-beam alone could not induce heterogeneous deposition of Li_2S on SiN_x or Ti electrodes over 164 s (Fig. R55a). Besides, under a dose rate of 1.2 e $Å^{-2}$ s^{-1}, we quantified the impact of e-beam on electrochemical reactions, which accounted for 2.46% of the measured current density (Figs. R55b, c). During *in situ* EC-TEM experiments, Li_2S deposition occurred mainly at the electrode interface during potentiostatic discharge, indicating that electron accessibility is necessary for electrochemical reduction from soluble Li_2S_6 to solid Li_2S ($S_6^{2-} + e^- \rightarrow S^{2-}$) and can only be driven by an electric field, not an e-beam.

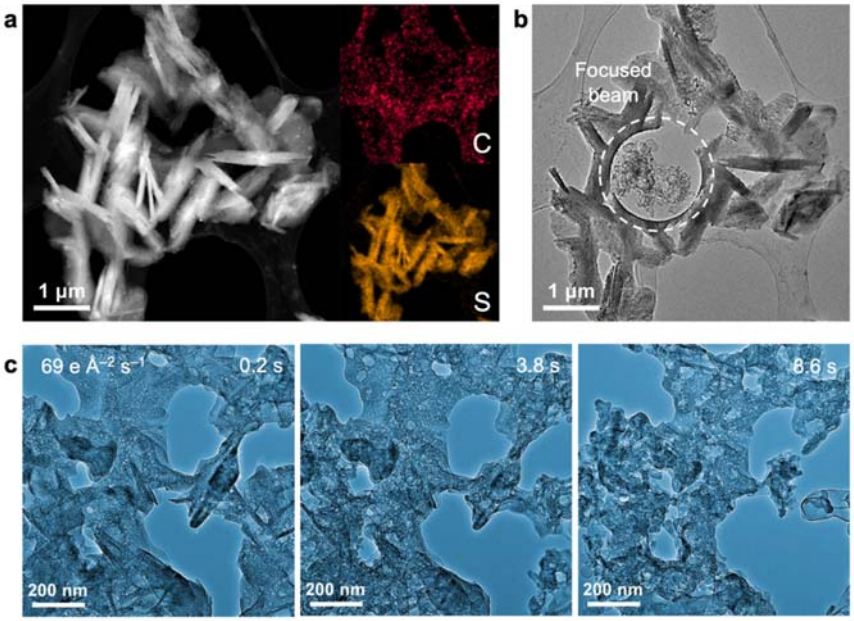

Fig. R51 | E-beam effect on commercial Li_2S. (a) STEM image and EDS mappings of the original commercial Li_2S. (b) TEM image of commercial Li_2S after focusing e-beam at the marked area. (c) Time-series TEM images of commercial Li_2S at a dose rate of 69 e $Å^{-2}$ s^{-1}, showing sever structure damage due to the focused e-beam.

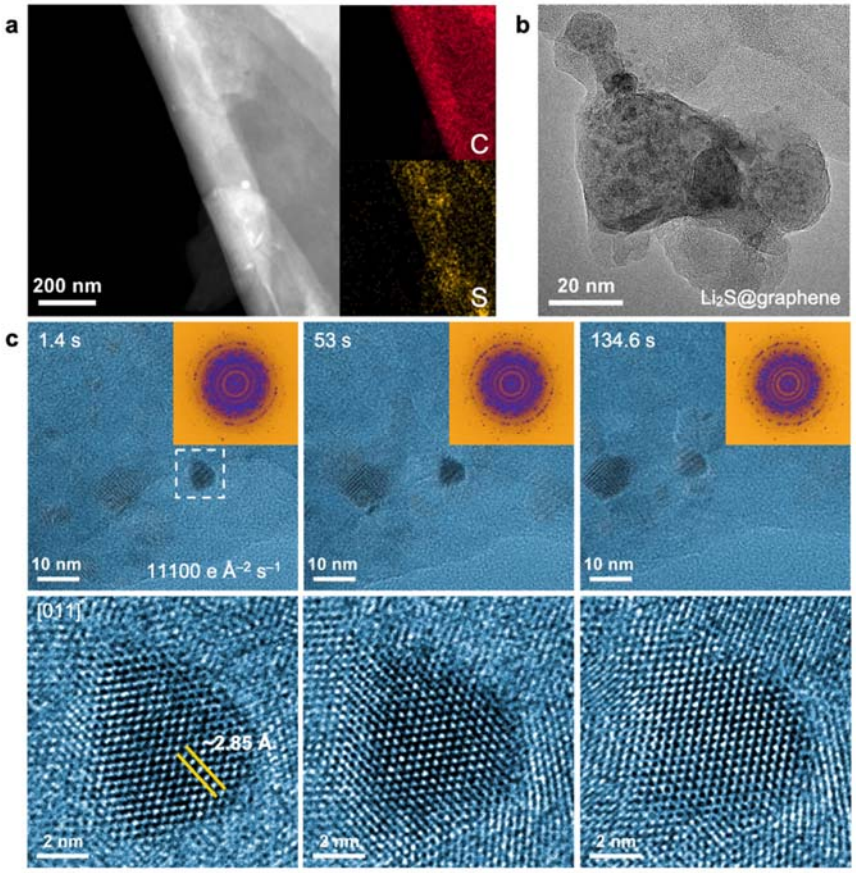

Fig. R52 | E-beam effect on Li_2S@graphene. (a, b) (S)TEM images and EDS mappings of Li_2S@graphene prepared by ultrasonically mixing commercial Li_2S with graphene in deionized water for 30 min. (c) Time-series HRTEM images, corresponding FFT patterns, and partial enlarged details of Li_2S@graphene at a dose rate of 11000 e $Å^{-2}$ s^{-1}, showing the alleviated electron damage and stable atomic structure of Li_2S nanocrystalline.

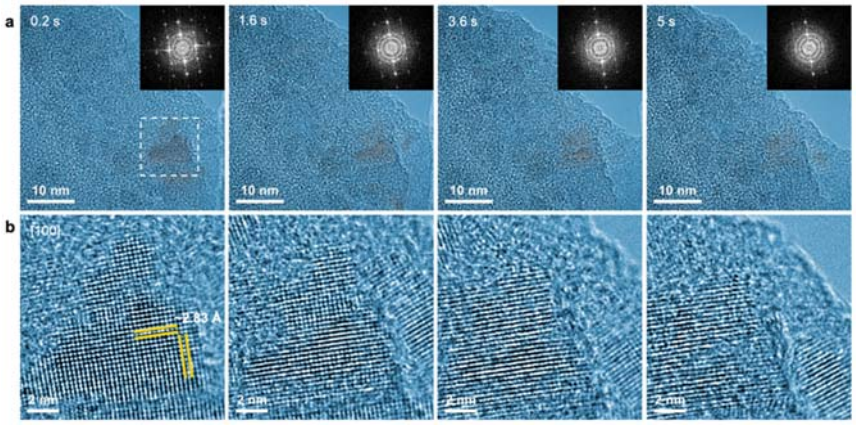

Fig. R53 | TEM images at different magnifications of Li_2S deposited on Mo NCs/N-G in a liquid cell. (a, b) Time-series HRTEM images, the corresponding FFT patterns,

and the partial enlarged details of Li_2S nanocrystalline deposited on Mo NCs/N-G obtained in electrochemical liquid cell.

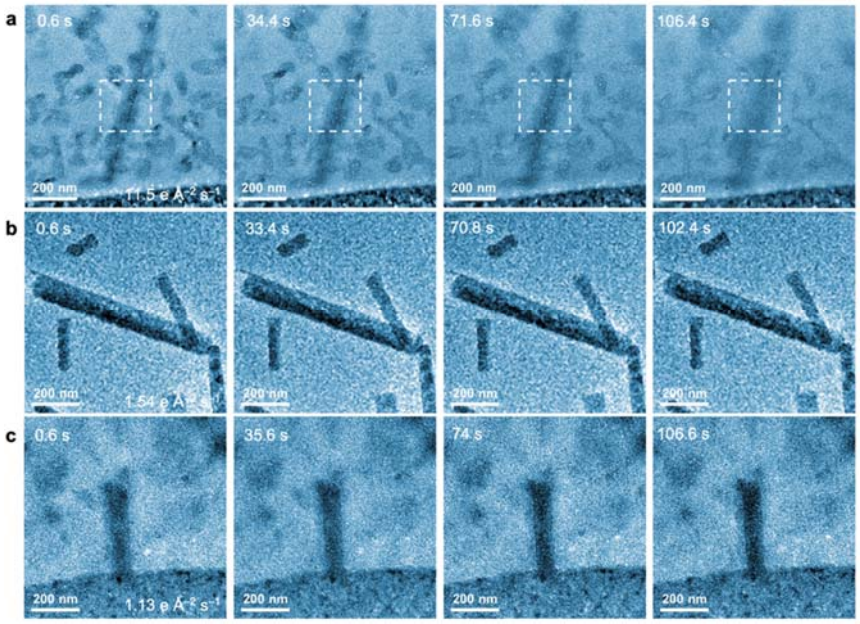

Fig. R54 | E-beam effect on the electrochemically deposited Li_2S micro-rods. (a-c) Time-series TEM images of Li_2S at the dose rates of 11.5, 1.54, and 1.13 e $Å^{-2}$ s^{-1}, respectively.

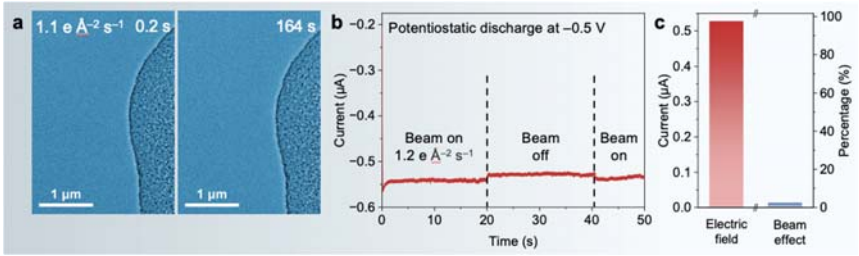

Fig. R55 | E-beam effect on the electrochemical deposition of Li_2S. (a) Exclusion of e-beam effect on heterogenous deposition of Li_2S. (b, c) Measured current during potentiostatic discharge at –0.5 V with e-beam on (1.2 e $Å^{-2}$ s^{-1})/off.

<u>Revision to Comment 2:</u> The corresponding contents have been added in Fig. S3-7. The discussions have been added in Supplementary Discussion 2 (e-beam effects).

Comment 3: *In Extended Data Fig. 2 (17 s) and Movie S2, discharge products were observed far from the electrode surface. It is an interesting phenomenon. The reasons and the electrochemical mechanisms are suggested to be further discussion.*

Response to Comment 3: Thank you for your comment on the formation and dissolution of small nanoparticles. The conversion from soluble Li_2S_6 to solid Li_2S_2/Li_2S occurred through the electrochemical reduction at the electrode interface ($S_6^{2-} + e^- \rightarrow S_2^{2-}/S^{2-}$). During this process, some of the reduced S_2^{2-}/S^{2-} ions diffused away from the electrode and caused the precipitation of granular Li_2S_n in the electrolyte ($S_n^{2-} + Li^+ \rightarrow Li_2S_n\downarrow$, $n\leq2$), as revealed in the TEM image at 17 s (Fig. R56). However, these solid discharge products were thermodynamically unstable and were prone to undergo disproportionation reactions or chemically react with soluble/long-chain LiPSs intermediates,[3] thus leading to their spontaneous decomposition and dissolution. As a result, the formation and dissolution of solid discharge products in the electrolyte was observed during the potentiostatic discharge. The similar dissolution process and inter-particle mass transfer was further confirmed by particles #1/#2 and particles #3/#4 in the supplemented deposition experiment (Fig. R57). Therefore, the investigation indicates that reduced S_n^{2-} ($n\leq2$) ions are diffusible and can result in the precipitation of solid Li_2S_n ($n\leq2$) near the electrode surface. The thermodynamic instability and chemical reactivity of these solid discharge products can lead to their spontaneous dissolution or decomposition, thereby supplying LiPSs species for the growth of larger particles.

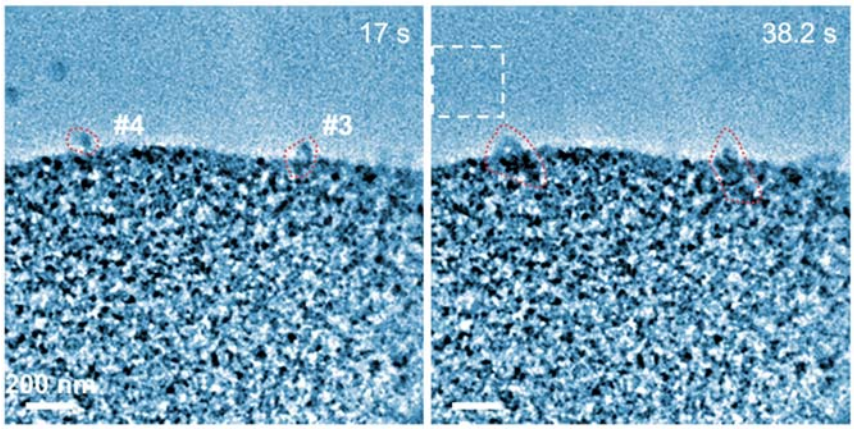

Fig. R56 | Li_2S deposition without mediation of active centers through a single-step pathway. Time-series TEM images from Supplementary Movie S2 of single-step deposition of Li_2S in an electrochemical liquid cell, showing the formation and dissolution of solid discharge products detached from electrode surface. The uncontacted distance of solid discharge products towards electrode surface was marked

by the double-sided arrows.

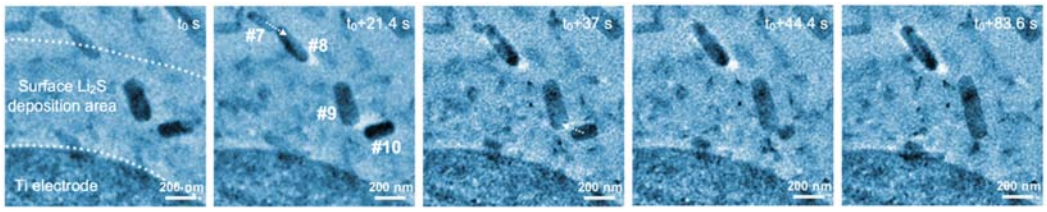

Fig. R57 | Surface Li_2S deposition on Ti electrode via two-step mechanism. Time-series TEM images showing two-step Li_2S deposition in liquid-cell EC-TEM. TEM image (t_0 s) revealed solid Li_2S deposited on the surface of Ti electrode. The mass transfer direction of inter-particle Ostwald ripening is indicated by the dotted single-sided arrows (t_0+21.4 s).

Revision to Comment 3: The corresponding contents have been added in Fig. S10.

Comment 4: *In situ or ex situ Raman spectra or XRD measurements are suggested to be performed to further confirm the gathering-induced collective charge transfer of LiPSs during the discharge/charge process of the batteries*

Response to Comment 4: Thank you for this important suggestion. The gathering-induced collective charge transfer of LiPSs primarily involved the gathering of soluble LiPSs and their fast conversion into solid Li_2S. To confirm this phenomenon, we conducted separate investigation on the soluble and insoluble discharge products through *ex situ* characterizations, including Raman spectra, XRD patterns, UV-vis spectra, SEM, and high-resolution (S)TEM.

Raman spectra: After galvanostatic discharge to 1.7 V, the coin-type cells were disassembled in an argon-filled glove-box. Subsequently, they were transferred to a stainless-steel device with a quartz window for Raman spectra characterization, which was crucial in preventing air pollution (Fig. R58a). The peaks at 473 and 458 cm^{-1} were primarily attributed to the S–S stretching vibration of the surface-adsorbed soluble Li_2S_n ($2<n<6$), while the peak at 374 cm^{-1} was associated with solid Li_2S[35-37]. The previous *in situ* and *ex situ* Raman studies have highlighted the challenge in identifying Li_2S peaks due to their low intensity. In our Raman spectra, both soluble and insoluble

discharge products exhibited significantly stronger signals when detected from the Mo NCs/N-G decorated surface, compared to the bare Ti electrode before/after deposition. This should be attributed to the Li_2S_n ($2<n<6$) dense phase and the abundant Li_2S nanocrystalline deposited on the Mo NCs/N-G nanosheet. Subsequently, the discharge products of solid Li_2S were investigated by XRD patterns and the soluble Li_2S_6 was investigated by UV-vis spectra. The structures of solid Li_2S deposited on different surfaces were further visualized by SEM and TEM images.

XRD patterns: Following the deposition of Li_2S in coin-type cells, the XRD patterns of Ti mesh with and without the decoration of Mo NCs/N-G nanosheet were analyzed, using a Kapton-filmed coin-type cell to avoid air exposure. Both patterns displayed characteristic diffraction peaks at approximately 26.4°, corresponding to the (111) crystal plane of cubic Li_2S (Fig. R58b). Notably, the Li_2S-Mo NCs/N-G pattern exhibited a stronger diffraction peak, indicating higher conversion activity from soluble Li_2S_6 to solid Li_2S. The size of the deposited Li_2S crystals was assessed using the Scherrer equation, $D = K\lambda/(\beta\cos\theta)$, where K is the Scherrer constant; λ is the X-ray wavelength; β is the full width at half maximum (FWHM); θ is the Bragg angle. As the crystalline size was inversely related to the β value, Li_2S-Mo NCs/N-G exhibited a smaller crystalline size compared to Li_2S-Ti.

UV-vis spectra: We conducted UV-vis spectra to investigate the adsorption effects of soluble Li_2S_6 on various surfaces, including Ti mesh and Mo NCs/N-G decorated Ti mesh (Fig. R47). After a static adsorption, the electrolyte in the Mo NCs/N-G decorated Ti mesh appeared clearer and more transparent, indicating a strong adsorption of soluble Li_2S_6. By measuring and linearly fitting the absorbance of blank Li_2S_6 electrolyte with varying concentrations, we were able to quantitatively calculate the Li_2S_6 adsorption capacity, showing 58.4 wt% of Mo NCs/N-G nanosheet and 13.4 wt% of bare Ti mesh (Fig. R58c, d).

SEM and TEM images: *Ex situ* SEM images indicated that the presence of Mo NCs/N-G resulted in a thicker and rougher surface after Li_2S deposition, primarily in a particle-like structure (Fig. R59a, b). In contrast, the bare Ti electrode exhibited a passivated layer covering the electrode surface, with sparse deposition of rod-like/plate-like Li_2S

due to its limited nucleation sites (Fig. R59c). The difference in surface morphology was further confirmed by *ex situ* (S)TEM images, EDS mappings, and SAED patterns. Li_2S was deposited on the surface of Mo NCs/N-G nanosheet as poly-crystalline nanoparticles, primarily exposing the (111), (200), and (220) crystal planes (Fig. R60a-c), while on the bare Ti electrode surface, it was deposited as single-crystal rod-like/plate-like structures (Fig. R60d-f). It is worth noting that while there may be variations in the size of Li_2S deposited in liquid cells and coin-type cells due to factors such as cell space, deposition time, and reactant amount, the reaction activity and deposition structure on different electrode surface remain highly consistent in both *in situ* and *ex situ* experiments.

Given that the same electrolyte was used in coin-type cells, the different deposition morphology and structure was attributed to the electrode surface with or without mediation of active centers. Mo NCs/N-G surface exhibited stronger adsorption, which induced the formation of soluble LiPSs dense phase (as evidenced by Raman spectra and UV-vis spectra). The fast electron transfer and reaction kinetics led to the deposition of Li_2S nanocrystalline (as evidenced by XRD, SEM, and TEM). Notably, even if the supplemented characterizations were highly consistent with the results obtained from *in situ* EC-TEM experiments, the details of gathering-induced collective charge transfer reaction, involving the gathering, conversion, and crystallization, could only be given by *in situ* EC-TEM due to its high spatial-temporal resolution. The irreplaceability of this method cannot be overemphasized.

Revision to Comment 4: The corresponding contents have been added in Fig. S28-30. The discussions have been added in Supplementary Discussion 6 (consistency of *in situ* and *ex situ* experiments).

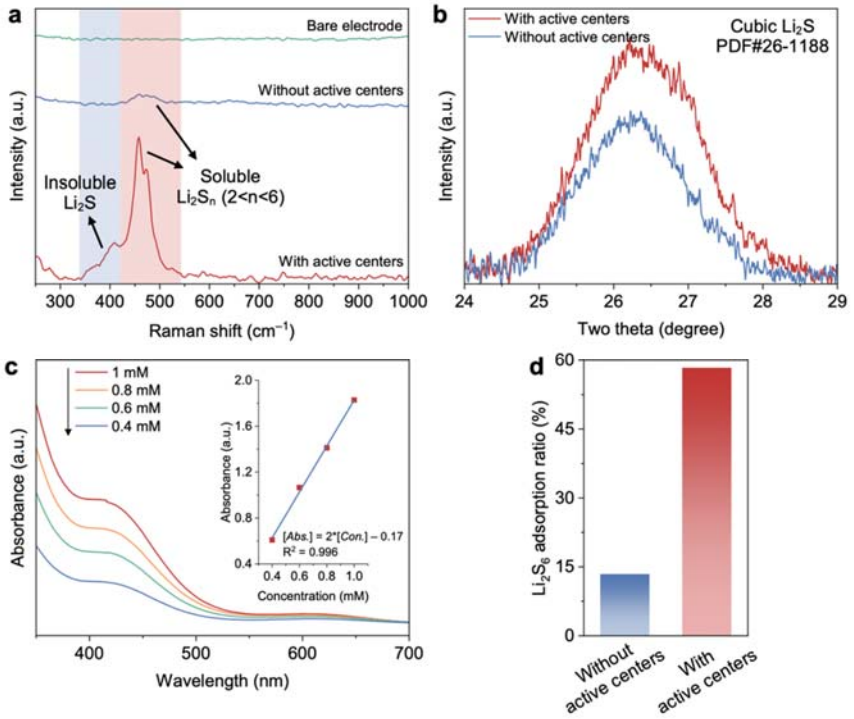

Fig. R58 | *Ex situ* Raman spectra, XRD patterns, and UV-vis spectra characterizations. (a) *Ex situ* Raman spectra of the fresh electrode of Mo NCs/N-G decorated Ti mesh, Ti mesh with/without the decoration of Mo NCs/N-G after galvanostatic discharge at 1.7 V in coin-type cells. To isolate the cycled electrodes from an air atmosphere, a specific stainless steel Raman device was engaged. A quartz window with a thickness of 0.5 mm was installed on the upper surface. (b) *Ex situ* XRD patterns of Ti mesh with/without the decoration of Mo NCs/N-G after galvanostatic discharge at 1.7 V in coin-type cells. To avoid air exposure, the deposited cells were dis-assembled in argon-filled glovebox and re-assembled into Kapton-filmed coin-type cells. (c) UV-vis spectra of blank Li_2S_6 electrolyte with different concentrations of 1, 0.8, 0.6, and 0.4 mM, as well as the corresponding linear fitting of absorbance and concentration. (d) The calculated Li_2S_6 adsorption ratio of Ti mesh with/without the decoration of Mo NCs/N-G based the absorbance and linear fitting.

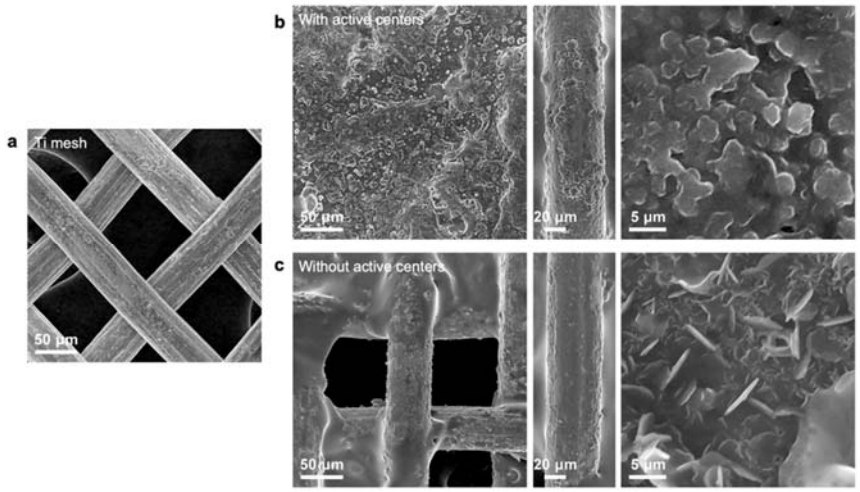

Fig. R59 | *Ex situ* SEM characterization. (a-c) *Ex situ* SEM characterizations of Ti mesh and Li_2S deposited Ti mesh with/without mediation of active centers after Li_2S deposition. Li_2S electrodeposition was conducted by galvanostatic discharge at 16 μA cm^{-2} with 100 mM Li_2S_6 electrolyte in coin-type cells from OCP to 1.7 V.

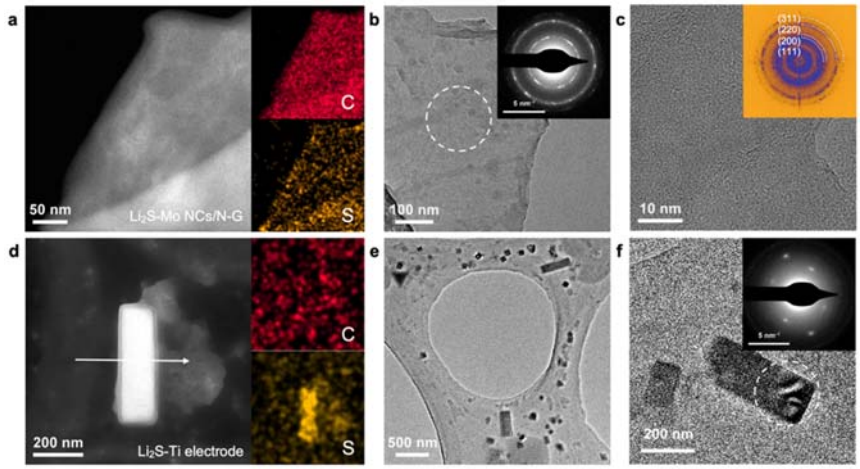

Fig. R60 | *Ex situ* (S)TEM characterization of deposited Li_2S with/without active centers. (a) *Ex situ* STEM and EDS mappings of Mo NCs/N-G nanosheet after Li_2S deposition in coin-type cells. (b, c) (HR)TEM images and the corresponding SAED and FFT patterns of Li_2S nanocrystalline deposited on Mo NCs/N-G nanosheet. Li_2S deposition was conducted by galvanostatic discharge at 16 μA cm^{-2} with 100 mM Li_2S_6 electrolyte in coin-type cells from OCP to 1.7 V. (d) *Ex situ* STEM images and EDS mappings of Li_2S micro-rod deposited on bare Ti electrode. (e, f) TEM images and the corresponding SAED pattern of Li_2S micro-rods. Li_2S deposition was conducted by the same galvanostatic discharge.

Reference

1. Shen, Z. *et al.* Cation-doped ZnS catalysts for polysulfide conversion in lithium–sulfur batteries. *Nat. Catal.* **5**, 555-563 (2022).
2. Chen, H. *et al.* Catalytic materials for lithium-sulfur batteries: mechanisms, design strategies and future perspective. *Mater. Today* **52**, 364-388 (2021).
3. Zhang, L. *et al.* Revealing the Electrochemical Charging Mechanism of Nanosized Li_2S by in Situ and Operando X-ray Absorption Spectroscopy. *Nano Lett.* **17**, 5084-5091 (2017).
4. Ye, H. *et al.* Activating Li_2S as the Lithium-Containing Cathode in Lithium–Sulfur Batteries. *ACS Energy Lett.* **5**, 2234-2245 (2020).
5. Zhang, Z. *et al.* Cryogenic Electron Microscopy for Energy Materials. *Acc. Chem. Res.* **54**, 3505-3517 (2021).
6. Liao, H.-G., Cui, L., Whitelam, S. & Zheng, H. Real-Time Imaging of Pt_3Fe Nanorod Growth in Solution. *Science* **336**, 1011-1014 (2012).
7. Peng, X. *et al.* Identification of a quasi-liquid phase at solid–liquid interface. *Nat. Comm.* **13** (2022).
8. Li, G. *et al.* Observations of Dense Liquid Phase-Assisted Nanocrystal Growth and Coalescence. *Cryst. Growth Des.* **21**, 6025-6030 (2021).
9. Woehl, T. J. *et al.* Experimental procedures to mitigate electron beam induced artifacts during in situ fluid imaging of nanomaterials. *Ultramicroscopy* **127**, 53-63 (2013).
10. de Jonge, N. & Ross, F. M. Electron microscopy of specimens in liquid. *Nat. Nanotechnol.* **6**, 695-704 (2011).
11. de Jonge, N., Houben, L., Dunin-Borkowski, R. E. & Ross, F. M. Resolution and aberration correction in liquid cell transmission electron microscopy. *Nat. Rev. Mater.* **4**, 61-78 (2018).
12. Gong, C. *et al.* Revealing the Role of Fluoride-Rich Battery Electrode Interphases by Operando Transmission Electron Microscopy. *Adv. Energy Mater.* **11** (2021).
13. Lee, S.-Y. *et al.* Unveiling the mechanisms of lithium dendrite suppression by cationic polymer film induced solid–electrolyte interphase modification. *Energy Environ. Sci.* **13**, 1832-1842 (2020).
14. Zhang, Q. *et al.* In situ TEM visualization of LiF nanosheet formation on the cathode-electrolyte interphase (CEI) in liquid-electrolyte lithium-ion batteries. *Matter* (2022).
15. Mehdi, B. L. *et al.* Observation and quantification of nanoscale processes in lithium batteries by operando electrochemical (S)TEM. *Nano Lett.* **15**, 2168-2173 (2015).
16. Xu, Z.-L. *et al.* Visualization of regulated nucleation and growth of lithium sulfides for high energy lithium sulfur batteries. *Energy Environ. Sci.* **12**, 3144-3155 (2019).
17. Hwa, Y., Seo, H. K., Yuk, J. M. & Cairns, E. J. Freeze-Dried Sulfur−Graphene Oxide−Carbon Nanotube Nanocomposite for High Sulfur-Loading Lithium/Sulfur Cells. *Nano Lett.* **17**, 7086-7094 (2017).
18. Levin, B. D. *et al.* Characterization of Sulfur and Nanostructured Sulfur Battery Cathodes in Electron Microscopy Without Sublimation Artifacts. *Microsc. Microanal.* **23**, 155-162 (2017).
19. Tan, G. *et al.* Burning lithium in CS_2 for high-performing compact Li_2S–graphene nanocapsules for Li–S batteries. *Nat. Energy* **2** (2017).
20. Zhang, J. *et al.* Lithiothermic-Synchronous Construction of Mo-Li_2S-Graphene Nanocomposites for High-Energy Li_2S//Si-C Battery. *Adv. Funct. Mater.* **32**, 2108305 (2022).
21. Zhang, J. *et al.* A Conductive Molecular Framework Derived Li2S/N,P-Codoped Carbon

Cathode for Advanced Lithium–Sulfur Batteries. *Adv. Energy Mater.* **7** (2017).
22. Serra-Maia, R. *et al.* Nanoscale Chemical and Structural Analysis during In Situ Scanning/Transmission Electron Microscopy in Liquids. *ACS Nano* **15**, 10228-10240 (2021).
23. Malis, T., Cheng, S. C. & Egerton, R. F. EELS log-ratio technique for specimen-thickness measurement in the TEM. *J. Electron. Microsc. Tech.* **8**, 193-200 (1988).
24. Ghosh, T., Bardhan, M., Bhattacharya, M. & Satpati, B. Study of inelastic mean free path of metal nanostructures using energy filtered transmission electron microscopy imaging. *J. Microsc.* **258**, 253-258 (2015).
25. LeBeau, J. M., Findlay, S. D., Allen, L. J. & Stemmer, S. Quantitative atomic resolution scanning transmission electron microscopy. *Phys. Rev. Lett.* **100**, 206101 (2008).
26. Ray Egerton & Cheng, S. Measurement of local thickness by electron energy-loss spectroscopy. *Ultramicroscopy* **21**, 231-244 (1987).
27. Li, Y. *et al.* Enhanced Chemical Immobilization and Catalytic Conversion of Polysulfide Intermediates Using Metallic Mo Nanoclusters for High-Performance Li-S Batteries. *ACS Nano* **14**, 1148-1157 (2020).
28. Liu, Y. *et al.* Monodisperse Molybdenum Nanoparticles as Highly Efficient Electrocatalysts for Li-S Batteries. *ACS Nano* **15**, 15047-15056 (2021).
29. Han, L. *et al.* Atomically Dispersed Molybdenum Catalysts for Efficient Ambient Nitrogen Fixation. *Angew. Chem. Int. Ed.* **58**, 2321-2325 (2019).
30. Liu, X.-C. *et al.* Utilizing a metal as a sulfur host for high performance Li-S batteries. *Nano Energy* **50**, 685-690 (2018).
31. Baran, M. in *EUROCON 2005 - The International Conference on "Computer as a Tool".* 975-978.
32. Ishizuka, K., Eilers, P. H. C. & Kogure, T. Optimal Noise Filters in High-Resolution Electron Microscopy. *Microsc. Microanal.* **13**, 902-903 (2007).
33. Zhao, J. *et al.* Size-Dependent Chemomechanical Failure of Sulfide Solid Electrolyte Particles during Electrochemical Reaction with Lithium. *Nano Lett.* **22**, 411-418 (2022).
34. Wang, Z. *et al.* In Situ TEM Observations of Discharging/Charging of Solid-State Lithium-Sulfur Batteries at High Temperatures. *Small* **16**, 2001899 (2020).
35. Yao, H. *et al.* Improved lithium–sulfur batteries with a conductive coating on the separator to prevent the accumulation of inactive S-related species at the cathode–separator interface. *Energy Environ. Sci.* **7**, 3381-3390 (2014).
36. Blanchard, D. & Slagter, M. In operando Raman and optical study of lithium polysulfides dissolution in lithium–sulfur cells with carrageenan binder. *J. Phys.-Energy* **3** (2021).
37. Partovi-Azar, P., Kuhne, T. D. & Kaghazchi, P. Evidence for the existence of Li2S2 clusters in lithium-sulfur batteries: ab initio Raman spectroscopy simulation. *Phys. Chem. Chem. Phys.* **17**, 22009-22014 (2015).

Reviewer Reports on the First Revision:

Referees' comments:

Referee #1 (Remarks to the Author):

I carefully read the authors' responses and revised manuscript.
The concerns about the mechanism of Li2S6 crystallization, electron beam induced effect, and MD simulations of Li2S6 have been well addressed. I recommend the acceptance of this manuscript without any change.

Referee #2 (Remarks to the Author):

In the revised manuscript and response letter, the authors conducted additional experiments in response to the reviewer's comments. These new results are valuable contributions to the research field of Li-S batteries and TEM studies. I appreciate the authors' time and effort in providing logical and thorough responses to our questions. While I acknowledge the significance and advances of this work, I still have some concerns that need to be addressed.
1. The author used 10 nm SiNx windows in their in situ TEM analysis, which is a progressive work in Li-S batteries and in situ experiments. However, the authors still mentioned the thickness of SiNx windows and 100 nm spacer. Although the authors planned to make a 100 nm thickness spacer, the thickness of the EC cell could be swollen by a bulging out effect. This effect is very well-known in the field of in situ liquid TEM society. Please measure the thinkness of the part that contains two SiNx layers (20 nm) and swollen liquid layer (more than 100 nm). If this chip did not have the bulging effect, the authors should very carefully mention it as well.
2. In order to obtain high quality images, the author operated in situ TEM with an e-beam at a dose rate of 1.2 e Å–2 s–1 and 100 nm spacer for holding the electrolyte. The low dose rate of 1.2 Å–2 s–1 may not be sufficient to obtain high-quality HRTEM images. Thus, this reviewer suggests that the authors compare the in situ TEM and HRTEM images with a dose rate of 1.2 Å–2 s–1.
3. In addition, if the spacer thickness is an important factor in in situ TEM with low dose rates, please provide TEM images with spaces of different thickness (e.g 200, 500, 1000 nm etc.).
4. In Fig. R14, it is difficult to understand the SEM image of Ti mesh with active centers. Based on Fig. R22, the Ti mesh appears to be covered with active centers. Then, please clarify how to capture images of the middle of Fig. R14 C, which shows a warped Ti mesh. Additionally, please provide SEM images of the Ti mesh with active centers before the reactions.
5. The authors showed two types of bubbles which are nanobubbles in Fig. R17 and 19 and e-beam bubbles in Fig. R20. It is unclear what distinguishes these two types of bubbles. Thus, please explain this difference in detail.
6. In Comment 3, (2) Impact of electrolyte concentration on nucleation-growth pathways section, the authors provided only the effect of different potential, not electrolyte concentration. Thus, the authors should investigate the impact of electrolyte concentration and explain its effect clearly.
7. In the Discussion of the depletion area section, it is unclear to understand the meaning of the content. The authors mentioned that "appearance of depletion layers is random at micro-/nano-scales, and there can be inconsistency in local observation area." If the appearance of the depletion

layer is indeed random, then it cannot be explained. Thus, please explain the concept of depletion area more clearly or remove the section from the manuscript if the authors cannot adequately explain it.

Referee #3 (Remarks to the Author):

After being revised, the manuscript has been improved and suitable for the publication. Therefore, I recommend it to be published as it is.

Author Rebuttals to First Revision:

Nature (Manuscript ID: 2022-10-16085A)

Visualizing Interfacial Collective Reaction Behaviour of Li-S Batteries

Authors: Shiyuan Zhou,† Jie Shi,† Sangui Liu, Gen Li, Fei Pei, Youhu Chen, Junxian Deng, Qizheng Zheng, Jiayi Li, Chen Zhao, Inhui Hwang, Cheng-Jun Sun, Yuzi Liu, Yu Deng, Ling Huang, Yu Qiao, Gui-Liang Xu,* Jian-Feng Chen, Khalil Amine,* Shi-Gang Sun and Hong-Gang Liao*

We would like to express our sincere gratitude to the editor and all the three referees for the valuable feedback/suggestions on our work.

In this section, we provide a detailed point-by-point response to each comment of referee #2. To distinguish the comments from our responses, we have presented the comments in *italics*. Additionally, any revisions from referee's comment to our manuscript or supporting information are highlighted in red for clarity. The revisions from editorial suggestions to our manuscript are highlighted in blue.

Besides, to facilitate the distinction of figures in different files, we have marked them as follows: **Figs. R1-6** are the figures in response; **Figs. 1-4** are the figures in main text; **Extended Data Figs. 1-10** are the figures in extended data; **Supplementary Figs. 1-36** are the figures in supporting information.

Thank you once again to the editor and referees for their valuable comments.

Responses to Referees:

A Detailed Point-by-Point Responses to Referees' Comments

Referee #1:

General Comment: *I carefully read the authors' responses and revised manuscript. The concerns about the mechanism of Li_2S_6 crystallization, electron beam induced effect, and MD simulations of Li_2S_6 have been well addressed. I recommend the acceptance of this manuscript without any change.*

Response to General Comment: We are very grateful to the referee for carefully reading our response. Thank you very much for your approval of our revised manuscript.

Referee #2:

General Comment: *In the revised manuscript and response letter, the authors conducted additional experiments in response to the reviewer's comments. These new results are valuable contributions to the research field of Li-S batteries and TEM studies. I appreciate the authors' time and effort in providing logical and thorough responses to our questions. While I acknowledge the significance and advances of this work, I still have some concerns that need to be addressed.*

Response to General Comment: We sincerely appreciate your further valuable feedback. Your insightful comments, such as bulging effect, spacer thickness, influence of concentration on deposition, etc., definitely enhance the quality of this research. We have attached a point-by-point response to your questions.

Comment 1: *The author used 10 nm SiN_x windows in their in situ TEM analysis, which is a progressive work in Li-S batteries and in situ experiments. However, the authors still mentioned the thickness of SiN_x windows and 100 nm spacer. Although the authors planned to make a 100 nm thickness spacer, the thickness of the EC cell could be swollen by a bulging out effect. This effect is very well-known in the field of in situ liquid TEM society. Please measure the thinkness of the part that contains two SiN_x layers (20 nm) and swollen liquid layer (more than 100 nm). If this chip did not have the bulging effect, the authors should very carefully mention it as well.*

Response to Comment 1: The bulging of the SiN_x windows is a common issue that arises from the geometry of the window, particularly the large length and width sizes, as well as the pressure difference between the liquid cell and the high-vacuum chamber of the electron microscope. This issue is usually observed in commercial flow holder systems and can lead to a considerable increase in the liquid layer thickness and a decrease in the resolution due to beam broadening and chromatic aberrations[1].

To address this issue, our liquid cell has a reduced window width of 5-8 μm and a length of 50 μm. The reduced window width alleviates the bulging effect. Additionally, the volume of the closed cell is in the range of hundreds of picolitres, which is significantly smaller than that of a flow system. This means that even slight bulging can lead to a

considerable decrease in pressure inside the liquid cell, thereby compensating the pressure difference between the inside and outside. As a result, the bulging effect of the SiN_x observation windows in our liquid cells has been largely reduced. These findings have been verified by high-resolution *in situ* TEM images throughout the manuscript and our previously reported works[2-4].

We have quantitatively measured the thickness of the liquid layer in our electrochemical liquid cell with EELS and the log-ratio method $t/\lambda = \ln(I_t/I_0)$[5-8]. In this equation, t represents the absolute thickness of the liquid layer, λ is the mean free path, I_t is the integration of the entire EELS, and I_0 is the integration of the zero-loss peak. Here, we sealed deionized water in liquid cells to measure the thickness, where the mean free path (λ_{water}) is 330 nm at an acceleration voltage of 300 kV[9]. In addition to the high-resolution TEM image and the clear Ti electrode (Fig. R1a), EELS revealed similar values of liquid layer thickness across different areas in the liquid cell, providing further evidence of the alleviated bulging effect. The thickness of the liquid layer can be obtained using the following equation (Fig. R1b, c), once the relative thickness of the two SiN_x observation windows has been measured (Extended Data Fig. 5h):

$$t_{water}/\lambda_{water} + 2\times t_{SiNx}/\lambda_{SiNx} = \ln(I_t/I_0) \quad (2)$$

The thickness of the liquid layer was determined to be approximately 124.74±8.54 nm.

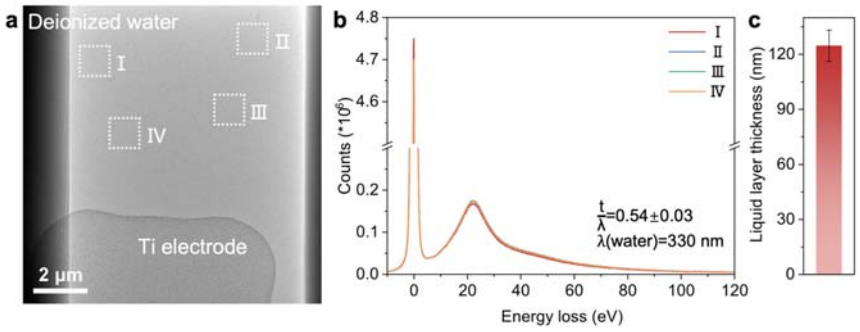

Fig. R1 | Measurement of liquid layer thickness through EELS. (a) TEM image of an electrochemical liquid cell filled with deionized water. (b) Typical low-loss EELS of a liquid specimen sandwiched between two SiN_x membranes corresponding to the areas marked in Fig. R1a. Relative thickness ($t_{water}/\lambda_{water}$) is obtained by the log-ratio method in Digital Micrograph software. (c) Average thickness of liquid layer. Error bars represent standard deviations from multiple EELS curves (I-IV).

Revision to Comment 1: The corresponding contents have been added in Supplementary Discussions (1.2 Bulging effect) and Supplementary Fig. 3.

Reference

1. Woehl, T. J. *et al.* Experimental procedures to mitigate electron beam induced artifacts during in situ fluid imaging of nanomaterials. *Ultramicroscopy* **127**, 53-63 (2013).
2. Xiao, L. *et al.* Efficient CO_2 reduction MOFs derivatives transformation mechanism revealed by in-situ liquid phase TEM. *Appl. Catal. B: Environ.* **307**, 121164 (2022).
3. Li, G. *et al.* Observations of Dense Liquid Phase-Assisted Nanocrystal Growth and Coalescence. *Cryst. Growth Des.* **21**, 6025-6030 (2021).
4. Peng, X. *et al.* Identification of a quasi-liquid phase at solid–liquid interface. *Nat. Comm.* **13** (2022).
5. Malis, T., Cheng, S. C. & Egerton, R. F. EELS log-ratio technique for specimen-thickness measurement in the TEM. *J. Electron. Microsc. Tech.* **8**, 193-200 (1988).
6. Ghosh, T., Bardhan, M., Bhattacharya, M. & Satpati, B. Study of inelastic mean free path of metal nanostructures using energy filtered transmission electron microscopy imaging. *J. Microsc.* **258**, 253-258 (2015).
7. LeBeau, J. M., Findlay, S. D., Allen, L. J. & Stemmer, S. Quantitative atomic resolution scanning transmission electron microscopy. *Phys. Rev. Lett.* **100**, 206101 (2008).
8. Ray Egerton & Cheng, S. Measurement of local thickness by electron energy-loss spectroscopy. *Ultramicroscopy* **21**, 231-244 (1987).
9. Yesibolati, M. N. *et al.* Electron inelastic mean free path in water. *Nanoscale* **12**, 20649-20657 (2020).

Comment 2: *In order to obtain high quality images, the author operated in situ TEM with an e-beam at a dose rate of 1.2 e Å^{-2} s^{-1} and 100 nm spacer for holding the electrolyte. The low dose rate of 1.2 e Å^{-2} s^{-1} may not be sufficient to obtain high-quality HRTEM images. Thus, this reviewer suggests that the authors compare the in situ TEM and HRTEM images with a dose rate of 1.2 e Å^{-2} s^{-1}.*

Response to Comment 2: In order to avoid the e-beam effect, real-time observations were conducted at a magnification of approximately SA 4000 × and dose rate of around 1.2 e Å^{-2} s^{-1}, which was obviously insufficient for acquiring HRTEM images. For obtaining HRTEM image, a magnification of around SA 630,000 × and a spot size of 2 are used. At this setting, the lowest dose rate that can be set by the electron microscope is approximately 50 e Å^{-2} s^{-1}. After considering valuable suggestions, we conducted further HRTEM investigations at various e-beam dose rates (Fig. R2).

HRTEM images and the corresponding FFT patterns of Li_2S-Mo NCs/N-G were obtained after the electrochemical deposition in a liquid cell. At a dose rate of 51 e $Å^{-2}$ s^{-1}, using a resolution of 4096*4096 and 500 ms exposure time, the surface structures could not be observed. Even after extending the exposure time to 10 s, the sample drifting impeded high-resolution observation, although the outline of graphene was observable. However, by increasing the dose rate to approximately 200 e $Å^{-2}$ s^{-1}, the crystal structure of Li_2S nanocrystalline become visible, as confirmed by the FFT patterns. With a further increase in the e-beam dose rate, the atomic structures became clearer. Therefore, it is crucial to note that achieving high-quality HRTEM images of Li_2S nanocrystalline requires a balance of the e-beam dose rate, exposure time, and image resolution.

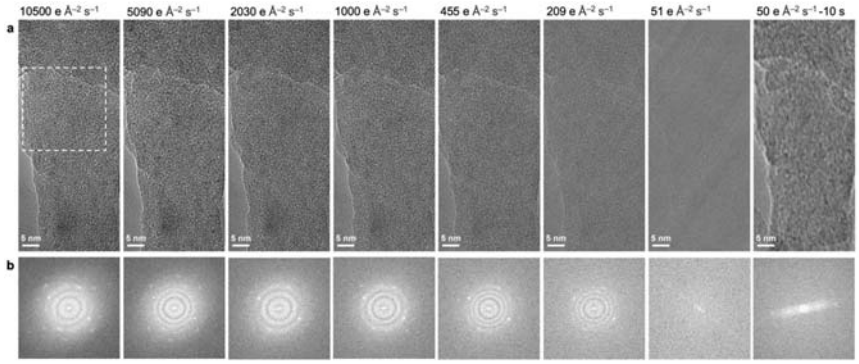

Fig. R2 | Structures of Li_2S-Mo NCs/N-G obtained at various e-beam dose rates. (a, b) HRTEM images and the corresponding FFT patterns of Li_2S-Mo NCs/N-G after electrochemical deposition in a liquid cell. The HRTEM images were acquired by FEI Talos-F200s TEM operating at 200 kV, using Velox software at various e-beam dose rates, with a resolution of 4096×4096 pixels and an exposure time of 500 ms (from the first to the seventh columns) and 10 s (the eighth column).

Revision to Comment 2: The corresponding contents have been added in Supplementary Fig. 21.

Comment 3: *In addition, if the spacer thickness is an important factor in in situ TEM with low dose rates, please provide TEM images with spaces of different thickness (e.g 200, 500, 1000 nm etc.).*

Response to Comment 3: Thank you for providing your valuable suggestion. We have supplemented TEM images of electrochemical liquid cells sealed with spacers of varying thicknesses, ranging from 100 to 1000 nm. In the TEM images taken with spacers of 100 and 200 nm (Fig. R3a, b), the edges of the Ti electrode were clearly visible. However, as the spacer thickness increased to 500 nm (Fig. R3c), the electrode could not be imaged clearly due to the increased thickness of the electrolyte layer. When the spacer thickness was increased to 1000 nm (Fig. R3d), SiN_x observation windows can hardly be located. These results from the TEM images clearly demonstrate the critical importance of using thinner spacers to obtain high-resolution TEM images.

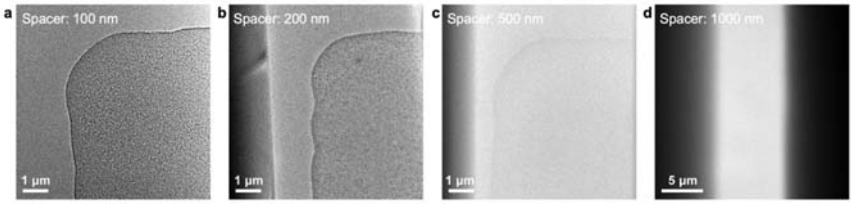

Fig. R3 | Influence of liquid cell spacers thickness. TEM images of electrochemical liquid cells with varying spacer thickness, including 100, 200, 500, and 1000 nm.

Revision to Comment 3: The corresponding contents have been added in Supplementary Discussions (1.1 Spacer thickness) and Supplementary Fig. 2.

Comment 4: *In Fig. R14, it is difficult to understand the SEM image of Ti mesh with active centers. Based on Fig. R22, the Ti mesh appears to be covered with active centers. Then, please clarify how to capture images of the middle of Fig. R14 C, which shows a warped Ti mesh. Additionally, please provide SEM images of the Ti mesh with active centers before the reactions.*

Response to Comment 4: We feel sorry for any confusion in our previous description. In our study, we utilized both Ti meshes with and without active centers for *ex situ* investigations in coin-type cells, as illustrated in Supplementary Fig. 33 (formerly Fig. R14). Additionally, Ti electrodes in liquid cells with or without active centers were used in *in situ* TEM experiments, as shown in Extended Data Fig. 5 (formerly Fig. R22). It is important to note that the SEM image in the middle of Fig. R14c (from the previous

revision) was taken after the electrochemical deposition of Li_2S in coin-type cells.

To provide further clarity, we have included additional SEM images of the Ti mesh with and without active centers before the electrochemical deposition of Li_2S in coin-type cells. After the introduction of active centers, SEM images clearly showed the coverage of Mo NCs/N-G nanosheets on the surface of Ti mesh (Fig. R4).

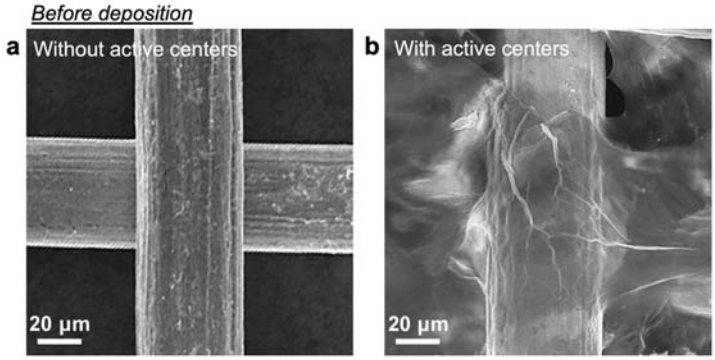

Fig. R4 | *Ex situ* SEM characterization of Ti mesh with/without active centers before deposition. (a) SEM images of pristine Ti mesh without active centers. (b) SEM images of Ti mesh with active centers. Slurry was prepared by ball milling the mixture of 80 wt% Mo NCs/N-G and 20 wt% LA133 aqueous binder, which was then coated on Ti mesh disks.

Revision to Comment 4: The corresponding contents have been added in Supplementary Fig. 33.

Comment 5: *The authors showed two types of bubbles which are nanobubbles in Fig. R17 and 19 and e-beam bubbles in Fig. R20. It is unclear what distinguishes these two types of bubbles. Thus, please explain this difference in detail.*

Response to Comment 5: Thank you for raising this issue. As highlighted by the referee, to prevent any confusion, we have replaced the term "nanobubbles" with "void" in Fig. R5a-c. These voids are primarily caused by e-beam or heating damage to Li_2S. On the other hand, the bubbles depicted in Fig. R2d and e were gas bubbles that resulted from focused e-beam in organic electrolyte in liquid cells.

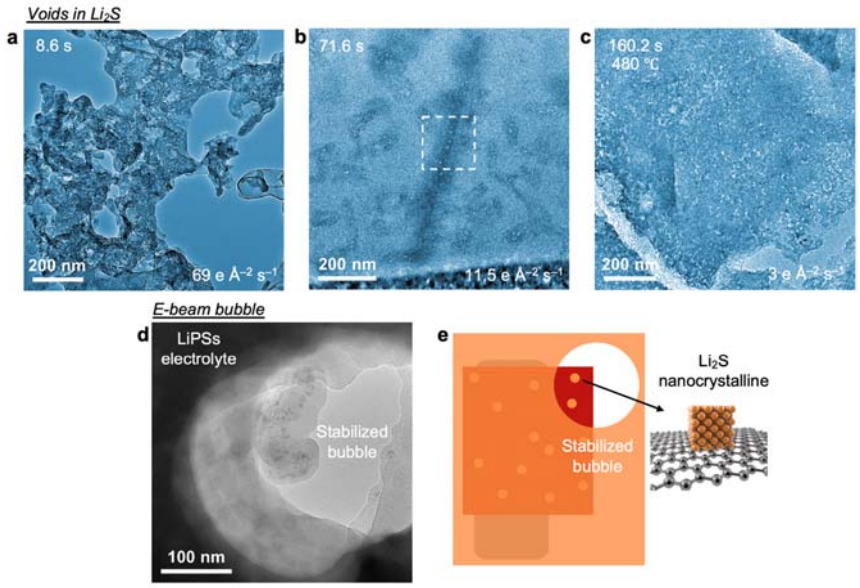

Fig. R5 | Voids in Li_2S and e-beam bubble generation. TEM images showing voids in Li_2S: (a) commercial Li_2S at a dose rate of 69 e $Å^{-2}$ s^{-1}, (b) electro-deposited Li_2S at a dose rate of 11.5 e $Å^{-2}$ s^{-1}, (c) commercial Li_2S heating at specific temperature at a dose rate of 3 e $Å^{-2}$ s^{-1}. (d, e) TEM image and schematic illustration showing "e-beam bubble generation" method for HRTEM observation of Li_2S nanocrystalline.

Revision to Comment 5: The corresponding descriptions have been revised in Supplementary Discussions (2. E-beam effects).

Comment 6: *In Comment 3, (2) Impact of electrolyte concentration on nucleation-growth pathways section, the authors provided only the effect of different potential, not electrolyte concentration. Thus, the authors should investigate the impact of electrolyte concentration and explain its effect clearly.*

Response to Comment 6: Following the suggestion of the referee, we investigated the effect of higher concentrations of Li_2S_6 electrolyte (20 and 50 mM) on the deposition of Li_2S. Our results showed that 50 mM Li_2S_6 (Fig. R6a) yielded similar deposition of rod-like/plate-like Li_2S on the electrode surface, but the spatial resolution was significantly reduced. On the other hand, with 20 mM Li_2S_6 (Fig. R6b), the electrode surface got clearer, and we observed both single-step and two-step deposition. Time-series TEM images and projection area variation indicated gradual deposition of Li_2S

into rod-like/plate-like structures (Fig. R6b, c). Statistical analysis of particles #11/#12 revealed similar reaction-limited stages in accordance with the Lifshitz-Slyozov-Wagner model (LSW, Area $\propto t^n$). Our findings suggest that the growth behavior remains largely unchanged compared to the lower concentration of Li_2S_6 electrolyte (10 mM) in the main text (Fig. 2). However, we did observe more solid discharge products, including both rod-like/plate-like and granular structures, on the electrode surface (Fig. R6d, e). Additionally, the higher electrolyte concentration increased the non-elastic scattering of electrons, which further decreased the spatial resolution of the liquid cell. Our statistical analysis of particles deposited using different concentrations of Li_2S_6 electrolyte (10 and 20 mM) revealed a reaction-limited stage in both cases (Fig. 2a and Fig. R6c), indicating sufficient reactant at the electrode/electrolyte interface. As a result, increasing the Li_2S_6 concentration did not alter the nucleation-growth pathway, but rather decreased the image resolution. In contrast, when we changed the discharge potentials (Extended Data Fig. 3), we observed distinct variations in deposition pathways. These results suggest that the deposition of Li_2S is primarily controlled by charge transfer at the electrode surface rather than the concentration of Li_2S_6 electrolyte.

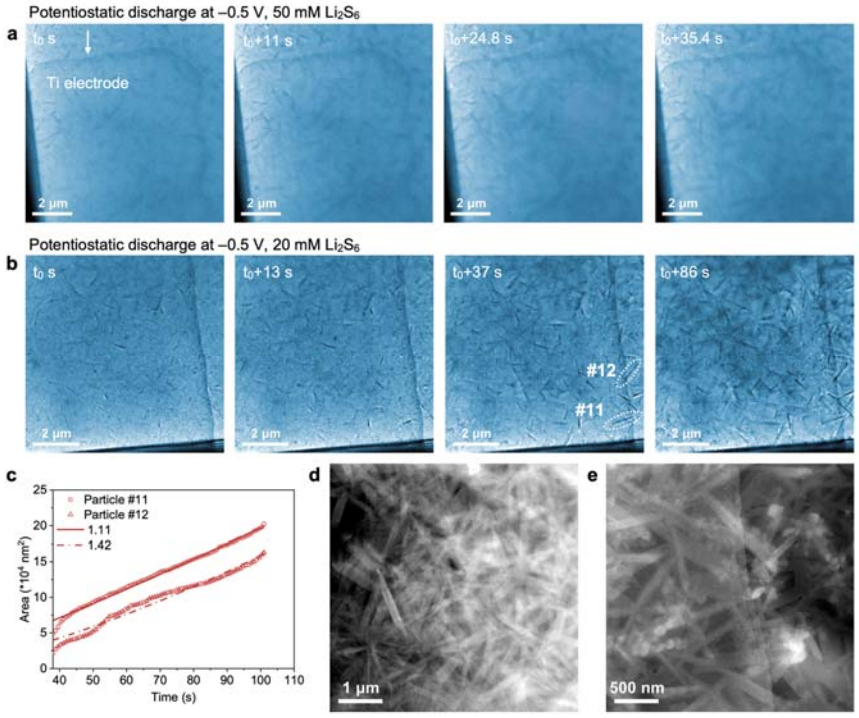

Fig. R6 | Deposition of Li_2S at –0.5 V with various Li_2S_6 concentrations. (a) Time-

series TEM images using 50 mM Li_2S_6 electrolyte for Li_2S deposition. Ti electrode edge is marked by a white arrow. (b) Time-series TEM images using 20 mM Li_2S_6 electrolyte for Li_2S deposition. (c) The projection area variation as a function of time of particles #11 and #12 in Fig. R6b. Error bars represent standard deviations of the measurement. (d, e) HAADF-STEM images after Li_2S deposition on the surface of Ti electrode using 20 mM Li_2S_6 electrolyte.

Revision to Comment 6: The corresponding contents have been added in manuscript (Page 5, Line 22-24) and Supplementary Fig. 14.

Comment 7: *In the Discussion of the depletion area section, it is unclear to understand the meaning of the content. The authors mentioned that "appearance of depletion layers is random at micro-/nano- scales, and there can be inconsistency in local observation area." If the appearance of the depletion layer is indeed random, then it cannot be explained. Thus, please explain the concept of depletion area more clearly or remove the section from the manuscript if the authors cannot adequately explain it.*

Response to Comment 7: After carefully considering your valuable suggestions, we find it better to remove the discussion of depletion areas from the manuscript. Our previous investigation has revealed that the formation of depletion areas is a highly complex process on the micro/nano scales. Therefore, we believe it is worthwhile to dedicate more effort to determine the formation mechanism in future work.

Referee #3:

General Comment: *After being revised, the manuscript has been improved and suitable for the publication. Therefore, I recommend it to be published as it is.*

Response to General Comment: Thank you for your approval and positive feedback to our revised version. We are delighted that our response can address your concerns and meet your expectations.

Reviewer Reports on the Second Revision:

Referees' comments:

Referee #2 (Remarks to the Author):

The authors have addressed all of my concerns. The methodology used to analyze their data is now much clearer. I believe the manuscript should be accepted for publication.